

# Study of an interacting ${}^6\text{Li}$ molecular Bose-Einstein condensate.

by Pierre Jouve, MSc.



Thesis submitted to The University of Nottingham  
for the degree of Doctor of Philosophy, June 2019



The University of  
**Nottingham**

UNITED KINGDOM • CHINA • MALAYSIA

# Contents

<b>Abstract</b>	<b>5</b>
<b>Acknowledgements</b>	<b>9</b>
<b>1 Introduction</b>	<b>10</b>
<b>2 Interactions in an ultracold gas</b>	<b>13</b>
2.1 Elastic collisions . . . . .	13
2.2 Feshbach resonance . . . . .	16
<b>3 Degenerate quantum gas</b>	<b>21</b>
3.1 Gas of bosons . . . . .	22
3.1.1 History . . . . .	22
3.1.2 How to count indistinguishable particles? . . . . .	23
3.1.3 Bose Einstein condensation of an ideal gas . . . . .	24
3.1.4 The chemical potential $\mu$ . . . . .	28
3.2 Fermi gas . . . . .	30
3.2.1 BCS state . . . . .	32
3.2.2 BEC-BCS crossover . . . . .	32
3.2.3 Thermal and condensate molecules . . . . .	33
<b>4 Basics of cold atoms physics</b>	<b>35</b>
4.1 Alkali atoms . . . . .	35
4.2 Interaction between atoms and a magnetic field . . . . .	39

4.3	Interaction between atoms and light . . . . .	44
4.3.1	The dipole force . . . . .	44
4.3.2	The scattering force . . . . .	49
<b>5</b>	<b>Guideline to making a <math>^6\text{Li}</math> BEC</b>	<b>51</b>
5.1	Heating up the atoms . . . . .	52
5.2	Transfer to the main chamber . . . . .	53
5.3	First cooling in the main chamber . . . . .	56
5.3.1	The magneto-optical Trap (MOT) . . . . .	57
5.3.2	Compression stage . . . . .	63
5.3.3	Cooling limits . . . . .	63
5.4	Evaporative cooling in the main chamber . . . . .	65
5.4.1	Evaporative cooling . . . . .	67
5.4.2	Dipole trap . . . . .	70
5.4.3	Feshbach Coils . . . . .	73
5.4.4	Stabilization of the dipole trap . . . . .	77
5.4.5	Trapping frequencies . . . . .	79
5.5	Imaging . . . . .	83
5.5.1	Absorption imaging . . . . .	83
5.5.2	TOF . . . . .	88
5.5.3	In situ imaging . . . . .	90
5.5.4	High field imaging and scattering length determination . . . . .	91
<b>6</b>	<b>Study of an interacting <math>^6\text{Li}</math> mBEC</b>	<b>94</b>
6.1	The Gross Pitaevskii equation . . . . .	96
6.1.1	Thomas-Fermi approximation . . . . .	98
6.1.2	Hartree-Fock equations . . . . .	99
6.2	The fitting models . . . . .	100
6.2.1	Ideal gas . . . . .	100
6.2.2	Semi-ideal . . . . .	102

6.2.3	Hartree-Fock . . . . .	106
6.2.4	Comparison between the SI and the HF model . . . . .	109
6.3	Fitting program . . . . .	109
6.4	Results . . . . .	111
6.5	Radius Measurement . . . . .	118
6.5.1	Relation between the radius of the condensate and the con- densate fraction using ideal gas model . . . . .	118
6.5.2	First correction to the ideal model . . . . .	119
6.5.3	Analytical Hartree Fock model . . . . .	120
6.5.4	Comparaison of the 3 models . . . . .	122
6.6	Results . . . . .	124
6.7	Prospects: Using an Energy conservation Method to Compare in-situ atom models . . . . .	126
6.7.1	Total energy calculation . . . . .	127
6.7.2	Predictive capabilities . . . . .	129
6.7.3	Numerical integration . . . . .	130
6.7.4	Experimental application . . . . .	130
<b>7</b>	<b>Initial work: Double well with <math>^6\text{Li}</math> molecules</b>	<b>133</b>
7.1	Introduction . . . . .	133
7.2	A Josephson junction in the cold atoms paradigm . . . . .	133
7.3	Experimental aparatus . . . . .	138
7.4	Prospects . . . . .	141
<b>8</b>	<b>Conclusions and outlook</b>	<b>142</b>
<b>A</b>	<b>Scattering length</b>	<b>145</b>
<b>B</b>	<b>Integration of Bose-Einstein distribution.</b>	<b>147</b>
<b>C</b>	<b>Laser Setup Lithium</b>	<b>150</b>

D Gaussian beams: useful quantities	152
E Offset lock	154
F Lithium properties	157
G Article: Collimated dual species oven source and its characterisation via spatially resolved fluorescence spectroscopy	159
H Article: Thermodynamics properties of a highly interacting $^6\text{Li}$ molecular Bose-Einstein condensate using in-situ imaging.	169
Bibliography	176

## Abstract

This thesis reports on a study of the molecular Bose-Einstein condensation (mBEC) of the  $^6\text{Li}$ . More specifically, using model the Hartree-Fock (HF) model to fit the spatial density of the cloud, we demonstrate that the thermal cloud deplete the condensate, therefore a lower temperature is needed to condense the atoms in the ground state. Moreover the inter-atomic interactions can be controlled via Feshbach resonance (see section 2.2), allowing us to study the effects of the interactions on the thermodynamics properties of a mBEC, especially the critical temperature of the BEC that decreases when we increase the inter-atomic interactions. The description starts from the experimental procedure to produce a mBEC to its physical analysis. We draw a list describing the different chapters presented in the thesis:

**Chapter 1 Introduction:** We present the fundamental difference between fermions and bosons, and we give some example of realisations of Bose-Einstein condensation and degenerate Fermi gas.

**Chapter 2 Interactions in an ultracold gas:** We discuss the role of interactions depending on the type of particles, either fermions or bosons, and the phenomena of Feshbach resonance which is a powerful tool to change the interaction strength between particles.

**Chapter 3 Degenerate quantum gas:** A brief historical section gives the fundamental ideas that initiate the long story of the Bose-Einstein conden-

sation phenomena. We then discuss the mathematical description of a BEC without interactions, which is the starting point of the theoretical analysis used in the chapter 3 where we study the influence of the interactions. Then, we describe the statistics of Fermi gas and the different states that can be reached using Feshbach resonances, in particular the creation of the Feshbach molecules.

**Chapter 4 Basics of Cold atoms physics:** A toolbox of the necessary knowledge to understand the underlying phenomena and concepts used in a cold atoms experiment. We describe the kind of atoms used, how these atoms interact with a magnetic and an electromagnetic field.

**Chapter 5 Guideline to making a  $^6\text{Li}$  BEC:** This chapter describes the experimental methods used in our laboratory to cool down atoms to the regime of ultra-cold temperature  $T < 1\mu\text{K}$ . This section gives details about atomic beams production, the Zeemann slower (radiation force cooling), the magneto-optical trap (MOT) (cooling by molasses), optical dipole trap (evaporative cooling). Also we present the methods used to probe atomic clouds, such as in situ imaging methods. My contribution to this section has been to improve the stability of the evaporative cooling sequence (see section 5.4.4) and to optimize the shape of the the evaporative cooling ramp (see section 5.4.1) in order to maximise the phase space density (PSD), to reach Bose-Einstein condensation. Then, to make precise simulations and measurements to extract values of the trapping frequencies (see section 5.4.5) and scattering length (see section 5.5.4), the latter gives us the interaction strength of the system. These parameter are then used in the next chapter to extract thermodynamics properties of the system. Moreover, I developed the sequence for in situ absorption imaging (see section 5.5.3).

**Chapter 6 Study of an interacting  $^6\text{Li}$  mBEC:** This chapter discusses the theory to understand the thermodynamics properties of an interacting Bose-

Einstein condensate. It is accomplished by fitting the spatial atomic density profiles with different models, the ideal gas (IG) model, the semi-Ideal (SI) gas model and the Hartree-Fock (HF) model. These three models vary in complexity from the most simple one the IG model to most elaborated one the HF model. The HF model requires a lot more of computational power than the other methods, therefore we present a new numerical method requiring less computational power proposed by Nathan Welch, and demonstrate experimentally through a statistical analysis that the HF model used to determine the thermodynamics properties of a BEC is more accurate to describe ultracold atomic gas near the transition. Then, we present the results of the influence of the scattering length on the transition temperature and the chemical potential. My contribution to this section has been to develop tools to analyse the in situ atomic density profiles and improve the fitting program of Nathan (see section 6.3). Also, after taking the measurement of the in situ atomic density profiles, I developed and used the tools for the analysis of the thermodynamics properties of the mBEC (see section 6.4). I also adapted the models described in [1] to our experiment to extract the value of the radius of the condensate (see section 6.5). Finally, with N.Welch we present method based on energy conservation to verify the validity of the different model, my principal contribution to this was to modify the experiment to use this method (see section 6.7).

**Chapter 7 Initial work: Double well with  $^6\text{Li}$  molecules:** This chapter presents the initial work to produce a double well potential to trap cold atoms and create a Josephson Junction. We present the state of the art of the different effects that have been observed, and discuss future measurements that would be achievable in our laboratory, in particular we would like to use a second specie  $^{133}\text{Cs}$  as impurities and observe the influence on Josephson oscillations of  $^6\text{Li}$  molecules. An experimental description of the double well trapping



potential has been implemented and is also described. My contribution to this section was to design and implement the double well trapping potential.

## Acknowledgements

When for the first time, I heard about the Bose-Einstein condensation in my statistical physics class, I was fascinated. How such a beautiful theory with amazing predictions can work in the real world ? Since then, I always wanted to learn how to make a Bose-Einstein condensate (BEC) experimentally. Therefore, I would like to thank sincerely Lucia Hackermuller, to give me the great opportunity to realise this beautiful state of the matter in the real world. Even if the field of cold atoms is very demanding due to the extreme precision required to manipulate atoms in such extreme conditions, I still find an inherent beauty in it. Such an experiment is a work of many people. I would like to thank Asaf, Matt, Sonali to have done an amazing work setting up this experiment and realising the first molecular BEC in UK. I would like to thank my colleagues, Nathan, Elisa, Danielle, that were extremely helpful when the experiment was difficult to tame. Thanks to Nathan Welch, for the discussion about the theory, also thanks to Jean Dalibard, to have kindly answered to my questions almost instantly, and to provide such high quality courses available for everyone. Finally, the last but not the least, my friend from the office, Manon, who were always there to laugh and joke, making days shorter.

# Chapter 1

## Introduction

“Mathematics, rightly viewed, possesses not only truth, but supreme beauty cold and austere, like that of sculpture, without appeal to any part of our weaker nature, without the gorgeous trappings of painting or music, yet sublimely pure, and capable of a stern perfection such as only the greatest art can show. The true spirit of delight, the exaltation, the sense of being more than Man, which is the touchstone of the highest excellence, is to be found in mathematics as surely as in poetry.”

— Bertrand Russell

According to Pauli [2], nature divides all particles into two parts, the particles with an half-integer spin the Fermions, and the particles with an integer spin the Bosons. The consequence of this feature appears when identical particles get close enough for their wavefunction to overlap. Fermions tend to repel each other, while Bosons tend to aggregate in the same state. In other words, the nature of Bosons and Fermions depends on the symmetry of their wavefunction. Thus, we consider two non-interacting spinless identical particles  $\Psi_A(x_1)$  and  $\Psi_B(x_2)$  at the position  $x_1$  and  $x_2$ .

We write the composite wave-function of the system:

$$\Psi(x_1, x_2) = \frac{1}{\sqrt{2}} [\Psi_A(x_1)\Psi_B(x_2) \pm \Psi_A(x_2)\Psi_B(x_1)] \quad (1.1)$$

If  $\pm$  is positive,  $\Psi$  is said to be symmetric with respect to exchange in space, i.e.  $\Psi(x_1, x_2) = \Psi(x_2, x_1)$ . This situation corresponds to the Bosons.

If  $\pm$  is negative,  $\Psi$  is said to be antisymmetric with respect to exchange in space, i.e.  $\Psi(x_1, x_2) = -\Psi(x_2, x_1)$ . This situation corresponds to the Fermions. For the Fermions, if the  $x_1 = x_2$  it implies the composite wavefunction to be  $\Psi(x_1, x_1) = 0$ . Consequently, the behaviour of the Bosons and the Fermions confined in an harmonic trap is very different when their wavefunctions expand at very low temperature. The Bosons undergoes a phase transition so-called Bose-Einstein condensation (BEC) and most of the atoms go into the lowest energy state, on an other hand the Fermions fill up all the available states (see Fig .1.1), this state is called a degenerate Fermi gas.

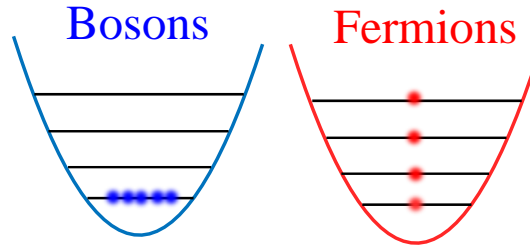


Figure 1.1: Bosons do not obey to the Pauli exclusion's principle, consequently at very low temperature they can aggregate in the lowest energy level and eventually undergo a phase transition to reach the Bose-Einstein condensation. Fermions do obey to the Pauli exclusion principle and two fermions can not be in the same state, therefore they fill up all the states, and the Fermi energy  $E_F$  is defined as the energy of the highest occupied energy level.

**Bose-Einstein condensation.** The first evidence of a BEC was realised in 1995 [3–5], 71 years after the first publication of N.Bose and A.Einstein [6]. From that

point, many experiments have been realised to understand fundamental aspects of many-body physics such as macroscopic matter wave interferences [7], the Mott insulator transition [8]. An excellent general description of BECs can be found in [9].

**Degenerate Fermi gas and cold atom molecules.** As described in Fig. 1.1, fermions behave very differently from the bosons and fill up all the available states. Various experiments have reached the quantum degeneracy regime with  $^{40}\text{K}$  [10, 11] and  $^6\text{Li}$  [12–14], and a summary of Fermi gas can be found in [15]. Two fermions in the same state do not interact, therefore to form pairs a mixture of fermions in two different states is required, usually two different spin states of the same fermion. Different regimes exist for these pairs (see Fig. 1.2), depending on the interaction strength between the atoms. From tightly bound molecules [16] that behaves like a BEC to the regime of long range Cooper pairs [13, 17] (Bardeen-Cooper-Schrieffer state). In the middle, the crossover regime [18] where the pair size is in the order of the inter-particle size and the interaction is very high.

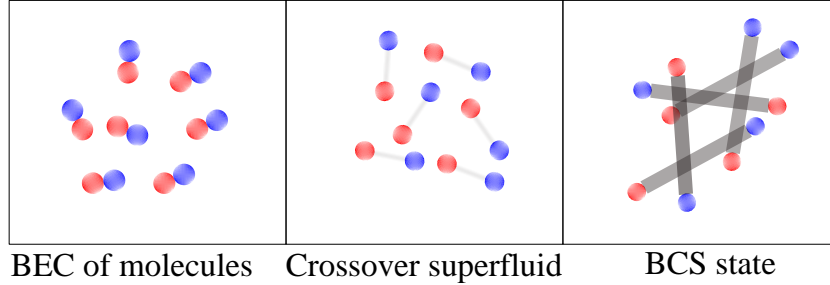


Figure 1.2: Pair of Lithium atoms in different regime, each regime can be reached by tuning a magnetic field around a Feshbach resonance. Figure inspired from [19].

This thesis is focused on the creation and the study of cold atom molecules in the regime of high interactions. A summary of the different chapters and my contributions are given in the abstract.

# Chapter 2

## Interactions in an ultracold gas

The control of the interactions of ultracold particles is a crucial feature of the system. The interactions can be controlled through a phenomenon called Feshbach resonance, which allows us to change the inter-atomic interaction strength by tuning a magnetic field. It is used in most stages of our experiment. When we evaporate atoms in the dipole trap, we want to increase the interactions to enhance the thermalisation rate [20]. Also, the interactions are used for the creation of the  $^6\text{Li}_2$  molecules, these molecules are made of two fermions, and follow a Bose-Einstein distribution, therefore can be cooled down to very low temperature to form a Bose-Einstein condensate (BEC). The binding energy of the molecules can be tuned and the molecular BEC (mBEC) can be transformed into a fermionic degenerate gas of weakly bound molecules, so-called Bardeen-Cooper-Schrieffer (BCS) state, or an universal regime where the interaction strength diverges.

The interactions between atoms or molecules are described by a quantity called **scattering length**  $a$ , which is the characteristic length of the interactions.

### 2.1 Elastic collisions

In our experiment, atoms are cooled down to  $T < 1\mu\text{K}$ , therefore collisions happen at low kinetic energy, in that case collisions are mainly isotropic, this is true if the

potential is decreasing faster than  $r^{-2}$  [21]. The collision between two particles is best described in the center-of-mass reference frame. Thus, it can be understood as the collision of a particle with a wave vector  $\vec{k}$  and a scattering centre at the origin. Far from the scattering centre, the wave function relative to the two particles can be written as:

$$\psi_k(\vec{r}) = \psi_{inc} + \psi_{sc} = e^{i\vec{k} \cdot \vec{r}} + f_k(\theta, k) \frac{e^{ikr}}{r}. \quad (2.1)$$

where  $f_k(\theta, k)$  is the probability amplitude for a particle of momentum  $\hbar k$  to scatter under an angle  $\theta$ ,  $\psi_{inc}$  and  $\psi_{sc}$  are the incident and scattered wavefunctions of the particles. The scattering amplitude probability  $f_k(\theta, k)$  is directly related to the differential cross section  $\frac{d\sigma}{d\Omega}$  by:

$$\frac{d\sigma}{d\Omega} = |f_k(\theta, k)|^2. \quad (2.2)$$

Due to the rotational symmetry of the system, a separation of  $\psi_k(\vec{r})$  into an angular and radial component is possible. The angular component is expanded into the eigenfunctions of angular momentum  $l = 0, 1, 2, \dots$  ( or  $l=s, p, d, \dots$ ), using the Legendre function  $P_l(\cos(\theta))$ , which leads to:

$$\psi_{sc}(\vec{r}) = \sum_{l=0}^{\infty} R_l(r) P_l(\cos(\theta)). \quad (2.3)$$

Solving the radial Schrodinger equation for  $r \rightarrow \infty$ , we obtain the radial solution  $R_l$  given by:

$$R_l = A_l \frac{1}{kr} \sin(kr - \frac{\pi}{2}l + \delta_l). \quad (2.4)$$

Here  $\delta_l$  is the phase shift between the scattered and the unperturbed wave caused by the scattering potential, it contains all information relevant for the scattering process,  $A_l$  is the amplitude. By inserting eq.(2.4) in eq.(2.3) and expanding  $\psi_{inc}$  into spherical waves as well, one can get the following expression for the scattering amplitude:

$$f_k(\theta, k) = \frac{1}{2ik} \sum_{l=0}^{\infty} (2l+1) (e^{2i\delta_l} - 1) P_l(\cos(\theta)). \quad (2.5)$$

Now one can integrate eq.(2.2) using eq.(2.5) and obtain:

$$\sigma(k) = \frac{4\pi}{k^2} \sum_{l=0}^{\infty} (2l+1) \sin^2(\delta_l). \quad (2.6)$$

We note that for Bosons, only even  $l = 0, 2, 4, \dots$  numbers are authorized and that for Fermions only odd  $l = 1, 3, 5, \dots$  numbers are allowed. This means that in the ultracold regime, where the  $s$ -scattering waves dominate, pairs of bosons can collide, and pairs of fermion in the same quantum state can not collide and form an ideal gas [22]. In our experiment, in order to have two  ${}^6\text{Li}$  atoms to collide, we have to create a mixture of two hyperfine states of  ${}^6\text{Li}$  to enable collisions (see section 5). Also, the centrifugal barrier causes the scattering phase to scale like  $\delta_l \propto k^{2l+1}$  [23], if the momentum is small compared to the interatomic potential, scattering processes with  $l > 0$  are suppressed for  $k \rightarrow 0$ , which is fulfilled in the ultracold regime. For the case of purely  $s$ -wave scattering  $l = 0$ , we have the following scattering amplitude:

$$f_0 = \frac{1}{2ik} (e^{2i\delta_0} - 1). \quad (2.7)$$

By defining the scattering length  $a$  as:

$$\lim_{k \rightarrow 0} \frac{\tan \delta_0}{k} = -a, \quad (2.8)$$

and using  $\delta_0 \approx ka$  we arrive at the final result for the scattering amplitude:

$$f_0 = -\frac{a}{1 + ika}. \quad (2.9)$$

with the energy independent cross section:

$$\lim_{k \rightarrow 0} \sigma_0(k) = 4\pi a^2 \quad (2.10)$$

## Cross section

The cross section is directly related to the scattering amplitude through eq.(2.2), and a general expression for cross section energy is given in [24]:

$$\sigma(k) = \frac{4\pi a^2}{1 + k^2 a^2} \quad (2.11)$$



In a weakly interacting gas,  $k^2 a^2 \ll 1$  this leads to a total elastic cross section of  $\sigma = 4\pi a^2$ . For the strongly interacting case with  $k^2 a^2 \gg 1$  so-called unitary limit, the cross section is  $\sigma_u = \frac{4\pi}{k^2}$ .

## Identical particles

Previously, we considered the particles that collide to be distinguishable, however identical particles have to be treated differently. If the particles are identical, the two scattering processes shown in Fig. 2.1 can not be distinguished, and their scattering amplitude can interfere. For fermions, it results in an elimination of the partial wave with even numbers, and for bosons an elimination of the partial waves with an odd number. The cross sections that are not annihilated are multiplied by a factor 2. Consequently, the cross section for bosons in the ultra cold regime is  $\sigma_k = 8\pi a$ , and for fermions there are no collisions.

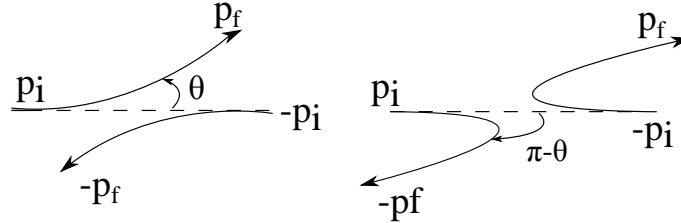


Figure 2.1: The two equivalent collisions processes for a pair of identical particles.

## 2.2 Feshbach resonance

In this section, we discuss the origin and effect of Feshbach resonance, responsible for the formation of diatomic molecules[25, 26]. To change the interaction strength, we need to be able to tune a parameter in the inter-atomic potential, this is accomplished by coupling two scattering channels, one is open, where the collisions are energetically allowed, and one is closed, where a bound state  $\varphi(r)$  exists (see Fig. 2.2), and this channel is energetically forbidden.

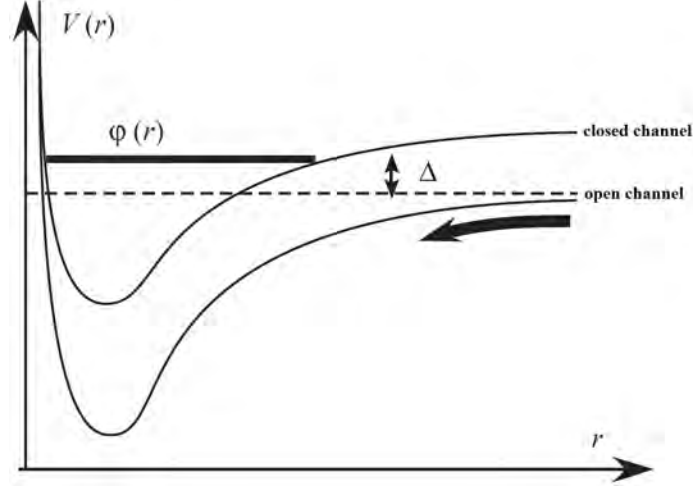


Figure 2.2: Schematic representation of the open channel and the closed channel with a molecular bound state, and  $\Delta$  the gap between the two channels.

The interatomic potential depends on the internal state of the atoms, different internal states lead to different potentials [27]. In our case,  $^6\text{Li}$  atoms are prepared in a mixture of the two lowest hyperfine states  $|F = \frac{1}{2}, m_F = \pm \frac{1}{2}\rangle$  (see Fig. 4.5). According to the spin 1/2 coupling, we have two cases, **the triplet state** with **a symmetric** spin arrangement  $M_F = -1, 0, 1$  and **a singlet state** with **anti-symmetric** spin arrangement,  $M_F = 0$ . In this configuration a Feshbach resonance occurs when two atoms scatter in the singlet state potential (open channel), which is the only one energetically allowed. Then the triplet state that has a non zero magnetic momentum is brought closer to the singlet state by applying a magnetic field (see Fig. 2.3). Only the triplet state will be shifted because of **non-zero value of magnetic momentum**  $M_F$ .

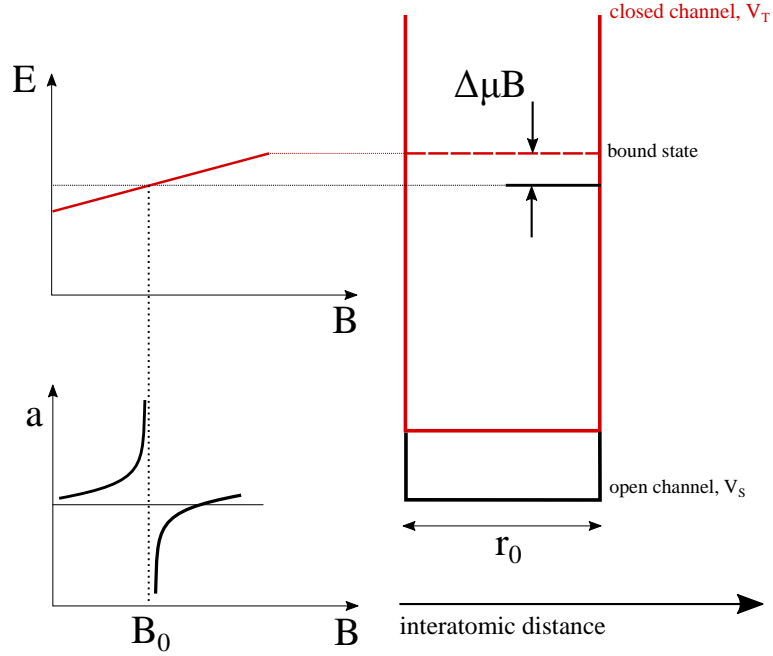


Figure 2.3: Schematic representation of two box potentials, one open channel (triplet state) and one closed channel (singlet state) with a molecular bound state. The triplet state (non zero magnetic momentum) can be brought closer to the singlet state using an external magnetic field. The total energy of the closed channel changes with  $\Delta E = \mu \Delta B$ . When the bound state of the closed channel meet the continuum of the open channel, the scattering length  $a$  diverge. A similar effect has been demonstrated in section A.

## Simple model for Feshbach Resonances

In the following model, we consider two identical atoms, with mass  $m$ . The vector base is composed of the **open channel**  $|o\rangle$ , and the **closed channel**  $|c\rangle$ . The wave function of the atoms is defined by  $|\psi\rangle = \psi_o(r)|o\rangle + \psi_c(r)|c\rangle$ , with  $\psi_o(r)$  and  $\psi_c(r)$  the amplitudes in the open and closed channels. The model is defined by the following equation:

$$E|\psi\rangle = \frac{\hbar^2}{m}(-\nabla^2 + \hat{v})|\psi\rangle, \quad (2.12)$$

where the potential  $\hat{v}$  is defined as:

$$\hat{v} = \begin{cases} \begin{pmatrix} V_o & \Omega \\ \Omega & V_c(B) \end{pmatrix}, & r < r_0 \\ \begin{pmatrix} 0 & 0 \\ 0 & \infty \end{pmatrix}, & r > r_0 \end{cases} \quad (2.13)$$

Further details can be found in [28]. In more technical terms, a Feshbach resonance is caused by second order coupling of an open with a closed channel, induced by hyperfine interaction [15]. In eq.(2.13), the coupling is represented by the frequency  $\Omega$ . In the case of a square well, eq.(2.12) can be solved analytically and results in an expression for the scattering length as a function of the magnetic field [28]:

$$a = a_{bg} \left( 1 - \frac{\Delta_B}{B - B_0} \right). \quad (2.14)$$

The background scattering length  $a_{bg}$  results from the scattering open channel potential. The position of the resonance is  $B_0$ , and  $\Delta_B \propto \frac{g^2}{\Delta\mu a_{bg}}$  is the width of resonance depending on the square of the coupling strength  $g$  between the two channels.

**<sup>6</sup>Li Feshbach Resonances,** A <sup>6</sup>Li spin mixture of the two lowest hyperfine states  $|1\rangle$  and  $|2\rangle$  (see Fig. 4.5) exhibits two s-wave Feshbach resonances, a very broad one at 834G (Fig. 2.4) that we are using in this experiment [29], and a narrow one at 534G [30, 31].

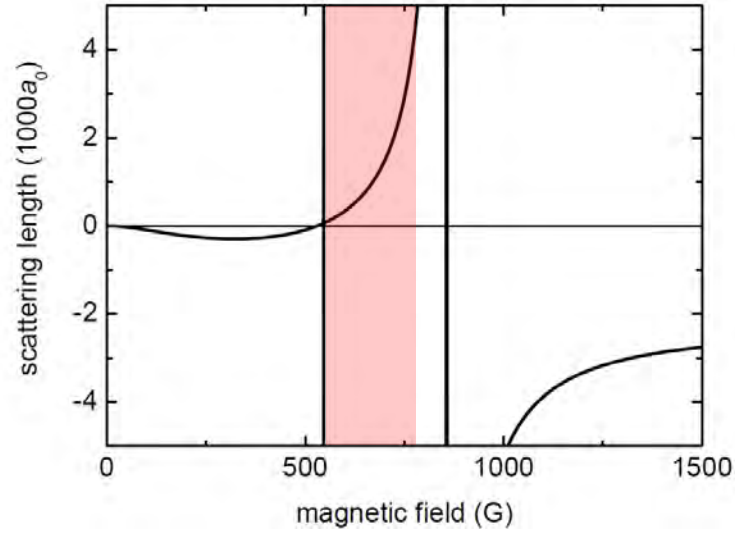


Figure 2.4: Plot of the magnetic Feshbach resonance of a  $|F = \frac{1}{2}, m_F = \pm\frac{1}{2}\rangle$  spin mixture of  $^6\text{Li}$  [32]. The red shaded zone is the range of interactions studied in our experiment.

# Chapter 3

## Degenerate quantum gas

We can associate to every particles the thermal de Broglie wavelength:

$$\lambda_{dB} = \sqrt{\frac{2\pi\hbar^2}{mk_BT}} \quad (3.1)$$

This length  $\lambda_{dB}$  represents the expansion of the wave packet of the particle. When the temperature is high enough, the de Broglie wavelength is negligible, and we can consider the particle classically. At low temperature<sup>1</sup>, the wave packet of the particles start to overlap and the classical treatment is not sufficient. To quantify the overlapping of the wave packets, we define the phase space density (PSD):

$$D = \lambda_{dB}^3 n \quad (3.2)$$

where  $n$  is the density of particles. When  $D \approx 1$  the nature of the particles, either bosons or fermions will lead to different behaviour. The bosons will condense into the ground state of the trap and eventually form a BEC, and the fermions will fill up the different energy level of the trap (see Fig. 1.1), this has been observed in [13], where they produce a mixture of a Fermi sea of  $^6\text{Li}$  and a BEC of  $^7\text{Li}$ .

---

<sup>1</sup>T=1 $\mu$ K corresponds to  $\lambda_{dB}$ =300nm

## 3.1 Gas of bosons

The Bose-Einstein condensation is a beautiful example of a physical phenomena first developed theoretically, leading to some effects beyond belief, allowing us to see the fundamental nature of matter in a fascinating new state of matter where all the particles seem to become one. In this section, we start with a brief overview on the history of the Bose-Einstein condensation. Then, we discuss the notion of distinguishability of particles, and the implication on the way we count them. Finally, we expose the fundamental results of the Bose-Einstein condensation in the non-interaction case, that will be used as a starting point for the study of the  $^6\text{Li}$  molecular Bose-Einstein condensate (mBEC).

### 3.1.1 History

The interpretation of the black body radiation has been the beginning of the era of quantum physics. Indeed, to understand the distribution of the spectrum of light at equilibrium, Planck introduced the idea of the quanta of energy. Different demonstrations of the Planck's formula have been found. Among them, the idea of Satyendra Nath Bose, that considered the light as a gas of identical particles. By looking for the most probable energy distribution of this gas made of identical particles, Bose found the Planck's distribution. Einstein found that approach interesting, he helped Bose to publish [6], and generalised the idea to the ideal gas, known as the Bose-Einstein distribution. The Einstein's formulas established in his second article [33], lead to an interesting effect. If  $V$  (volume) and  $N$  (number of atoms) are constant, when the temperature  $T < T_c$ , with  $T_c$  the critical temperature, atoms are transferred into the ground state (i.e. lowest energy state). Moreover,  $N_0$  the number of atoms in the ground state tends to  $N$  if the temperature is low enough. At this time, physicists, Einstein included, did not believe in this effect, at such a low temperatures people thought that matter could only exists as a gas or a liquid. Moreover, this interpretation appears in the early stage of the quantum

physics theory, and the Schrödinger's equation only arrived one year after [21].

### 3.1.2 How to count indistinguishable particles?

To establish the energy distribution of an ideal gas, we need to count the number of distinct microscopic states associated to a macroscopic state of the gas. For Einstein, the distinct microscopic states are defined by the number of atoms in each domain  $\Delta_i$  with an energy  $E_i$  between  $E_i$  and  $E_i + \Delta E_i$ . Each domain has  $g_i$  cells, corresponding to different quantum states. Now, instead of having distinguishable particles that we can label, we define indistinguishable particles without labels. In Fig. 3.1, we illustrate the counting of microscopic states for distinguishable and indistinguishable particles, considering 3 particles spread over two cells.

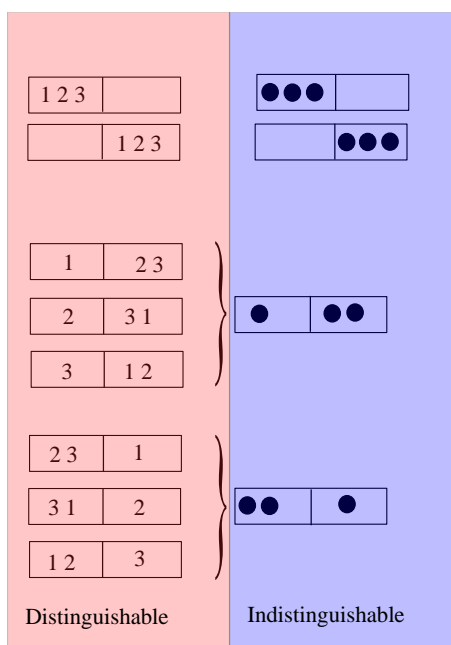


Figure 3.1: Microscopic state of 3 identical particles spread into two cells. The left part corresponds to the case of distinguishable particles, and particles are labelled by a number. The right part of the picture corresponds to the case of indistinguishable particles.

The number of microscopic states is different for the indistinguishable and dis-



tinguishable particles, respectively 4 and 8. Another important idea is shown in that figure, the number of microscopic states where all particles are in the same cell are equal. However, when particles are spread in different cells, the permutations of distinguishable particles lead to a greater number of microscopic state than the number of microscopic states of indistinguishable particles. Therefore, the relative weight of particles situated in the same cell in comparison with particles spread in different cells is also different. For distinguishable particles it is  $1/4$ , and for indistinguishable particles  $1/2$ , this gives a hint why bosons that are indistinguishable tend to accumulate in a same cell.

### 3.1.3 Bose Einstein condensation of an ideal gas

First, let's consider indistinguishable atoms without interaction, in contact with a thermostat. We want to find the most probable macroscopic state for a fixed atom number and fixed total average energy:

$$\sum_i N_i = N \qquad \sum_i N_i E_i = E \qquad (3.3)$$

Einstein calculated the number of distinct microscopic states corresponding to a macroscopic state defined by the set of  $\{N_i\}$ , with  $N_i$  the number of atoms in the domains  $\Delta_i$ , supposing indistinguishable particles. Then, he looked for the maximum of this number with the constraints eqs.(3.3). Consequently, the mean occupation number  $\bar{n}_i$  of the state  $i$  is given by the Bose-Einstein distribution:

$$\bar{n}_i = \frac{1}{\exp\left[\frac{\epsilon_i - \mu}{k_B T}\right] - 1}, \qquad (3.4)$$

where  $T$  is the temperature of the thermostat, and  $\mu$  the chemical potential fixed by the normalization  $\sum_i \bar{n}_i = N$ . In the denominator, the  $-1$  term is crucial, when the term in the exponential tends to 0 (lowest energy state), consequently the exponential term will tend to 1 and the density will diverge, which is fundamentally different from the classical Maxwell-Boltzmann distribution.

Now, let's consider an harmonic trap potential  $V_{\text{ext}} = \frac{1}{2}m(\omega_x^2 x^2 + \omega_y^2 y^2 + \omega_z^2 z^2)$  of an atom of mass  $m$ , the  $\omega_i$  are the trapping frequencies in three spatial directions. Using this trapping potential, we define the Hamiltonian of the system:

$$H^{sp} = \frac{p^2}{2m} + V_{\text{ext}}(\mathbf{r}) \quad (3.5)$$

with the eigenvalues :

$$\epsilon_{n_x n_y n_z} = \left(n_x + \frac{1}{2}\right) \hbar \omega_x + \left(n_y + \frac{1}{2}\right) \hbar \omega_y + \left(n_z + \frac{1}{2}\right) \hbar \omega_z, \quad (3.6)$$

where  $n_i = 0, 1, \dots$  is the energy level quantum number. At temperature  $T$ , the total number of particles is given by:

$$N = \sum_{n_x n_y n_z} \frac{1}{\exp[\beta(\epsilon_{n_x n_y n_z} - \mu)] - 1}, \quad (3.7)$$

where  $\beta = (k_B T)^{-1}$ . Now, we separate the lowest state  $\epsilon_{000}$  from the sum and call  $N_0$  the number of particle in this state. The chemical potential is equal to the energy of the lowest state,  $\mu \rightarrow \mu_c = \frac{1}{2}\hbar(\omega_x + \omega_y + \omega_z)$  in order to maximize the number of thermal atoms  $N_T = N - N_0$ :

$$N_{T,max} = \sum_{n_x n_y n_z \neq 0} \frac{1}{\exp[\beta(\epsilon_{n_x n_y n_z})] - 1}, \quad (3.8)$$

when  $N \rightarrow \infty$ , the condition  $k_B T \gg \hbar(\omega_x \omega_y \omega_z)^{1/3}$  (semi-classical approximation), and the sum can be replaced by an integral. Moreover knowing the density of state of an ideal gas in an harmonic trap  $g(\epsilon) = \epsilon^2 / (2\hbar^3 \omega_{ho}^3)$  we can write:

$$N_{T,max} = \int_0^\infty \frac{\epsilon^2 d\epsilon}{2\hbar^3 \omega_{ho}^3 (\exp(\beta\epsilon) - 1)}, \quad (3.9)$$

where:

$$\omega_{ho} = (\omega_x \omega_y \omega_z)^{1/3}, \quad (3.10)$$

the average harmonic trapping frequency. We take eq.(3.9) and set  $N_T = N$ , i.e. the critical point of the Bose-Einstein condensation, we have the following relation for the critical temperature [34]:

$$T_c^0 = \frac{\hbar \omega_{ho}}{k_B} \left( \frac{N}{\zeta(3)} \right)^{1/3}, \quad (3.11)$$

where  $\zeta(x)$  is the Riemann's Zeta function,  $\zeta(x) = \sum_1^\infty k^{-x}$ . The peak phase space density of an ideal gas in an harmonic trap is given by:

$$D(T) = N \left( \frac{\hbar\omega_{ho}}{k_B T} \right)^3 \quad (3.12)$$

Then, we calculate the phase space density at the critical temperature  $T_c$ :

$$D(T_c) = N \left( \frac{\hbar\omega_{ho}}{k_B T_c} \right)^3 = \zeta(3) \approx 1.202, \quad (3.13)$$

this represent the condition for the apparition of a BEC. Using eq.(3.9) and the normalization condition  $N_0 + N_T = N$ , we obtain the condensate fraction against the temperature (see Fig. 3.2):

$$\frac{N_0}{N} = 1 - \left( \frac{T}{T_c} \right)^3. \quad (3.14)$$

These results are very useful to evaluate the critical temperature knowing the atoms number, and will be used in this thesis as a reference point. However, due to the role of the inter-atomic interactions that are a very important parameter in the  $^6\text{Li}$  mBec, this simple model is not accurate enough and we will discuss more sophisticated model suitable for the study of a highly interacting BEC.

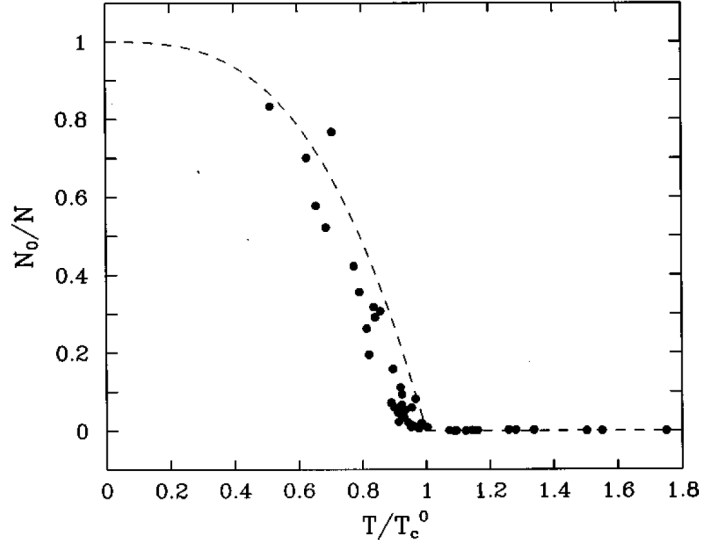


Figure 3.2: Condensate fraction as a function of  $T/T_c^0$ . Circles are the experimental results of *Ensher et al(1996)*. While the dashed line is eq.(3.14). We notice a deviation from the theoretical curve, which is due to the inter-atomic interactions, weak enough in that case to be close to the theoretical model.

**Wave function of an ideal gas BEC.** For a BEC, the wave function is defined by the lowest energy state ( $n_x = n_y = n_z = 0$ ) of a single particle function and is given by:

$$\phi_0 = \left(\frac{m\omega_{ho}}{\pi\hbar}\right)^{3/4} \exp\left[-\frac{m}{2}(\omega_x x^2 + \omega_y y^2 + \omega_z z^2)\right], \quad (3.15)$$

where we can define the length of the harmonic oscillator  $a_{ho} = \sqrt{\frac{\hbar}{m\omega_{ho}}}$ . And the density distribution is given by  $n(\mathbf{r}) = N|\phi_0(\mathbf{r})|^2$ . For typical value of trapping potential in our experiment, the harmonic oscillator length for  $^6\text{Li}_2$  molecules is  $a_{ho} = 3\mu\text{m}$ .

**Finite size effect correction.** Due to the finite size of the system the thermodynamic is never reached even if the number of atoms is  $N \approx 10^7$ . Therefore, in [35] they work out a finite size correction given by:

$$\frac{N_0}{N} = 1 - \left(\frac{T}{T_c^0}\right)^3 - \frac{3\bar{\omega}\zeta(2)}{2\omega_{ho}\zeta(3)^{2/3}} \left(\frac{T}{T_c^0}\right)^{2/3} N^{-1/3}, \quad (3.16)$$

where  $\bar{\omega}$  is the arithmetic average of the trapping frequencies. The correction scales like  $\propto N^{1/3}$  and become relevant when we approach the critical temperature. In Fig. 3.3, we plot the correction for  $N = 5 \cdot 10^5$  atoms, that corresponds to the number of atoms that we have in our experiment, the correction small and mainly visible near the phase transition.

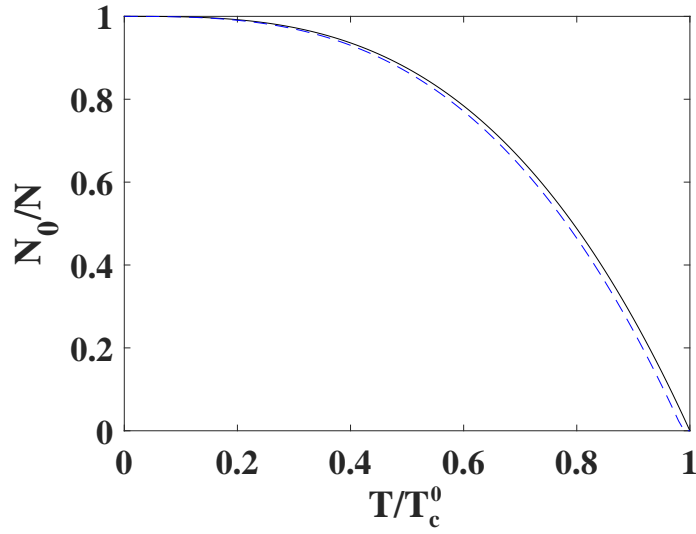


Figure 3.3: Solid line represent the thermodynamic limit and the dashed line the finite size effect correction for  $N = 5 \cdot 10^5$ .

### 3.1.4 The chemical potential $\mu$

A key parameter in Bose Einstein condensation is the chemical potential [36]. Because this parameter is often a source of confusion, this section describes the chemical potential with a particular attention on its meaning.

**Intuitive picture of the chemical potential  $\mu$  for a non-interacting gas.** In thermodynamics, when a system exchanges energy and particles with a reservoir, its internal energy  $U$  changes following the thermodynamic identity:

$$dU = TdS - pdV + \mu dN. \quad (3.17)$$

Where  $T$  is the temperature,  $S$  the entropy,  $p$  the pressure,  $V$  the volume and  $N$  the atom number. From eq.(3.17) we obtain the chemical potential  $\mu$ :

$$\mu = \left. \frac{\partial U}{\partial N} \right|_{S,V}. \quad (3.18)$$

The chemical potential  $\mu$ , is the energy difference, when a particle is added or removed from the system, with  $S$  the entropy (constant) and  $V$  the volume (constant). In order to have a better understanding of the chemical potential, let's consider a system with equally spaced energy level by the energy  $\epsilon$ , with the ground state energy equal to zero. We assume that we have two distinguishable particles, **A** and **B**, and that the energy of the system is  $2\epsilon$ . Therefore, there are 3 microstates available, and the entropy is simply calculated with  $S = k_B \ln(3)$ .

A	B
$2\epsilon$	0
0	$2\epsilon$
$\epsilon$	$\epsilon$

Now, if a particles is added, the number of available microstates is 6, the entropy becomes  $S' = k_B \ln(6)$ , but according to the definition of the chemical potential eq.(3.18), the entropy should remain constant.

A	B	C
$2\epsilon$	0	0
0	$2\epsilon$	0
0	0	$2\epsilon$
$\epsilon$	0	$\epsilon$
$\epsilon$	$\epsilon$	0
0	$\epsilon$	$\epsilon$

Therefore, the new particles should bring an energy of  $-\epsilon$  to keep the number of microstates to 3, and  $S = S'$ . At the end, the chemical potential is  $\mu = -\epsilon$ , the energy of the system decreases as a particle is added.

**The chemical potential  $\mu$  for an ideal Bose Gas.** Now, we will describe the meaning of the chemical potential for a BEC. For an ideal BEC at  $T = 0$ , all atoms are in the ground state with the energy  $\epsilon = 0$ . There is only one micro state, therefore the entropy  $S = k_B \ln(1) = 0$ , then  $\Delta U = 0$ ,  $\Delta S = 0$ , thus  $\mu = 0$ . Now, let's consider a gas with a finite temperature below the critical temperature. If a particle is added at very low temperature, the probability of being added in the ground state is very high, then the entropy should increase by a small amount, the system should be allowed to decrease slightly its energy by cooling, therefore, the energy needed to compensate the chemical potential is very small in amplitude and negative. If the temperature increases, the number of microstates increases, and  $\mu$  becomes more negative.

## 3.2 Fermi gas

For fermions, according to the Pauli exclusion principle, two fermions cannot be in the same quantum state, the corresponding distribution at finite temperature is given by the Fermi-Dirac distribution:

$$\bar{n}_i = \frac{1}{\exp\left[\frac{\epsilon_i - \mu}{k_B T}\right] + 1}, \quad (3.19)$$

the difference with the BE distribution is the  $+1$  at the denominator, this implies an average occupation number  $\leq 1$ . Here  $\mu$  is the energy of the highest occupied state, so-called Fermi energy  $E_F$ , and its value is given by [15]:

$$E_F = \hbar\omega_{ho}(6N)^{1/3}, \quad (3.20)$$

where  $\omega_{ho} = (\omega_x\omega_y\omega_z)^{1/3}$ , and  $N$  the number of fermions. Using the Fermi energy, we define the radius of the cloud in the trap:

$$R_{TF} = \sqrt{\frac{2E_F}{m\omega_{ho}^2}} = a_{ho}(48N)^{1/6}, \quad (3.21)$$

where  $a_{ho} = \sqrt{\frac{\hbar}{m\omega_{ho}}}$  the length of the harmonic oscillator. We can also define the largest momentum  $p_F = \hbar k_F = \sqrt{2mE_F}$ , where  $k_F$  is the Fermi wave number.

Locally, it is defined by  $p_F(\mathbf{r}) = \hbar k_F(\mathbf{r}) = \sqrt{2m\epsilon_F(\mathbf{r})} = \hbar(6\pi^2 n_F(\mathbf{r}))^{1/3}$ , where  $\epsilon_F = \mu(\mathbf{r}, T = 0) = E_F - V(\mathbf{r})$ . At the center of the trap where  $V(\mathbf{r}) = 0$ , we can calculate the density:

$$n(0) = \frac{2}{\sqrt{3}\pi^2} \frac{\sqrt{N}}{a_{ho}^3}, \quad (3.22)$$

and the wave number:

$$k_F = (6\pi^2 n(0))^{1/3}, \quad (3.23)$$

which has the dimension of the inverse of a length and proportional to the separation between particles. To classify the different regime, we use the quantity  $1/k_F a$ , which is the ratio between the particle separation between particles and the scattering length, and can be positive or negative. The different phase are summarized in Fig. 3.4.

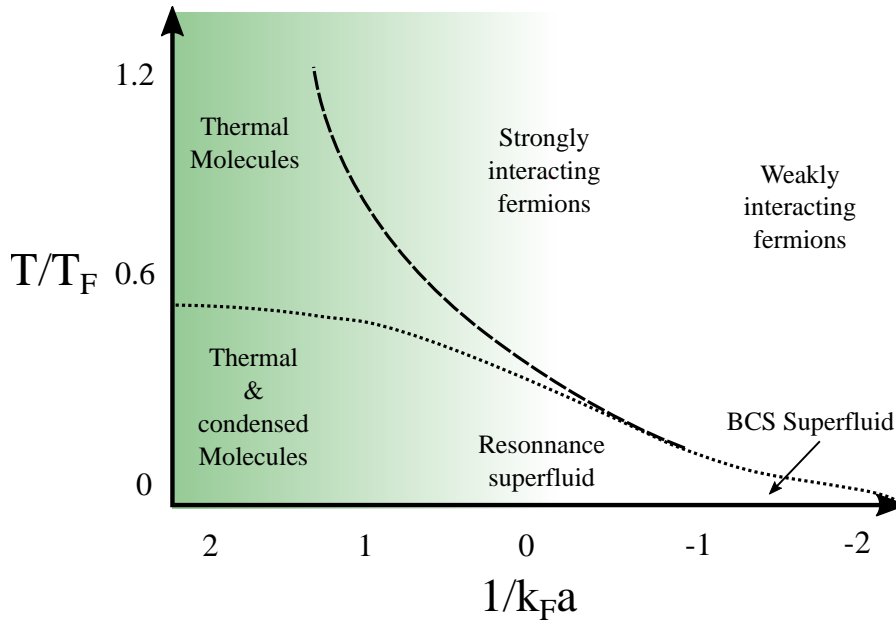


Figure 3.4: Phase diagram for fermions inspired from [15]. The dotted line represent the line of critical temperature  $T_c$ , and the dashed line the line where starts the formation of pairs of fermions. The shaded area represents the zone of interest for this thesis.



### 3.2.1 BCS state

In 1957, Bardeen-Cooper-Schrieffer(BCS) were able to explain the superfluidity by the formation of pairs of electrons (Cooper pairs) [17]. In that case, the interactions between fermions is weakly attractive and the scattering length is negative. These pairs are much larger than the interparticle spacing, consequently a strong spacing overlap, the binding energy is calculate to be  $\Delta = 2k_B T_D e^{-1/\rho_F |V|}$  where  $\rho_F = mk_F/2\pi^2\hbar^2$  is the density of state at the Fermi energy [37],  $T_D$  the Debye temperature, and  $V$  the potential between the particles (phonon-mediated electron-electron interaction). To realise a BCS state with cold atoms, a spin mixture of two different hyperfine states of  $^6\text{Li}$  is realised, and the potential is created by sweeping the Feshbach field to the negative scattering length side where the interaction becomes attractive, i.e. on the BCS side.

### 3.2.2 BEC-BCS crossover

The crossover between the molecular BEC and BCS state represents a very interesting subject of study, in that regime the interactions are very high because the scattering length diverges, and the pair size of comparable to the interparticle distance, this properties are shared with some High- $T_c$  superconductors [38, 39] or system like neutron stars. Also, when the scattering length diverges, the only important length becomes the interparicles length, and the relevant energy length is the Fermi energy  $E_F$ , the system is called universal [40]. It means that the following quantities related to the energy, the mean energy of the gas, the binding energy of the pairs and the temperature must be related to the Fermi energy by universal numerical constants, and the size of a pair of Fermions is equal to an universal constant times the interparticle distance [15].

### 3.2.3 Thermal and condensate molecules

In this thesis the work is focused on the production and analysis of Feshbach molecules. There are three ways to produce Feshbach molecules; the photoassociation [41, 42] where two colliding atoms are optically excited to a bound state, the sweep of the magnetic field from weakly paired molecules (BCS side) to the tightly bound molecules (BEC side), and finally the one that we use in our experiment, the three body recombination [43, 44]. In the last method, the magnetic field is kept constant and set on the BEC side of the Feshbach resonance where a molecular state exists. During the collisions of three particles, two can form a molecule and the other one take the excess of energy, on the other hand a particle can also collide with a molecule and dissociate it. These processes are summarized in the following equation [45]:

$$\frac{N_{mol}}{N_{at}} = D e^{-E_b/k_B T} \quad (3.24)$$

where  $D$  is phase space density, and  $E_b$  the binding energy of the molecular bound state defined by [46]:

$$E_b = \frac{\hbar^2}{ma^2} \quad (3.25)$$

To be valid, the scattering length must be larger than the extent of the Van der Waals potential, with the characteristic distance:

$$r_{\text{eff}} = \left( \frac{mC_6}{\hbar^2} \right)^{1/4}. \quad (3.26)$$

For lithium, the Van der Waals coefficient is  $1.3340 \times 10^{-76} \text{Jm}^6$  [47], giving a  $r_{\text{eff}} = 62.5a_0$ . For the values of scattering length smaller than  $r_{\text{eff}}$ , a correction can be found [48]:

$$E_b = \frac{\hbar^2}{m(a - \bar{a})^2}, \quad (3.27)$$

with

$$\bar{a} = \frac{\Gamma(3/4)}{2\sqrt{2}\Gamma(5/4)} r_{\text{eff}} \approx 0.478 r_{\text{eff}}. \quad (3.28)$$

Where  $\Gamma(x)$  is the mathematical Gamma function. The properties of the lithium molecular bound state have been studied in [49, 50]. To cool down the molecules to degeneracy temperature, we use evaporative cooling (see section 5.4). A high collision rate is necessary for the thermalisation, which depends on the trapping frequencies, the scattering length between molecules and on the molecules density. Compared to the single atoms, the density of the molecules is divided by two, the scattering length between molecules is given by [50]:

$$a_m = 0.6a. \quad (3.29)$$

According to [50], the process where a tightly bound molecules is created after a collision between a molecules and a particles is suppressed in the case of fermions ( $^6\text{Li}$  in our experiment).

# Chapter 4

## Basics of cold atoms physics

In this chapter, we present the basic concepts necessary to understand the building blocks of our experiment. We first discuss the nature of the atoms that are used, then discuss the way the atoms interact with a magnetic field. Afterwards, we describe their interaction with an electric field through the concept of dipole force [51], which allow us to trap atoms in a deep attractive potential or repel them with a repulsive potential. It is followed by a discussion on how pairs of atoms interact, and finally we will discuss the phenomena of Feshbach resonance[28], allowing us to control the interaction between atoms.

### 4.1 Alkali atoms

In the past twenty years, the development of cooling methods has lead to an original way of reaching the ultra-low temperature regime [3, 52], mostly by using exchange of momentum between light and matter[51, 53, 54] and evaporative cooling methods [55] to reach Bose-Einstein condensation. These cooling methods require powerful laser source. The most reliable and powerful laser sources are in the visible or near infra-red spectrum range. Therefore, on an experimental point of view, the choice of the atoms has been naturally oriented toward alkali atoms that have an electromagnetic spectrum in that range. Moreover, the alkali metals share a common

property of having one electron unpaired on their outer shell. We remind that electrons are fermions, consequently they respect the exclusion principle of Pauli, two electrons cannot have the same quantum state  $|n, l, m_l, m_s\rangle$  where:

$$n = 1, 2, \dots \quad l = 0, 1, \dots, n-1 \quad m_l = -l, \dots, l, \quad m_s = -1/2, +1/2, \quad (4.1)$$

(principal, azimuthal, magnetic, spin numbers respectively). First, we introduce the weakly relativistic Hamiltonian for an hydrogen atom. This Hamiltonian comes from the Dirac's relativistic equation, that satisfies the postulate of quantum mechanics and special relativity. If we look at the typical constants of the system, we can define a typical velocity for the lowest level of the hydrogen atom with,  $v = \frac{e^2}{\hbar}$  that we now compare to  $c$ , the speed of light to give  $\alpha = \frac{e^2}{\hbar c} = \frac{1}{137}$ , the fine structure constant which is  $\ll 1$ , therefore the weakly relativistic regime is justified. The weakly relativistic Hamiltonian is given by [27, 56]:

$$H_0 = m_e c^2 + \underbrace{\frac{\mathbf{P}^2}{2m_e} + V(r)}_{H_0} - \frac{\mathbf{P}^4}{8m_e^3 c^2} + \underbrace{\frac{1}{2m_e^3 c^2} \frac{1}{r} \frac{dV(r)}{dr} \mathbf{L} \cdot \mathbf{S}}_{W_{SO}} + \frac{\hbar^2}{8m_e^2 c^2} \Delta V(r) + \dots \quad (4.2)$$

In addition of the  $H_0$ , we are going to give a particular attention to the term  $W_{SO}$ , the physical meaning of this term is relativistic. The Lorentz boost deforms the electric charge distribution of the valence electron, creating a net magnetic field that interacts with its spin, so called spin-orbit interaction. Its relative intensity is  $\frac{W_{SO}}{H_0} \approx \alpha^2$ . We define the fine structure operator  $\hat{\mathbf{J}} = \hat{\mathbf{L}} + \hat{\mathbf{S}}$ , the eigenstates are now written as linear combination of  $|n, l, s, j, m_j\rangle$ . To get the expectation value of the spin-orbit interaction we use :

$$\begin{aligned} \langle l \ s \ j \ m_j | \hat{\mathbf{L}} \cdot \hat{\mathbf{S}} | l \ s \ j \ m_j \rangle &= \frac{1}{2} \langle l \ s \ j \ m_j | \hat{\mathbf{J}}^2 - \hat{\mathbf{S}}^2 - \hat{\mathbf{L}}^2 | l \ s \ j \ m_j \rangle \\ &= \frac{1}{2} [j(j+1) - l(l+1) - s(s+1)] \end{aligned} \quad (4.3)$$

Finally, we are going to consider the interaction of the magnetic moment of the valence electron with the magnetic moment of the nucleus. This effect is approximately 2000 times weaker than the fine structure effect. However, this level of

accuracy is needed for cold atoms experiments. We define the hyperfine structure operator  $\hat{\mathbf{F}} = \hat{\mathbf{I}} + \hat{\mathbf{J}}$ , with  $\hat{\mathbf{I}}$ , the spin observable of the nucleus. The operator  $\hat{\mathbf{F}}$  is diagonal in the  $|n, l, s, j, i, f, m_f\rangle$ . The corresponding value of the hyperfine interaction is :

$$\begin{aligned} \langle l s j i f m_f | \hat{\mathbf{I}} \cdot \hat{\mathbf{S}} | l s j i f m_f \rangle &= \frac{1}{2} \langle l s j i f m_f | \hat{\mathbf{F}}^2 - \hat{\mathbf{I}}^2 - \hat{\mathbf{S}}^2 | l s j i f m_f \rangle \\ &= \frac{1}{2} [f(f+1) - i(i+1) - s(s+1)] \end{aligned} \quad (4.4)$$

However for alkalis atoms, the term  $H_0$  is more complex, if the atom has  $N$  electrons, the Coulomb potential of a charge  $Ze$  gives us:

$$H = \sum_{i=1}^N \left[ \frac{\hbar^2}{2m} \nabla_i^2 - \frac{Ze^2/4\pi\epsilon_0}{r_i} + \sum_{j>i}^N \frac{e^2/4\pi\epsilon_0}{r_{ij}} \right]. \quad (4.5)$$

The first term is the kinetic energy, the second the potential energy for each electron in the Coulomb field of the nucleus of charge  $Z$ . The term including the denominator  $r_{ij} = |\mathbf{r}_i - \mathbf{r}_j|$  is the electrostatic repulsion between the electrons  $i$  and  $j$ . However for atoms with  $Z > 1$ , this equation can't be solved analytically. A first approximation called the quantum defects [57] gives a good approximation of the energy level of the outer electron:

$$E(n, l) = -hc \frac{R_\infty}{(n - \delta_l)^2}, \quad (4.6)$$

where  $\delta_l$  the quantum defect number,  $R_\infty$  the Rydberg constant and  $n$  the principal quantum number. Now if we want to consider all the electrons, an other approximations have to be made. In a closed shell, for a given  $l$  the sum of all the  $m_l$  values will give zero. This implies a total angular momentum  $\mathbf{L} = 0$  for closed shells. The charge has a spherical symmetry, thus the interaction between the subshells and the valence electrons also have a spherical symmetry. The potential is then approximated by an effective central potential, the Hamiltonian is then given by eq.(4.7)[56], and this approximation is called the **central field (CF) approximation**.

$$H_0 = \frac{\mathbf{p}^2}{2m_e} + V_{\text{eff}}(r), \quad (4.7)$$

with  $\mathbf{p}$  the momentum of the valence electron,  $m_e$  its mass and  $V_{\text{eff}}$  the effective central potential (Fig. 4.1).

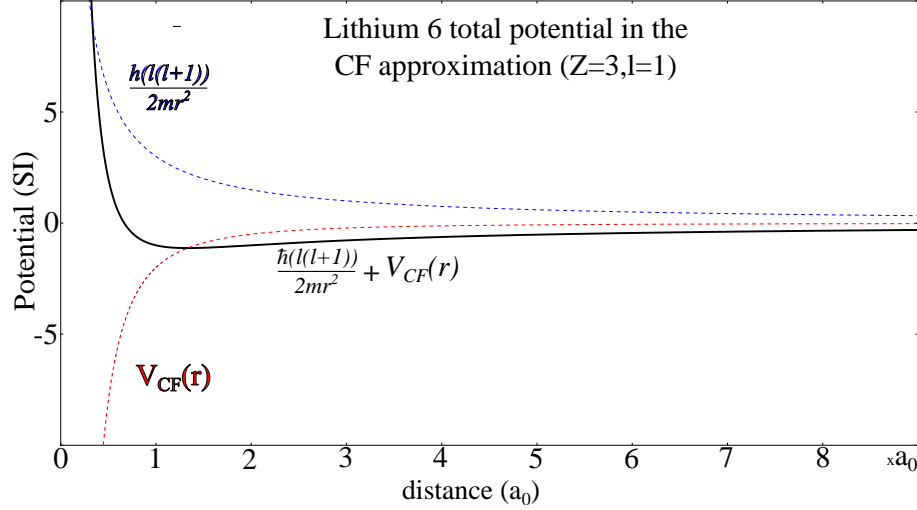


Figure 4.1: Central effective potential in the central field approximation. The blue dotted line represents the repulsive centrifugal barrier ( $k_B \times 7\text{mK}$  for lithium [58]). The red dotted line represents the attractive potential. The black line is the central effective potential. Due to the small number of electron in the  ${}^6\text{Li}$ , the screening is relatively small.

In our experiment, we use two species, the Lithium 6 and the Caesium 133, but in this thesis we are going to mainly discuss the  ${}^6\text{Li}$ . The energy levels are of the ground state and excited states used in the experiment are described in the following figure:

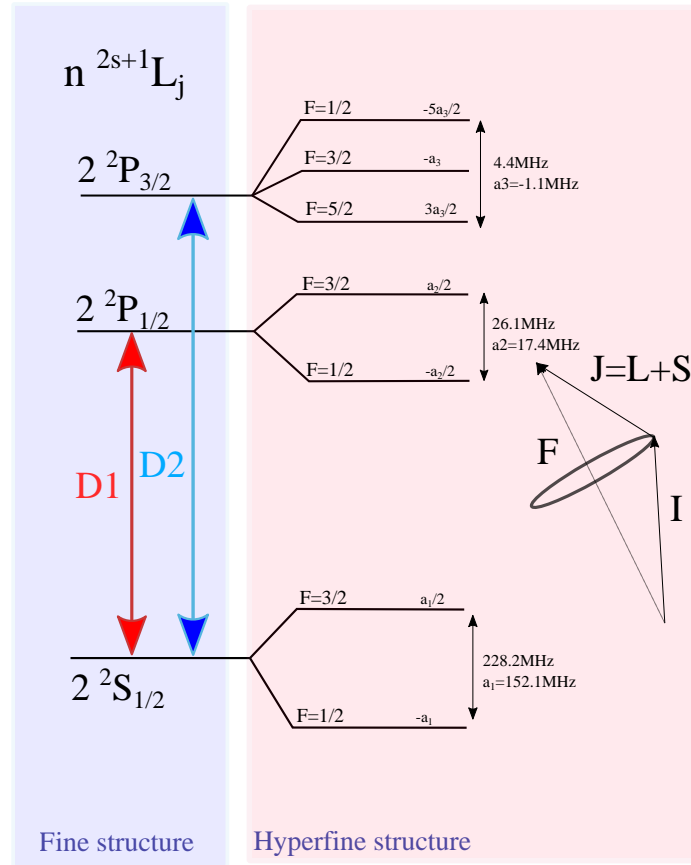


Figure 4.2: Diagram of the ground and 2P excited states of  ${}^6\text{Li}$ . Splitting energies are not to scale. D1 line = 670.993421nm and D2 line = 670.977338nm. Numbers from [59].

## 4.2 Interaction between atoms and a magnetic field

Each of the hyperfine energy levels ( $\mathbf{F}$ ) have a degeneracy of  $2F+1$ . To break the degeneracy, we apply an external magnetic field  $B_z$  along a specific direction (the



$z$ -axis) called the quantization axis. This magnetic field interacts with the magnetic moments ( $\mathbf{I}, \mathbf{L}, \mathbf{S}$ ) of the atoms (see Fig. 4.3). The Hamiltonian of this interaction is:

$$\begin{aligned} H_B &= -\frac{\mu_B}{\hbar}(g_S \mathbf{S} + g_L \mathbf{L} + g_I \mathbf{I}) \cdot \mathbf{B} \\ &= -\frac{\mu_B B}{\hbar}(g_S S_z + g_L L_z + g_I I_z), \end{aligned} \quad (4.8)$$

projected on the atomic quantization axis. Where  $g_S, g_I$  and  $g_L$  are respectively the  $g$ -factors of the electron spin, nuclear, and electron orbital. In eq.(4.8), the amplitude of the Hamiltonian depends on the strength of the magnetic field. We can separate the problem into three regimes: **low field** or **Zeeman regime**, where the magnetic field is treated as a perturbation; **high field** or **PaschenBack regime**, where the projection of the magnetic field on the  $z$ -axis  $Bz$  is large and the hyperfine structure becomes the perturbation. Finally, the **intermediate** or **Breit-Rabi regime** where the effects have a comparable strength. We now define the Hamiltonian including the hyperfine structure and the coupling terms with the external fields:

$$H_{hfs} = \frac{A_{hfs}}{\hbar^2} \mathbf{I} \cdot \mathbf{J} - \frac{\mu_B B}{\hbar}(g_S S_z + g_J J_z + g_I I_z), \quad (4.9)$$

where  $A_{hfs}$  is the magnetic dipole constant. We can neglect the term with  $\mu_I$  as it is  $\approx 2000$  times smaller than the two others [60]. There is a analytical solution to diagonalise this Hamiltonian in the subspace of  $l = 0$ . This give a good approximation for the high and low field regime. However, in our experiment we use the whole range of magnetic field intensity during high field imaging (see section 5.5.4) of the atomic cloud and the determination of the inter-atomic interaction strength. Therefore, a numerical solution is outlined here. The basis used for our calculation is  $|l \ s \ j \ m_j \ i \ m_i\rangle$ . We rewrite the hyperfine term of the Hamiltonian as:

$$\mathbf{I} \cdot \mathbf{J} = I_z J_z + \frac{1}{2} [I_+ J_- + J_+ I_-], \quad (4.10)$$

so it can be applied to the chosen basis. However, the operators  $L_z$  and  $S_z$  are not diagonal in that basis. The basis is then written as a linear combination of

$|l s j m_j i m_i\rangle$ , using their completeness relation:

$$L_z |l s j m_j\rangle = \sum_{m_l, m_s} m_l |l s j m_j\rangle \underbrace{\langle l m_l s m_s | l s j m_j \rangle}_{\text{CB1}}, \quad (4.11)$$

where **CB1** is a Clebsch-Gordan coefficient. By applying another bra to eq.(4.11), we find another value of the matrix and the corresponding Clebsch-Gordan coefficient.

$$\langle l m_l j' m'_j | L_z | l s j m_j \rangle = \sum_{m_l, m_s} m_l \underbrace{\langle l m_l j' m'_j | l s j m_j \rangle}_{\text{CB1}} \underbrace{\langle l m_l s m_s | l s j m_j \rangle}_{\text{CB2}}, \quad (4.12)$$

This allow us to calculate the energy levels of the  ${}^6\text{Li}$  atoms depending on the magnetic field in Fig. 4.4 and Fig. 4.5.

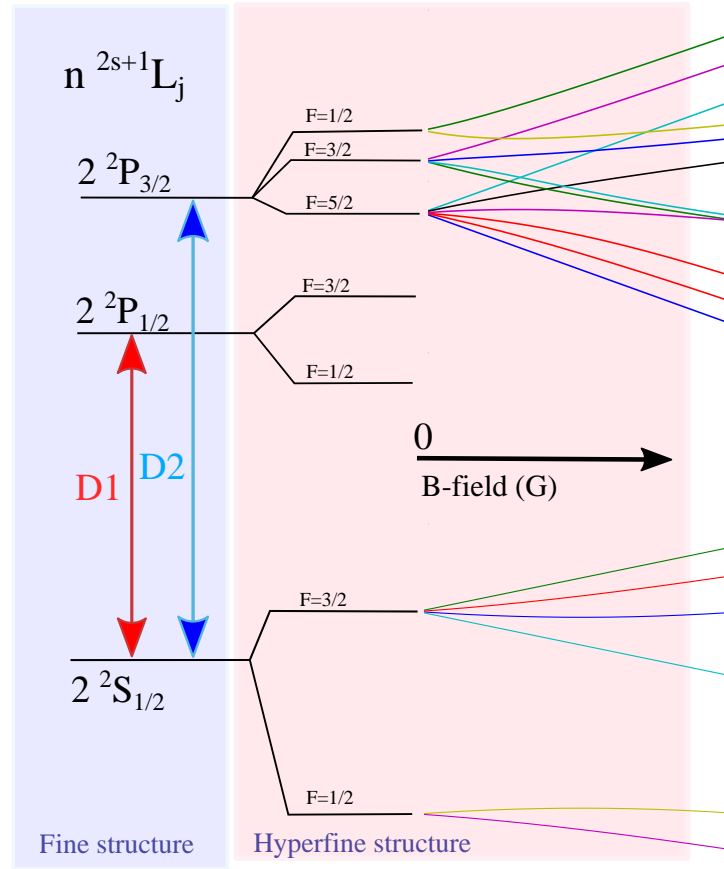
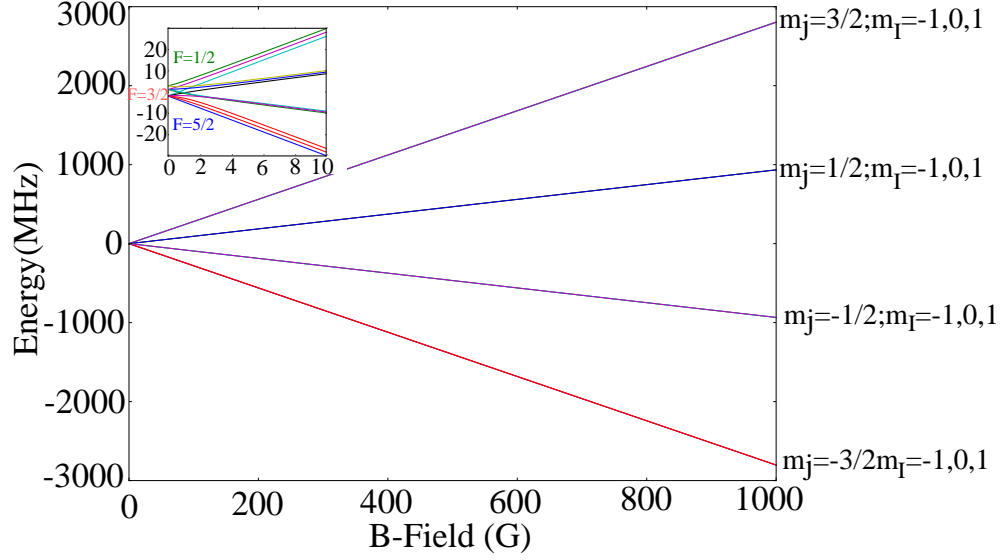
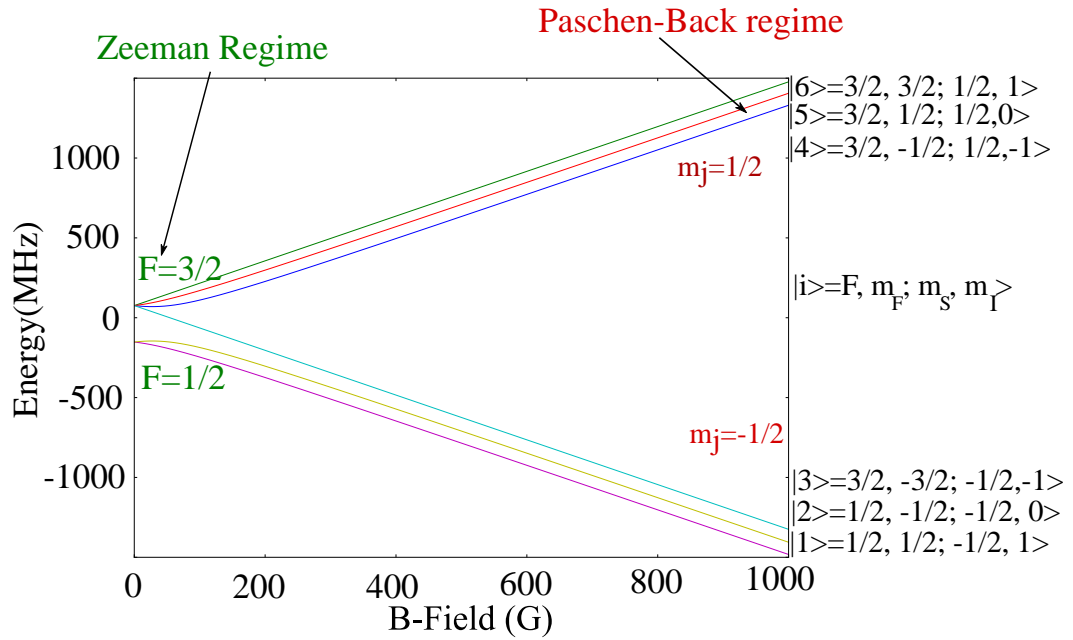


Figure 4.3: Diagram of the ground state and the 2P excited states of  ${}^6\text{Li}$ , the coloured lines represent the splitting of the hyperfine structure in the presence of a magnetic field  $B$ . Energy splitting is not to scale.

Figure 4.4: Breit Rabi diagram of the  ${}^6\text{Li}$  atom excited state  $2P_{3/2}$ .Figure 4.5: Breit Rabi diagram of the  ${}^6\text{Li}$  atom ground state  $2S_{1/2}$ .

### 4.3 Interaction between atoms and light

In this section, we discuss the effect of light on atoms. The light can interact with atoms in a conservative and a dissipative way. The conservative force is called dipole force, and is due to the interaction of the electric dipole induced by the light with the light field. This interaction causes a change in the potential energy of the atom (AC Stark Shift[61]) depending on the intensity and detuning of the light. The dipole force is used to draw a potential landscape to trap the atoms (see section 5.4.2). On a other hand, the scattering force which is dissipative is related to the momentum transfer between the absorption of photons and the spontaneous emissions is an essential tool for the Zeeman slower (see section 5.2) and Magneto-optical trap (see section 5.3). We start by a demonstration to obtain the expression of the dipole force potential using a two level-atom description and assuming that the light field is far detuned from the atomic transition which is the case for the trapping of neutral atoms, therefore that the population of the excited state is negligible. From that, we derive the expression for the scattering force using the rotating wave approximation where frequency of the light field is assumed to be closed to the resonance, consequently involving absorption emission processes.

#### 4.3.1 The dipole force

We start by a description of the semi-classical model, i.e. a classical description of the atomic motion and a quantum treatment of the internal dynamics of the atom. We first derive the expression of the dipole force without using the rotating wave approximation, because this approximation leads to inaccuracy when the frequency of the laser is far detuned from the atomic transition. Then, we will apply the model to a more realistic situation with to alkali atoms. Elements of this discussion can be found in [57, 62].

The most basic situation is to consider the interaction of linearly polarised light travelling along the  $z$ -axis with a two-level atom as shown in Fig. 4.6.

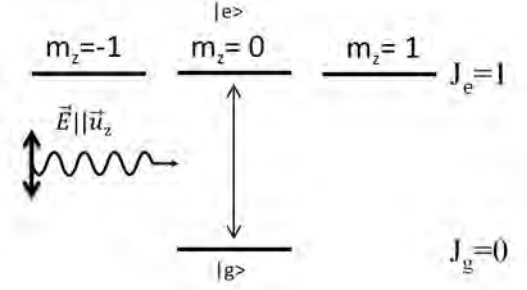


Figure 4.6: The two-level atom model, with the angular momentum  $J_g = 0$  in the ground state, and  $J_e = 1$  in the excited state.

The monochromatic electromagnetic field  $\mathbf{E} = \epsilon E(\mathbf{r}) \cos[\omega t - \phi(\mathbf{r})]$ <sup>1</sup>, with a linear polarization  $\vec{\epsilon}$  along the  $z$ -axis and a frequency  $\omega$  couples the ground state  $|g, J_g = 0\rangle$  to the excited state  $|e, J_e = 1, m_z = 0\rangle$ . We introduce the detuning  $\Delta = \omega - \omega_0$ , where  $\omega_0$  is the resonance frequency of the transition. The operator dipole electric  $\hat{\mathbf{D}}_{d,e}$  that induce a coupling between the internal states of the atom the light is defined by:

$$\hat{V}_{d,e} = -\hat{\mathbf{D}} \cdot \mathbf{E}(\mathbf{r}, t) \quad (4.13)$$

$$= d_0 E(\mathbf{r}) (\underbrace{|e\rangle\langle g|}_{\sigma+} + \underbrace{|g\rangle\langle e|}_{\sigma-}) \cos[\omega t - \phi(\mathbf{r})] \quad (4.14)$$

where we introduce the ascending and descending operator  $\sigma+$  and  $\sigma-$ . These operator mixes the ground state  $|g\rangle$  and  $|e\rangle$ , with  $d_0$  the intensity of the coupling depending on the transition. Now, as we are in the semi-classical approach, we can define a momentum and a position to the atom without incorporating the Heisenberg principle. We want to work out is the average force  $\overline{\langle \mathbf{F}(\mathbf{r}), t \rangle}_{intern}$  of a motionless atom. The term average hides two different means, the first one, the average on the stationary internal states, oscillating between  $|e\rangle$  and  $|g\rangle$  before reaching a stationary value. Secondly, a trivial average on time. We define the operator force:

$$\hat{F}(\mathbf{r}, t) = -\nabla [\hat{V}_{dip.elec}(\mathbf{r}, t)] = \hat{D} \nabla [E(\mathbf{r}) \cos[\omega t - \phi(\mathbf{r})]], \quad (4.15)$$

<sup>1</sup>Bold font is used to define a vector.

therefore, to get the average of  $\hat{F}$ , we need to work out the average on the internal state of  $\hat{D}$  given by:

$$d(\mathbf{r}, t) = \langle \hat{D} \rangle_{intern} = \text{Tr} \left( \hat{\rho}(\mathbf{r}, t) \hat{D} \right), \quad (4.16)$$

where  $\hat{\rho}(\mathbf{r}, t)$  is the density matrix ( $2 \times 2$ ) in stationary regime. The goal of this demonstration is to write  $d(\mathbf{r}, t)$  with this form:

$$\mathbf{d}(\mathbf{r}, t) = \alpha(\omega) \mathbf{E}(\mathbf{r}, t) = d_0 \left[ \underbrace{\text{Tr}(|e\rangle\langle g| \rho(\mathbf{r}, t))}_{\rho_{ge}} + \underbrace{\text{Tr}(|g\rangle\langle e| \rho(\mathbf{r}, t))}_{\rho_{eg}} \right], \quad (4.17)$$

where  $\alpha(\omega)$  is the polarisability. Therefore, we can write the average force eq.(4.15):

$$\langle \hat{F} \rangle (\mathbf{r}, t) = d(\mathbf{r}, t) \nabla E(\mathbf{r}, t), \quad (4.18)$$

and using eq.(4.17) we can write the average force in following form:

$$\langle \hat{F} \rangle (\mathbf{r}, t) = \frac{1}{2} \alpha(\omega) \nabla (E^2(\mathbf{r}, t)), \quad (4.19)$$

knowing that:

$$\langle \hat{F} \rangle (\mathbf{r}, t) = -\nabla (V_{dip}(\mathbf{r}, t)) \quad (4.20)$$

We finally obtain the expression for dipole potential by averaging over time:

$$V_{dip}(\mathbf{r}) = -\frac{1}{2} \alpha(\omega) \overline{\mathbf{E}^2(\mathbf{r}, t)} = -\frac{1}{4} \alpha(\omega) E^2(\mathbf{r}). \quad (4.21)$$

We can already, see the form of the dipole force potential depending spatially on the intensity of the electric field. Now, to obtain  $\alpha(\omega)$ , we are going to use the following evolution equation [51]:

$$i\hbar \frac{d\hat{\rho}}{dt} = [\hat{H}, \hat{\rho}] + i\hbar \frac{d\rho}{dt} \Big|_{\text{spontaneous emission}}, \quad (4.22)$$

which is the equivalent of the Schrodinger's equation for a density matrix, where we add a dissipative term due to spontaneous emission. We introduce the Rabi frequency  $\Omega$ :

$$\hbar\Omega = -d_0 E(\mathbf{r}). \quad (4.23)$$

We assume a weak field approximation where  $\rho_{gg} \approx 1$  and  $\rho_{ee} \approx 0$ , this approximation is correct if  $\Omega \ll \Delta, \Gamma$ . The values of the dissipative terms are then given by[62]:

$$i\hbar \frac{d\rho_{eg}}{dt} \Big|_{sp} = -\frac{\Gamma}{2} \rho_{eg} \quad (4.24)$$

$$i\hbar \frac{d\rho_{ge}}{dt} \Big|_{sp} = \frac{\Gamma}{2} \rho_{ge}, \quad (4.25)$$

where  $\Gamma$  is the natural width of the excited state  $|e\rangle$ , and  $\Gamma^{-1}$  the lifetime of the excited state. Moreover, we define the Hamiltonian of the the system, and suppose that the energy of the ground state is zero. This is given by:

$$\hat{H} = \hbar\omega_0 |e\rangle\langle e| - \hat{D}E(\mathbf{r}, t) \quad (4.26)$$

Now, if we insert this Hamiltonian eq.(4.26) in the eq.(4.22), we can obtain the evolution of  $\rho_{eg}$  for example:

$$i\hbar \frac{d\rho_{eg}}{dt} = \hbar(\omega_0 - \frac{i\Gamma}{2})\rho_{eg} - d_0 E(\mathbf{r}, t)(\rho_{eg} - \rho_{ee}). \quad (4.27)$$

There is no analytical solution to this problem. Therefore, using  $\rho_{gg} \approx 1$  and  $\rho_{ee} \approx 0$ , the result of the integration of eq.(4.27) gives:

$$\rho_{eg}(t) = \frac{\Omega}{2} \left[ \frac{e^{-i(\omega t - \phi)}}{\omega - \omega_0 + \frac{i\Gamma}{2}} + \frac{e^{i(\omega t - \phi)}}{\omega + \omega_0 - \frac{i\Gamma}{2}} \right], \quad (4.28)$$

$$\rho_{ge} = \rho_{eg}^*. \quad (4.29)$$

The laser used for the dipole trap are far detuned from the atomic transition, i.e.  $\Delta \gg i\frac{\Gamma}{2}$ , then we neglect the term  $i\frac{\Gamma}{2}$  in eq.(4.28). Now, we can rewrite eq.(4.17) using eq.(4.28):

$$\begin{aligned} \mathbf{d}(\mathbf{r}, t) &= d_0 2\Re(\rho_{ge}) \\ &= -\frac{d_0}{\hbar\Delta} E(\mathbf{r}) \cos(\omega t - \phi(\mathbf{r})) \end{aligned} \quad (4.30)$$

$$= \alpha(\omega) \mathbf{E}(\mathbf{r}, t) \quad (4.31)$$



where the detuning  $\overline{\Delta}$  that include both the resonant and the non-resonant term is given by:

$$\frac{1}{\overline{\Delta}} = \frac{1}{(\omega - \omega_0)} + \frac{1}{(\omega + \omega_0)}. \quad (4.32)$$

We have the following expression of the **dipole potential** using eqs.(4.17, 4.21, 4.28):

$$V_{dip}(\mathbf{r}) = \frac{\hbar\Omega}{4\overline{\Delta}} = \frac{1}{4} \frac{d_0^2}{\hbar\overline{\Delta}} I(\mathbf{r}). \quad (4.33)$$

Therefore, by using  $\overline{\Delta} < 0$  (red detuning), the atoms will be attracted by the high intensity region. On the other hand, by using  $\overline{\Delta} > 0$  (blue detuning) the atoms will be repelled by high intensity region.

## Alkali atoms

In our case, the wavelength for the  ${}^6\text{Li}$  D<sub>2</sub> line is  $\lambda_0 = 671\text{nm}$  and the wavelength of the dipole laser is  $\lambda = 1064\text{ nm}$ . Therefore, the non-resonant term of  $\overline{\Delta}$  has an influence on the results. For  $\Delta < 0$  it reinforces the action of the 1064nm laser by 22%, and for  $\Delta > 0$  reduces the action of the 532nm laser (see chapter 7) by 11% on lithium. The resonant would have been neglected in the rotating wave approximation.

Now, we consider a more realistic structure, including the interaction of the laser with the D<sub>1</sub> and D<sub>2</sub> lines (see Fig. 4.2). The hyperfine structure, particularly the one of the Lithium is very small compared to the detuning of the light field from the resonance, therefore we only include terms of the fine structure. Using the coefficient of Clebsch-Gordan in Fig. 4.7 we have a new expression for the detuning:

$$\frac{1}{\overline{\Delta}} = \frac{1}{3} \left( \frac{1}{\overline{\Delta}_1} + \frac{2}{\overline{\Delta}_2} \right). \quad (4.34)$$

where  $\overline{\Delta}_1$  and  $\overline{\Delta}_2$  are the detuning of the lines D<sub>1</sub> and D<sub>2</sub>.

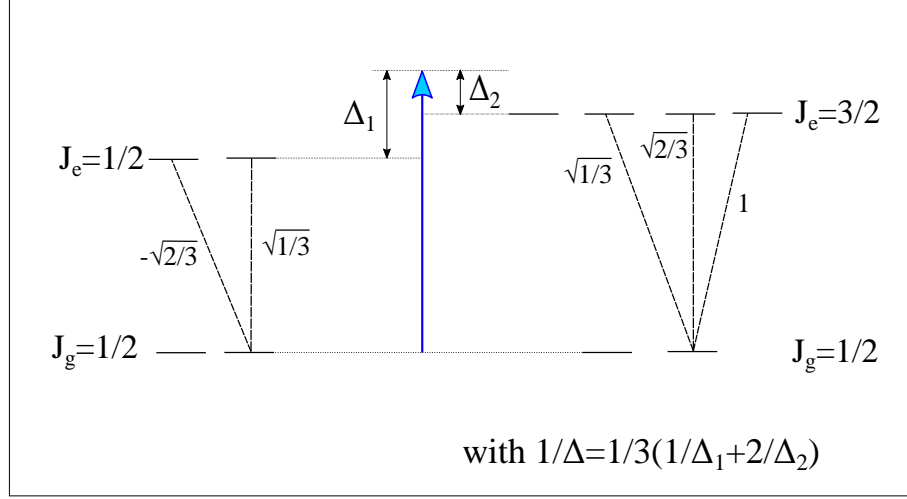


Figure 4.7: Fine structure of an alkali atom, and detuning for dipole trap calculation.

### 4.3.2 The scattering force

However, there is another force, the scattering force, which is time dependant on the gradient of the phase:

$$\mathbf{f}_{\text{scat}} = -(\epsilon \cdot \mathbf{d}) E [\nabla \phi(\mathbf{r})] \sin(\omega t - \phi) \quad (4.35)$$

In our calculation, this force is null in the first order of  $\frac{1}{\Delta}$ , i.e. that we neglect  $i\Gamma/2$  in eq.(4.28). Consequently, if we want the average force  $f_{\text{scat}}$  to be different from zero, because of the sine that appeared in eq.(4.35), the induced dipole has to be out of phase with the field. This is done by developing the spontaneous emission term at the second order in  $1/\Delta$ :

$$\frac{1}{\omega - \omega_0 - \frac{i\Gamma}{2}} \approx \frac{1}{\omega - \omega_0} - i \frac{\Gamma/2}{(\omega - \omega_0)^2} \quad (4.36)$$

However, in cold atom physics, it is common to use the rotating frame approximation, which use the fact that  $|\Delta| \ll \omega_0$ , i.e  $\bar{\Delta} \approx \Delta$ . This approximation simplifies the calculation if we take from the beginning:

$$\hat{V}_{d.e}^{rwa} = \frac{\hbar\Omega}{2} [\hat{\sigma}_+ e^{-i(\omega t - \phi)} + \hat{\sigma}_- e^{i(\omega t - \phi)}] . \quad (4.37)$$

It allows us to find analytical solution to eq.(4.27), without supposing that  $\rho_{gg} \approx 1$  and  $\rho_{ee} \approx 0$ . This approximation gives the following useful quantities :

$$\rho_{ee} = \frac{|\Omega|^2/\Gamma^2}{1 + (2\Delta/\Gamma)^2 + 2|\Omega|^2/\Gamma^2}, \quad (4.38)$$

and

$$\rho_{eg}^* = -\frac{i\Omega}{\Gamma} \frac{1 + 2i\Delta/\Gamma}{1 + (2\Delta/\Gamma)^2 + 2|\Omega|^2/\Gamma^2}, \quad (4.39)$$

also developing eq.(4.35) gives us an expression for the time-averaged scattering force :

$$\langle F_{\text{scat}} \rangle = \frac{\Gamma}{2} \frac{I/I_{\text{sat}}}{1 + (2\delta/\Gamma)^2 + I/I_{\text{sat}}} \hbar \nabla \phi = R_{\text{sc}} \hbar \nabla \phi \quad (4.40)$$

The vector  $\nabla \phi$  points in the direction of the travel of the wave-front. For a plane wave  $\phi = \mathbf{k} \cdot \mathbf{r}$ , therefore  $\nabla \phi = k$ .  $\langle F_{\text{scat}} \rangle$  can also be written as the product of scattering rate  $R_{\text{sc}} = \Gamma \rho_{ee}$  and the momentum of a photon  $\hbar k$ . Finally, we write the polarisability  $\alpha$  for the two-level atom in the rotating frame approximation:

$$\alpha = i \frac{c\epsilon_0 \hbar \Gamma}{2_{\text{sat}}} \frac{1 + 2i\delta/\Gamma}{1 + (2\Delta/\Gamma)^2 + I/I_{\text{sat}}} \quad (4.41)$$

where  $I_{\text{sat}}$  is the saturation intensity defined by  $I/I_{\text{sat}} = 2\Omega^2/\Gamma^2$ , a useful quantity often used in experimentation.

# Chapter 5

## Guideline to making a $^6\text{Li}$ BEC

In this chapter, we describe the technology and methods used to achieve a  $^6\text{Li}$  mBEC. The experiment is separated on two tables, the first one contains the lasers appendix C providing the light for the magneto-optical trap (MOT) (see section 5.3) and the imaging (see section 5.5), and the second one contains the main chamber where atoms are cooled down (see Fig. 5.1). We start by the description of the lithium oven, where the atoms are heated up (see section 5.1), then collimated and sent through the Zeeman slower (see section 5.2), where atoms are slowed down before arriving to the main chamber. Once the atoms arrive in the main chamber, they are first load in the MOT (see section 5.3) and cooled down to temperature in the order of  $600\mu\text{K}$ . Then, the atoms are transferred to a deeper trap, so-called dipole trap (see section 5.4), and evaporated while increasing the interactions between atoms to maximize the thermalisation, the final temperature reached is around  $30 - 600\text{nK}$ , at these temperatures the atoms are converted to molecules and the PSD  $D > 1$ , consequently we can observe the formation of a mBEC (see section 3.2.3). Finally, the imaging system (see section 5.5.1) takes 3 absorption pictures to reconstruct the density distribution of the atoms, if we are in the regime of ultra low temperatures and most of the atoms are converted into molecules, the binding energy is set to be low enough adjusting the scattering length so the imaging light can dissociate and image them [63].

The goal of this chapter is to give the up to date parameters and improvements made on the experiment in order to achieve the BEC. During my PhD, I improved the simulations and the methods to calculate the trapping frequencies of optical dipole trap, develop an alternative method to measure the scattering length, and also implement a better power stabilization loop of the dipole trap in order to reach lower temperature. A new AOM controller has been designed allowing us to reach very low power evaporation regime, therefore very low temperature BEC. Moreover, I set up an in situ absorption imaging sequence of the density of the cloud, the densities are studied in the next chapter (see chapter 6). Further technical details about the initial experiment can be found in [63–65].

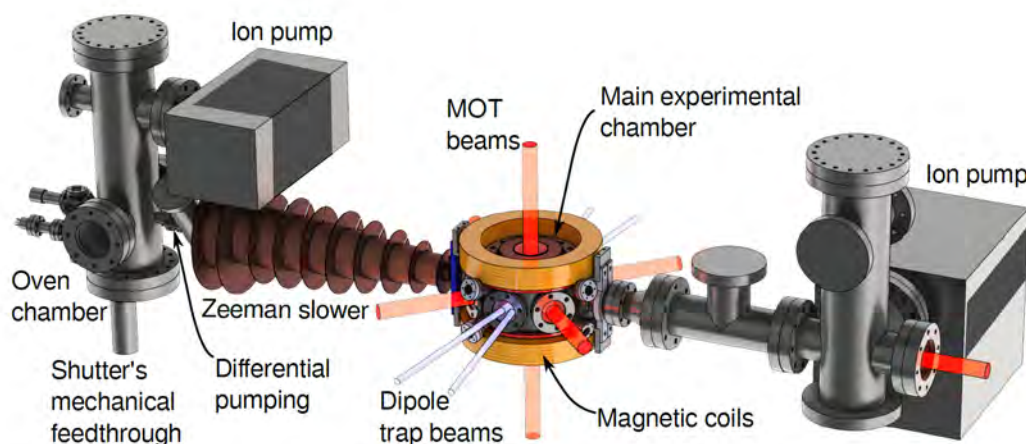


Figure 5.1: Overview of the main part of the experiment where the atoms are cooled down and imaged.

## 5.1 Heating up the atoms

The first step is to obtain an atomic beam, this is done by heating up a lithium chunk from Sigma-Alrich pure at 95% (see Fig. 5.2).

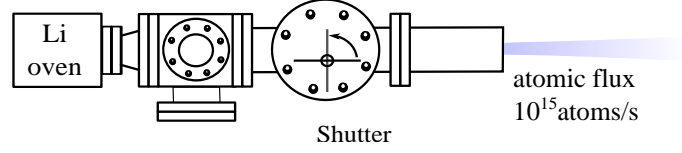


Figure 5.2: Schema of the oven used to heat up the atoms.

The chunk of lithium is heated at a temperature of  $\sim 700\text{K}$  to obtain the required vapour pressure. The vapour pressure of a gas is defined by the Antoine equation [66]:

$$\log_{10}(P) = A - \frac{B}{T + C}, \quad (5.1)$$

where  $P$  is the vapour pressure, and  $A, B$  and  $C$  are known as the Antoine coefficients and can be found in [67] for  ${}^6\text{Li}$ . From eq.(5.1) we can obtain the density using:

$$n = \frac{P}{k_B T}, \quad (5.2)$$

where  $k_B$  is the Boltzmann constant, and the total emitted intensity  $I_{\text{oven}}$ :

$$I_{\text{oven}} = \frac{n \bar{v} A}{4} \approx 10^{15} \text{ atoms/s}, \quad (5.3)$$

with  $\bar{v}$  the mean velocity of the atoms,  $A$  the area of the oven aperture with an atomic density  $n$ . Moreover, a new dual species oven  ${}^6\text{Li}$ - ${}^{133}\text{Cs}$  has been built and soon will replace the current one, this new double species oven is described in appendix G.

## 5.2 Transfer to the main chamber

Once the atoms are emitted from the oven and collimated for the Zeeman slower part (see Fig. 5.3), their temperature reaches  $700\text{K}$ , with a most probable velocity at  $1380\text{m/s}$ . However, the capture velocity for the MOT is about  $230\text{ m/s}$  [51].

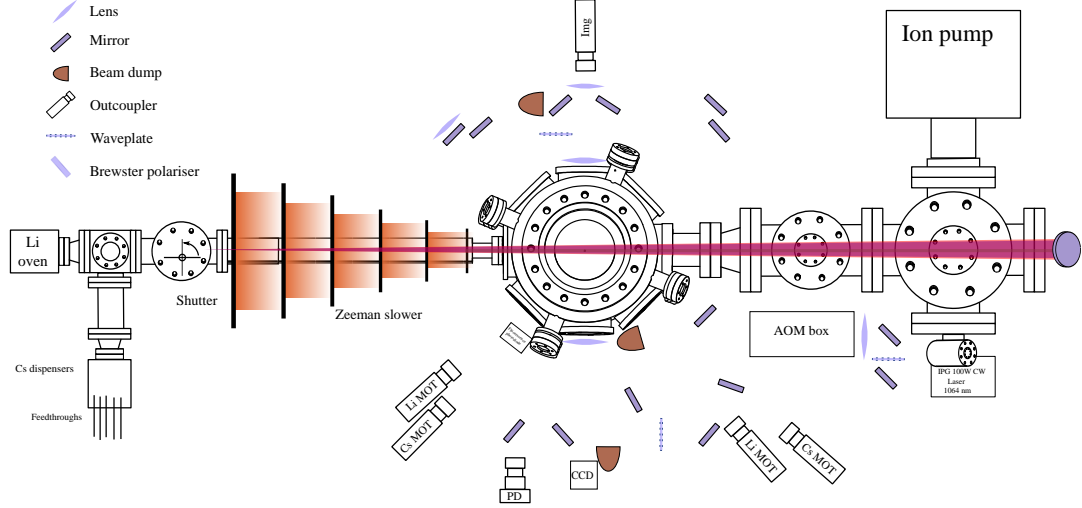


Figure 5.3: General over view of the main part of the experiment including optics. The red focused beam starting from the right hand side illustrate the Zeeman slower beam directed toward the oven.

Therefore, in order to reach that velocity, a resonant beam is shone to the counter propagating direction of the atoms (see Fig 5.3). Although, as the atoms slow down, the **Doppler shift** related to the velocity of the atoms changes and the laser beam is no longer resonant. The principle of the Zeemann slower [68] is to adapt the energy levels by means of a magnetic field to be resonant all along the path. The effective laser detuning  $\delta'$  including the Doppler and magnetic shifts is given by:

$$\delta' = \delta - \frac{\mu B}{\hbar} + kv, \quad (5.4)$$

where  $\mu$  is the magnetic moment of the transition,  $B$  the magnetic field,  $\delta$  the detuning from the transition of an atom in the **lab frame**,  $v$  the velocity of the atoms, and  $k$  the wave number. For the atomic transition and the laser beam to be resonant, the relative detuning must satisfy  $\delta' = 0$ .

For a constant deceleration  $-a_0$  along the path of the atoms  $z$ , the velocity of

the atoms should satisfy :

$$v(z) = \sqrt{v_0^2 - 2a_0 z}, \quad (5.5)$$

where  $v_0$  is the initial velocity of the atoms. Using eqs.(5.4,5.5), we obtain an expression for the magnetic field :

$$B(z) = \frac{\hbar}{\mu} \left( \delta + k \sqrt{v_0^2 - 2a_0 z} \right). \quad (5.6)$$

The value of the deceleration  $a_0$  is determined by the **radiation pressure force**  $F_{\text{scat}}$  (see section 4.3):

$$ma_0 = F_{\text{scat}} = \frac{\Gamma}{2} \frac{I/I_{\text{sat}}}{1 + I/I_{\text{sat}}} \hbar k \quad (5.7)$$

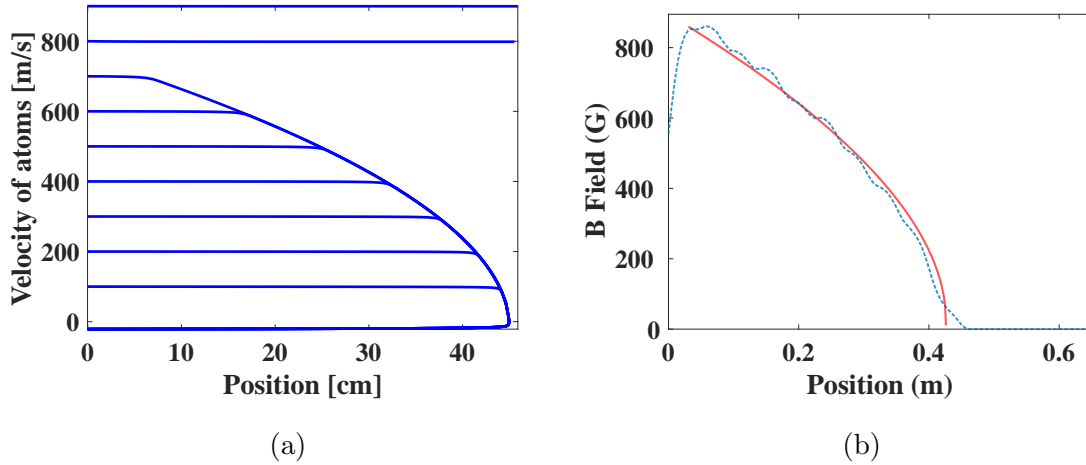


Figure 5.4: a) Simulation of the slowing process of the  ${}^6\text{Li}$  atoms in the Zeeman slower in order to find an optimal magnetic field profile [64]. Atoms are slowed at  $\approx 160 \text{ ms}^{-1}$  at 42cm, the position of the main chamber. The atoms with an initial velocity of  $v > 670 \text{ ms}^{-1}$  are not captured in the slowing process and therefore not decelerated. b) Map of the magnetic field of the Zeemann slower, the red curve is the theoretical plot and the blue dotted line the experimentally measured field.



### 5.3 First cooling in the main chamber

Once the atoms pass through the Zeeman slower, they arrive in the main chamber (see Fig. 5.6). They are loaded in a so-called **magneto-optical trap (MOT)** (see Fig. 5.9) [69], the capture velocity is  $\approx 200\text{ms}^{-1}$ . The cooling process of the atoms is provided by the optical **molasses**, with three counter-propagating beams, producing the cooling and repumping light. The spatial confinement is performed by magnetic coils in an anti-Helmholtz configuration. The sequence shown in Fig. 5.5 starts by switching on all the cooling and repumping lasers for approximately 15s, then diminishing the power of the cooling and repumping laser while increasing the detuning, in order to compress the MOT (see section 5.3.2), reducing the temperature of the cloud from  $2000\mu\text{K}$  to  $600\mu\text{K}$ . The repumper light is switched off 0.3ms before the transfer to the optical trap, to pump the atoms into the  $F=1/2$  state. The dipole laser is switched on 1s before the compression stage to initiate the transfer into the dipole trap. Then the cooling/repumping lights are switched off to transfer the atoms into the dipole trap.

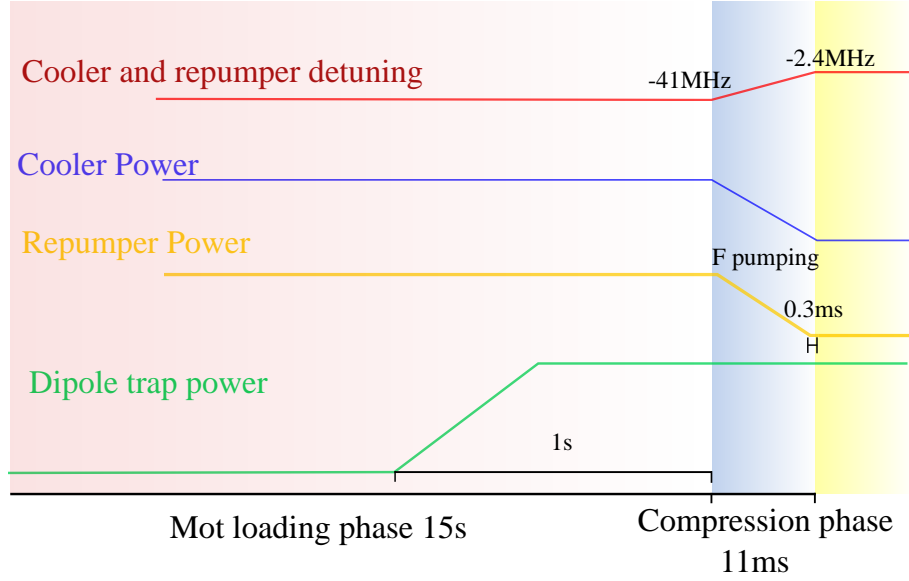


Figure 5.5: Temporal sequence of the MOT stage. First, the loading phase, the cooler and repumper lasers are switched on for 15s, the dipole laser is switched on at the end of the loading sequence to prepare the transfer into the dipole trap. Before the transfer to the dipole trap, the MOT is compressed, the detuning of the cooler and repumper is increased, and the cooler and repumper power are decreased.

### 5.3.1 The magneto-optical Trap (MOT)

The MOT combines the effects of the light and magnetic fields. The light slows down the atoms through **the radiation pressure force**, while a magnetic field gradient is designed to change the shape of the light force in order to push the atoms toward the center. The light force is generated by 3 pairs of counter-propagating laser beams. As mentioned before the light is prepared on a different table and transferred through optical fibres with an optical aperture of  $\text{NA} = 0.12$  to the table containing the main chamber (see Fig. 5.6). At the end of the fibres, outcouplers with  $f = 10\text{mm}$  lenses send the light in the main chamber and the light is retro-reflected on the other side of the chamber. Creating a set of 6 beams in the three directions  $x, y, z$ .

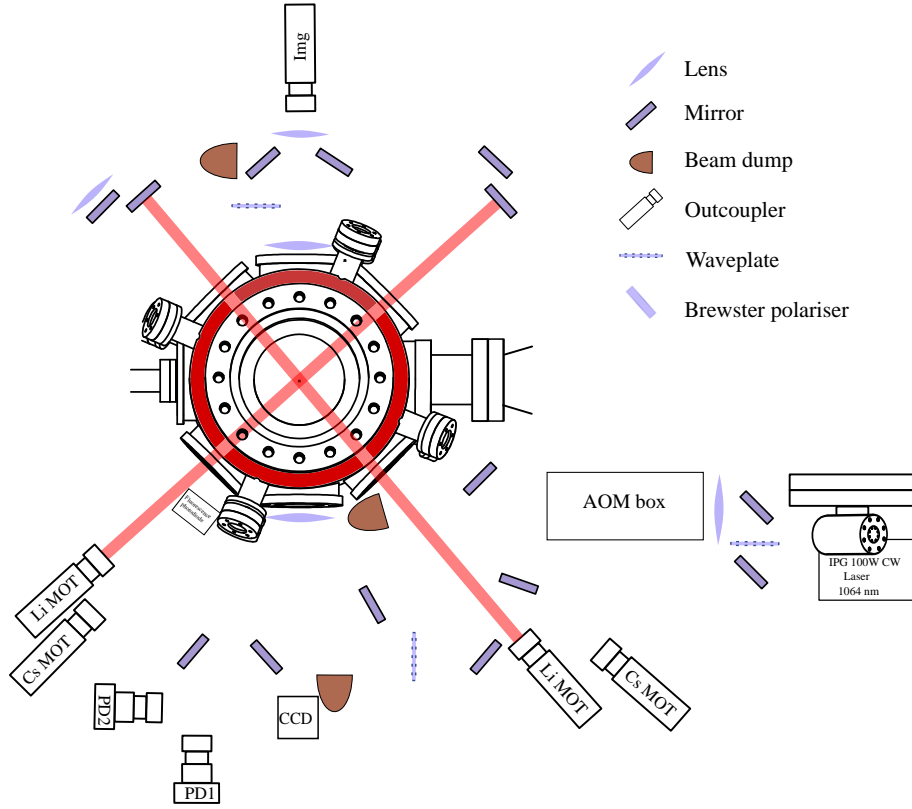


Figure 5.6: Top view of central part of the main chamber. The outcouplers send the lights toward the center of the chamber where the MOT is loaded. At the same time the MOT coils (dark red) are switched on to provide the spatial confinement.

When a pair of counter-propagating beams with the same  $|k|$  number close to resonance and red detuned  $\omega < \omega_0$  are overlapped with an atom of velocity  $v$ , the atoms undergo a ”**molasses**” **force**. Using eq.(4.40), we obtain (assuming  $kv \ll \Gamma$ ) :

$$\begin{aligned} F_{\text{molasses}}(\delta) &= F_{\text{rad}}(\omega - \omega_0 - kv) - F_{\text{rad}}(\omega - \omega_0 + kv) \\ &\approx -2k \frac{dF_{\text{rad}}}{d\delta}(\delta)v = -\gamma(\delta)v. \end{aligned} \quad (5.8)$$

using eq.(4.40) we obtain  $\gamma$  the damping coefficient:

$$\gamma = 4\hbar k^2 \frac{I}{I_{\text{sat}}} \frac{-2\delta\Gamma}{[1 + (\delta/\Gamma)^2]^2}, \quad (5.9)$$

where the term  $I/I_{\text{sat}}$  has been neglected in the denominator, because the validity of optical molasses requires  $I \ll I_{\text{sat}}$  for the force from each beam to act independently [57]. Now to extract a typical time scale of the process we use the 2<sup>nd</sup> Newton's law and eq.(5.8) :

$$\frac{dE}{dt} = \frac{d}{dt} \left( \frac{1}{2} m v_z^2 \right) = v_z F_{\text{mol}} = -\gamma v_z^2 = \frac{2\gamma}{m} E = -\frac{E}{\tau_{\text{damp}}} \quad (5.10)$$

with  $\tau_{\text{damp}}$  on the order of few microseconds.

However, the radiation pressure force provides a damping but it does not trap the atoms. To do so, a magnetic field gradient is added (see Fig. 5.7), this magnetic field gradient shifts the Zeemann sub-levels, represented in Fig. 5.7 b) along the  $x$ -axis. The quantization axis on this figure is chosen to be aligned with the local magnetic field.

If an atom is moving toward the  $-x$  direction, the most probable transition is  $|J = 0, m_J = 0\rangle \rightarrow |J = 0, m_J = +1\rangle$ , and can only be driven by  $\sigma^+$ -light coming from the left side. If an atom is moving toward the  $+x$  direction, the most probable transition is  $|J = 0, m_J = 0\rangle \rightarrow |J = 0, m_J = -1\rangle$ , and can only be driven by  $\sigma^-$ -light coming from the right side. This creates an imbalanced radiative force and pushes the atoms to the center. This force can be described by adding the frequency shift due to the coils in eq.(5.8):

$$\begin{aligned} F_{\text{MOT}} &= F_{\text{scatt}}^{\sigma^+}(\omega - kv - (\omega_0 + \beta z)) - F_{\text{scatt}}^{\sigma^-}(\omega - kv - (\omega_0 - \beta z)) \quad (5.11) \\ &\approx -2 \frac{\partial F}{\partial \omega} kv - 2 \frac{\partial F}{\partial \omega} \beta z \end{aligned}$$

with

$$\beta z = \frac{g\mu_B}{\hbar} \frac{dB}{dx} x, \quad (5.12)$$

with  $\mu_B$  the magnetic moment of the transition. The first term in eq.(5.11) is responsible for the damping of the atoms velocity, and the second term provides the spatial confinement.

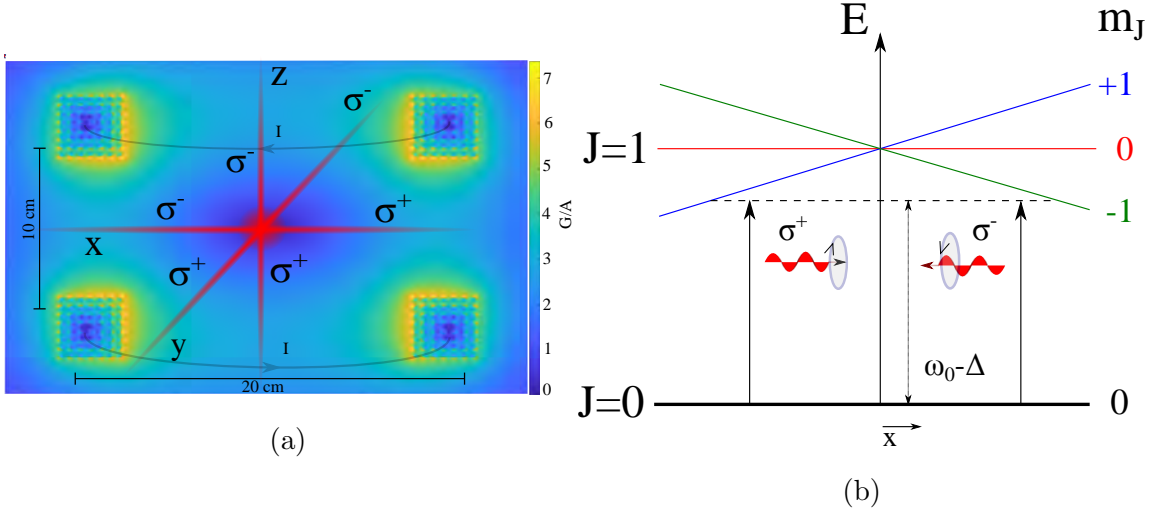


Figure 5.7: a) The MOT coils in an anti-Helmholtz configuration in order to create a linear gradient of magnetic field in the  $x, y, z$  directions to induce a Zeemann shift in the atomic energy levels. b) Principle of the MOT, an atom in the ground state  $\mathbf{J}=\mathbf{0}$  moving to  $-x$  direction absorbs a  $\sigma^+$  photon red-detuned of a value  $\Delta$ . In the same way an atom moving to the  $+x$  direction absorbs a  $\sigma^-$  photon. Therefore the atoms are pushed toward the center of the magnetic field.

**Laser setup.** In Fig. 5.8, we present the different atomic transitions that we need to address for the experiment. The exact layout of the lasers on the optical table can be found in appendix C. The frequency of a laser beam can be adjusted using an acousto-optical modulator (AOM) [70], the light is diffracted through the AOM and we use the first order of diffraction as the output. The amount of light and the frequency shift going through the first order is controlled by a RF signal.

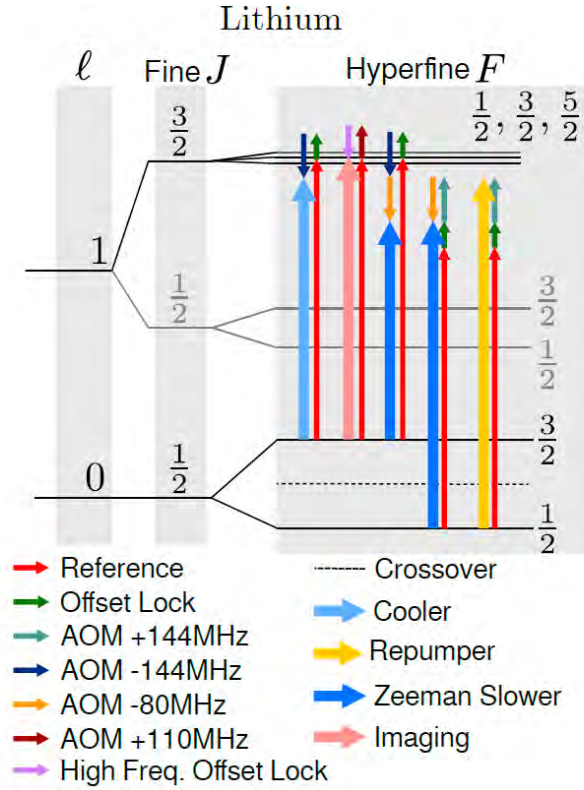


Figure 5.8: Frequencies used in the experiment. Thin arrows add up to obtain the frequencies represented by the thick ones. From [63].

In order to address the transitions shown in Fig. 5.8, we use 4 different lasers. Below we give:

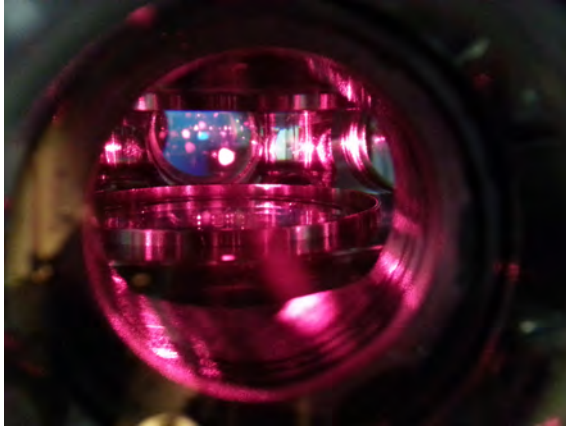
1. **Reference:** Homebuilt diode laser used for the saturation spectroscopy to lock the frequencies of the other lasers. Total output power: 15mW.
2. **Imaging:** Homebuilt diode laser to perform absorption imaging. Total output power: 15mW
3. **Toptica TA pro:** Seed light for the homebuilt TA, and re-pumping light for the MOT and Zeeman slower. Total output power: 350mW.
4. **Homebuilt TA:** Cooling light for the MOT and Zeeman slower. Total output

power: 300mW.

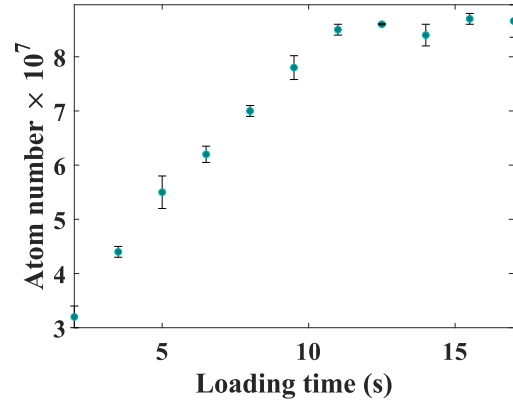
All light is fibre coupled, the output powers that we achieve on the experiment are given in the table below.

Laser	Detuning (MHz)	Output Power (mW)
MOT cooler	-40	20
MOT repumper	-40	18
Zeemann Slower Cooler	-120	12
Zeemann Slower repumper	-120	12

Table 5.1: Optimal values for the MOT light.



(a)



(b)

Figure 5.9: a) Photograph of the  ${}^6\text{Li}$  MOT, containing  $\approx 8 \times 10^7$  atoms. b) Atom number against loading time, measurement done by TOF absorption imaging after 0.2ms of fall time, repeated three times.

### 5.3.2 Compression stage

The lowest temperature achievable in the magneto-optical trap is reached when the detuning of the cooling laser  $\delta = -\Gamma/2$  (see section 5.3.3). The compression stage therefore consists in changing the detuning from  $\delta_{\text{initial}} = -40\text{MHz}$  to  $\delta_{\text{final}} = \Gamma/2$  (2.9MHz) within 11ms, while decreasing the power of the the cooler and repumper light (see Fig. 5.5). During that compression phase, the temperature drops from  $2000\mu\text{K}$  to  $600\mu\text{K}$ . We measure the number of atoms in the compressed MOT scanning the detuning of the cooling laser (see Fig. 5.10) to maximise the phase space density (PSD), and the maximum number of atoms correspond the optimum value of the detuning to reach the lowest temperature temperature  $T=600\mu\text{K}$ .

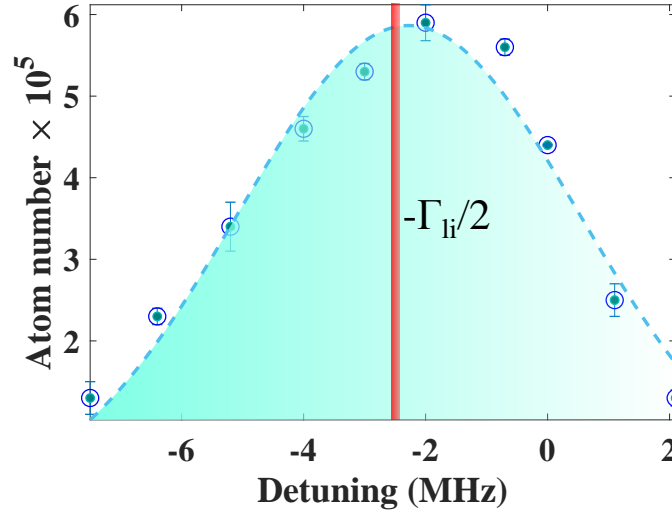


Figure 5.10: Atom numbers against detuning of the cooling/repumping light. The sequence is described above in Fig. 5.5. The measurements are done by TOF absorption imaging (see section 5.5.2) after 0.1ms of fall time, repeated 3 times.

### 5.3.3 Cooling limits

In this section, we discuss the achievable temperature limit of the MOT cooling. The radiation force is a time average force resulting from many absorption-emission events. When an atoms is slow enough, absorption from both sides (1D case) are



equally probable. Moreover, when an atom absorbs or emits a photon, heating occurs due to the photon recoil. Therefore, for each absorption-emission process, the kinetic energy of the atoms increases by  $E_r = 2\hbar k/2m$ . We know that the rate of absorption-emission process is  $R_{sc} = \Gamma\rho_{ee}$ . Then, the rate at which an atom is heated in a 1D MOT is :

$$\frac{dE_{\text{heat}}}{dt} = (2R_{sc})(2E_r). \quad (5.13)$$

In the same way, the cooling rate can be defined using eq.(5.8) :

$$\frac{dE_{\text{cool}}}{dt} = -\gamma v^2. \quad (5.14)$$

Now, we can work out the steady state of such a cooling/heating system:

$$\frac{dE_{\text{total}}}{dt} = \frac{dE_{\text{cool}}}{dt} + \frac{dE_{\text{heat}}}{dt} = 0, \quad (5.15)$$

from this equation, we extract **the equilibrium velocity** :

$$v_{\text{eq}}^2 = \frac{4E_r R_{sc}}{\gamma}. \quad (5.16)$$

Using eq.(5.9), the equilibrium temperature is :

$$k_B T = m v_{\text{eq}}^2 = \frac{\hbar\Gamma}{4} \left( \frac{2|\delta|}{\Gamma} + \frac{\Gamma}{2\delta} \right). \quad (5.17)$$

This limit temperature is called **the Doppler temperature**, reached for  $\delta = -\Gamma/2$  and defined by:

$$T_D = \frac{\hbar\Gamma}{2k_B}. \quad (5.18)$$

For lithium, this temperature is  $141\mu\text{K}$ . However, the temperature typically achieved in labs are much higher, in our case the temperature achieved is  $\approx 600\mu\text{K}$ , the reason is the overlap of the excited  $^2P_{3/2}$  hyperfine levels (see Fig. 4.4) that results in a broader effective linewidth for the cooling transition, therefore higher Doppler temperature. The proximity of the different  $^2P_{3/2}$  hyperfine levels also forbid the use of sub-Doppler cooling method [51]. Currently a grey molasses [71] is being implemented, to do so a laser providing cooling and repumping light is begin constructed to reach lower temperatures during the MOT stage.

## 5.4 Evaporative cooling in the main chamber

After loading and compressing the atoms in the MOT, the temperature of the atoms is about  $600\mu\text{K}$  and the atoms are in an equal mixture of  $|F = 1/2, m_F = -1/2\rangle$  and  $|F = 1/2, m_F = +1/2\rangle$  states to allow collisions, due to the fermionic nature of the  ${}^6\text{Li}$  atoms, only atoms in different states can collide, therefore thermalise. The atoms are then transferred to the optical dipole trap created by a 100W IPG laser. The beam is focused down to a waist of  $80\mu\text{m}$  in the center of the main chamber and reflected back to the main chamber (yellow line on Fig. 5.17) to form a crossed beam trap (see Fig. 5.11). At the same time, to enhance the thermalisation of the atomic ensemble the Feshbach coils are switched on, in order to increase the inter-atoms interactions in the trap. Then, after a plain evaporation time (i.e. a hold time where the trap depth is kept constant)  $\approx 1200\text{ms}$ , the power of the dipole trap is decreased to start the evaporative cooling sequence [72] to reach temperature  $\approx 100\text{nK}$ . The sequence of the evaporation is depicted in Fig. 5.12.

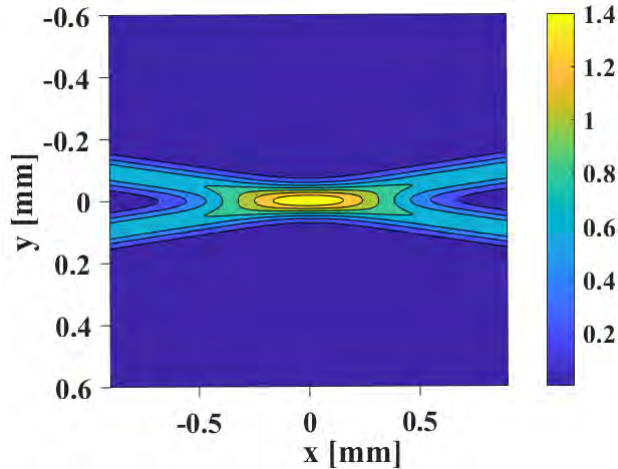


Figure 5.11: Projection of the potential created by the dipole trap seen by the atoms on the (x,y) plan. The scale is in mK.

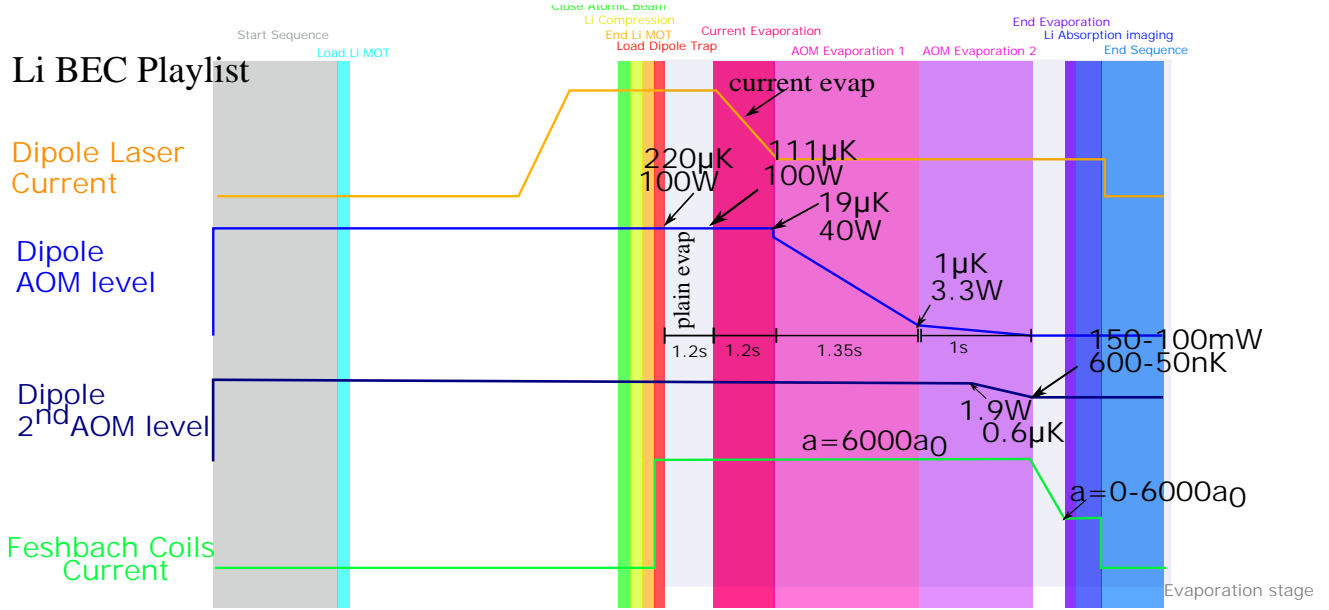


Figure 5.12: Dipole trap sequence. After the compression of the MOT, the cooler and repumper laser are turned off, and the atoms are transferred into the dipole trap. After a period of plain evaporation of 1.2s, we perform forced evaporation. The first stage of the forced evaporation is the current evaporation where we decrease the current going into the dipole laser to lower the power of the dipole trap. Then, we decrease the power using the first AOM driver until we reach temperature  $< 1\mu\text{K}$ , then a second AOM driver is used to decrease the temperature to reach 600 – 50nK, where atoms are converted to molecules and the PSD  $D > 1$ , so we observe a mBEC. The inter-atomic interactions are set to a high value along the sequence  $\approx 6000a_0$  to maximize the thermalisation. Once the atoms reach the desired temperature, we take a picture using an absorption imaging method, and the Feshbach coils field is set to the final value in a range of [700 – 800G]. The temperatures above  $T_c$  at the different stages of the evaporation are taken using time of flight imaging (see section 5.5.2) with 5 repetitions, and below  $T_c$  we use an in situ imaging method. We also display the corresponding dipole trap laser power measured with powermeter  $+/- 0.1\text{mW}$ .

### 5.4.1 Evaporative cooling

The atoms are confined in an optical dipole trap (see section 5.4.2), with a depth of  $U_0$ . Therefore, to leave the trap, an atom needs an energy of :

$$U_{\text{atom}} > U_0 + \epsilon k_B T, \quad (5.19)$$

assuming that the zero energy is at the bottom of the trap. The coefficient  $0 < \epsilon < 1$  represents the fraction of **thermal energy** carried by the atom. The probability for an atom to leave the trap is high, if it is situated in the tail of the Boltzmann distribution. Evaporation cooling is equivalent to cutting off the tail of the Boltzmann distribution, then due to the elastic collisions, the atoms thermalize to a lower mean temperature (see Fig. 5.13).

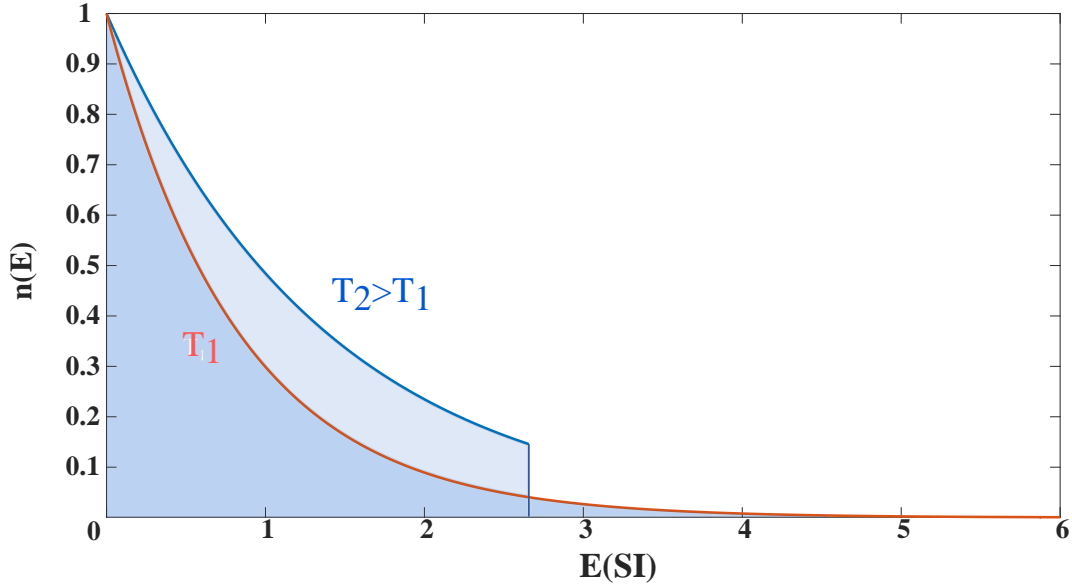


Figure 5.13: Population density depending on the energy of atoms for the Maxwell-Boltzmann (MB) distribution. The principle of evaporative cooling is to remove the higher energy atoms, i.e. cutting off the tail of the MB distribution (blue curve), then the atoms thermalise due to the elastic collisions to a lower temperature (red curve).

Cutting off the tail is done by removing atoms from the trap, and the loss rate

of a trap is defined by [73]:

$$\dot{N} = -N\gamma_{\text{el}}\eta e^{-\eta}, \quad (5.20)$$

where  $N$  is the total atom number and  $\eta = U_0/k_B T$  the truncation parameter. Now, we define  $\gamma_{\text{el}}$  the elastic collisions rate:

$$\gamma_{\text{el}} = n_0 \sigma \bar{v} \quad (5.21)$$

where  $n_0$  is the atom density,  $\sigma$  the atom-atom scattering cross section and  $\bar{v}$  the mean relative velocity of the atoms in the trap. To optimize the evaporation rate in order to get a more efficient thermalisation, we can adjust the cross section  $\sigma$  discussed in chapter 2. The rate of change of total energy of the gas is :

$$\dot{E} = E(U_0 + \epsilon k_B T), \quad (5.22)$$

the fraction of the energy carried out can be found, using kinetic theory, to be  $\epsilon = \frac{\eta-5}{\eta-4}$  for a harmonic trap with energy dependant cross section [72].

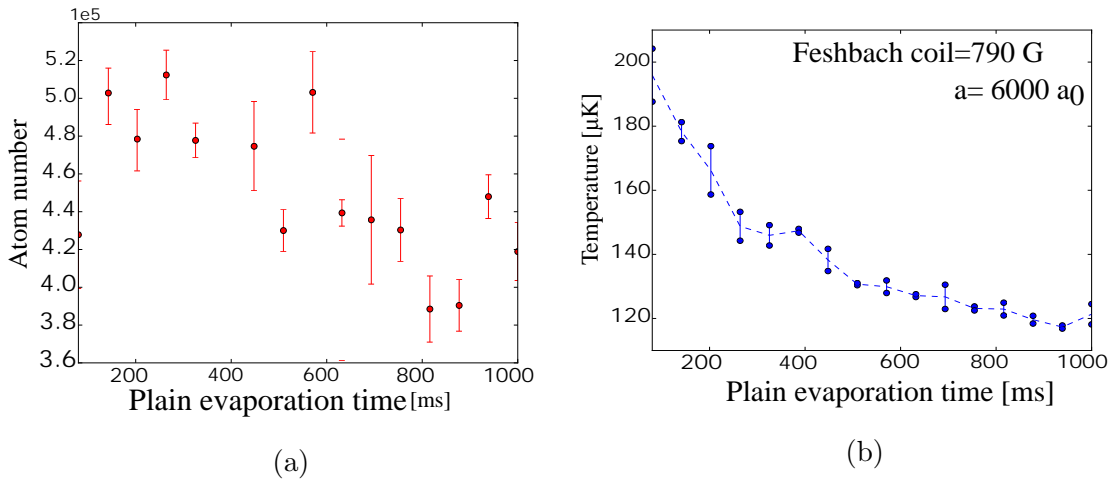


Figure 5.14: a) We scan the plain evaporation time and measure the atom number with an interaction strength of  $6000a_0$ . b) We measure the temperature at different plain evaporation times with an interaction strength of  $6000a_0$ .

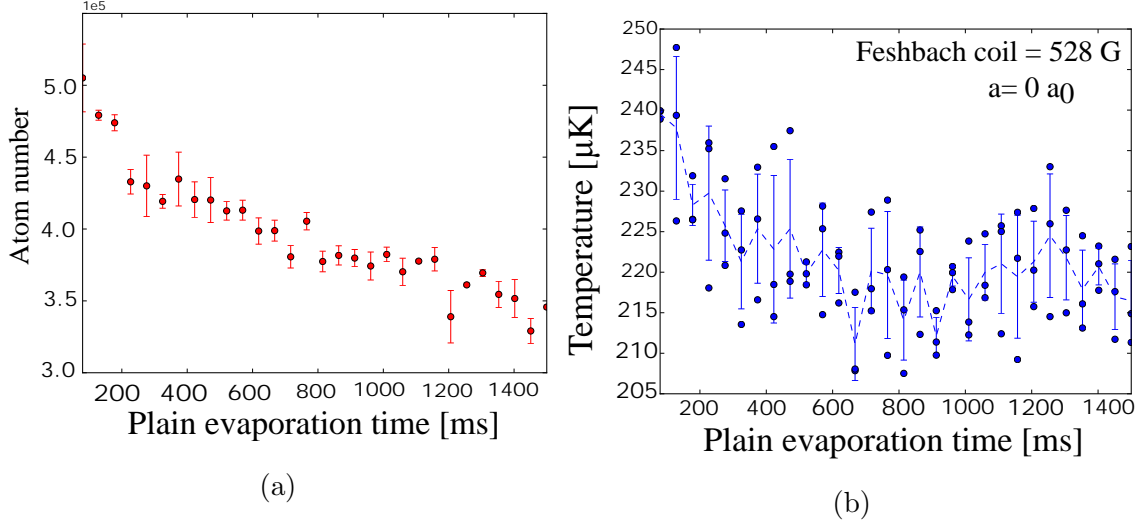


Figure 5.15: a) We scan the plain evaporation time and measure the atom number with no interaction strength. b) We measure the temperature at different plain evaporation times with no interaction strength.

In Fig. 5.14 and Fig. 5.15, we see the influence of the atomic scattering length on the temperature. In the case of a highly interacting cloud, the atoms are cooling down, however if the interactions are removed the atoms temperature stays (mainly) constant. Now, following the idea developed in [74], we can find the optimal truncation parameter. A formula for the ratio of the elastic collision rate vs. the background collisions  $\kappa_c = \gamma_{el}/\gamma_{bck}$  is given by:

$$\kappa_c = \frac{q}{(n-1)\Gamma(n+2, \eta)/\Gamma(n+2) - n\Gamma(n+1, \eta)/\Gamma(n+1)}, \quad (5.23)$$

where  $\Gamma(n, \eta)$  and  $\Gamma(n)$  are the incomplete and complete gamma functions. According to [55, 75],  $q=5$ ,  $n=2$  for a harmonic trap, (see Fig. 5.16). And the optimum parameter is found to be :

$$\eta_0 = \frac{n}{n-1} \frac{\Gamma(n+2)}{\Gamma(n+1)} = 6 \quad (5.24)$$

We summarize the temperature during the evaporation process in the following figure:

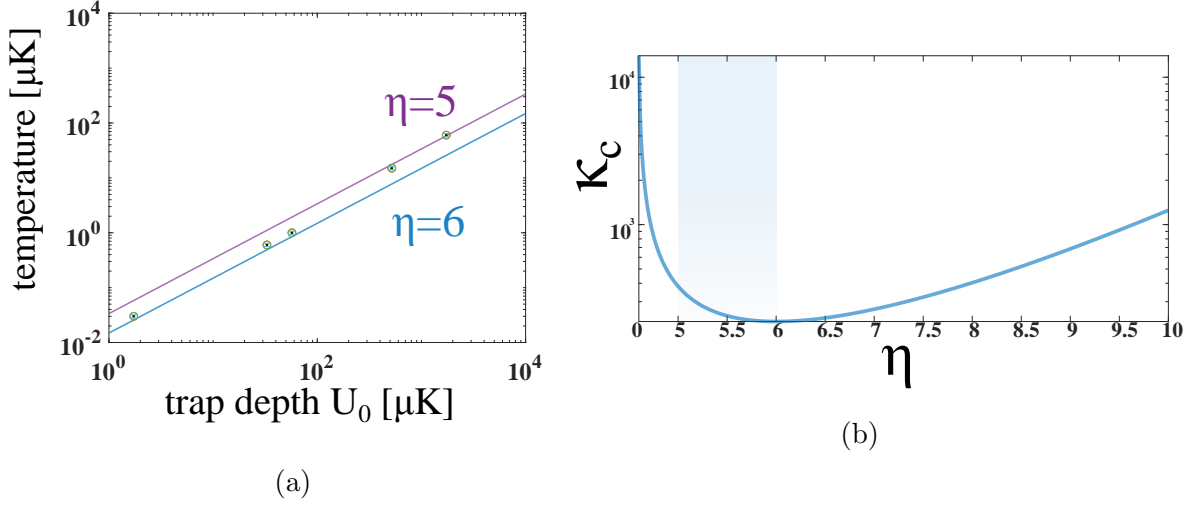


Figure 5.16: a) Log-log plot of the measured temperature of the atoms in  $\mu\text{K}$  against the depth of the dipole trap in  $\mu\text{K}$ . The value of the trap depth in  $\mu\text{K}$  is calculated through the simulation of the dipole trap (see section 5.4.2), giving us the relation between the power of the dipole trap beam in Watt and the "temperature" of the trap in Kelvin  $U = cP$ , with  $c = 17.3\mu\text{KW}^{-1}$ . b) Plot of the collision parameter  $\kappa_c$  against the truncation parameter  $\eta$ . The optimum parameter for our experiment found using eq.(5.24) gives us a value of 6, however we are experimentally in the blue region on the figure in the range of  $\eta = [5 - 6]$ . This is because the theory neglects the effect of the interaction between atoms that are increased in our experiment using the Feshbach resonance.

### 5.4.2 Dipole trap

In this section, we discuss the effect of the dipole trap on the atoms, we show a simulation of the potential seen by the atoms in the main chamber (see Fig. 5.19) when the IPG 100W laser (see Fig. 5.17) is turned on.

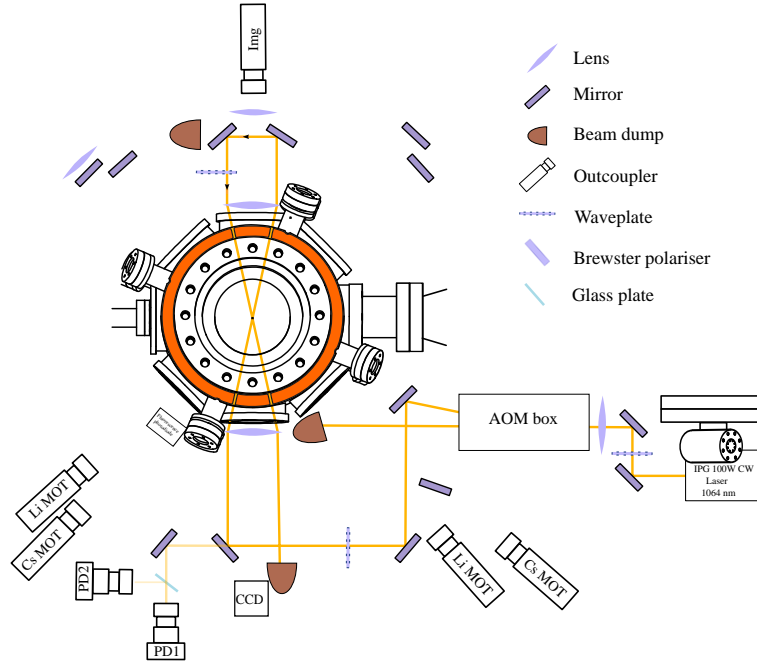


Figure 5.17: Top view of the main chamber, the yellow path represents the IPG laser. The angle formed by the laser is 13 degrees, the waist at the focus point is  $80\mu\text{m}$ , and the Rayleigh length  $z_R = 23\text{mm}$ . During the dipole trap sequence, the Feshbach coils are also switched on, in orange in the figure. PD1 and PD2 are the photodiodes for the laser stabilization, discussed in section 5.4.4.

To do so, we use eq.(4.33) and  $\Gamma = (\omega_0)^3/3\pi\epsilon_0\hbar c^3|\langle e|\mathbf{p}|g\rangle|^2$ , to obtain the potential experienced by the atoms :

$$V_{\text{dip}} = -\frac{\pi c^2 \Gamma}{2\omega^3} \left( \frac{1}{\Delta_1} + \frac{2}{\Delta_2} \right) I(r) \quad (5.25)$$

Where  $\Delta_{1/2}$  are the detuning values of the dipole trap beam frequency of the spectral line  $D_{1/2}$ . The intensity of the laser beam  $I(r, z)$  is described in the appendix D, given by :

$$I(r, z) = \frac{2P}{\pi w^2(z)} e^{-(2r^2/w^2(z))}, \quad (5.26)$$

where  $w$  is waist of the laser along the propagation axis  $z$ , and  $P$  the power (W) of



the laser. Then we combine eqs 5.25 and 5.26 to obtain:

$$V(r, z) = -\frac{\pi c^2 \Gamma P}{\omega^3 \pi w^2(z)} \left( \frac{1}{\Delta_1} + \frac{2}{\Delta_2} \right) e^{-(2r^2/w^2(z))} \quad (5.27)$$

We use eq.(5.27) to simulate the crossed beam dipole trap. The angle between the two beams is  $13.2^\circ$  determined from a measurement using absorption imaging pictures (see Fig. 5.18). Moreover the number of atoms determined by TOF is approximately  $2 \cdot 10^6$ .

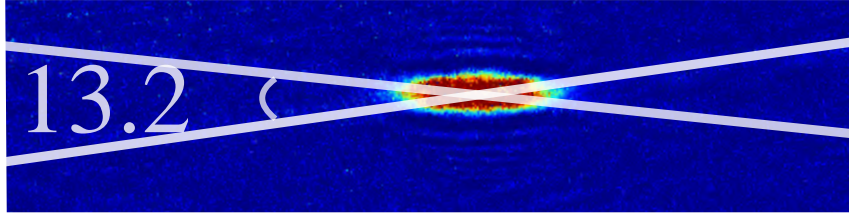


Figure 5.18: Absorption image of the atoms in the dipole trap, the tails of the dipole trap allow us to calculate the angle of the crossed beam.

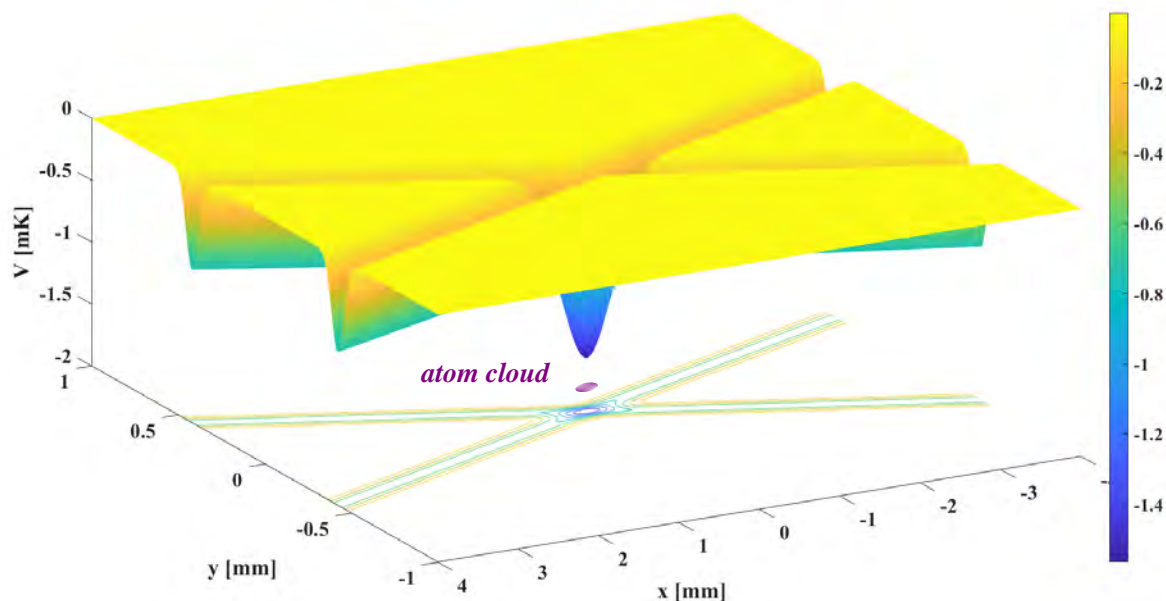


Figure 5.19: Simulation of the dipole potential using the parameters of the IPG laser given in Fig. 5.17 and eqs. (5.25,5.26). The current simulation is done for a IPG laser power  $P=100\text{W}$ .

### 5.4.3 Feshbach Coils

The coils described in this section are used to control the interactions between atoms using Feshbach resonances. This coils can produced a wide range of fields to be able to go over the different resonances (see Fig. 2.4). This coils are arranged in a way that they produce a homogeneous field at the position of the atoms (see Fig. 5.20). A field of 1400G can be reached when passing a current of 400A through them. A stationary temperature of 70°C is reached using a water cooling system.

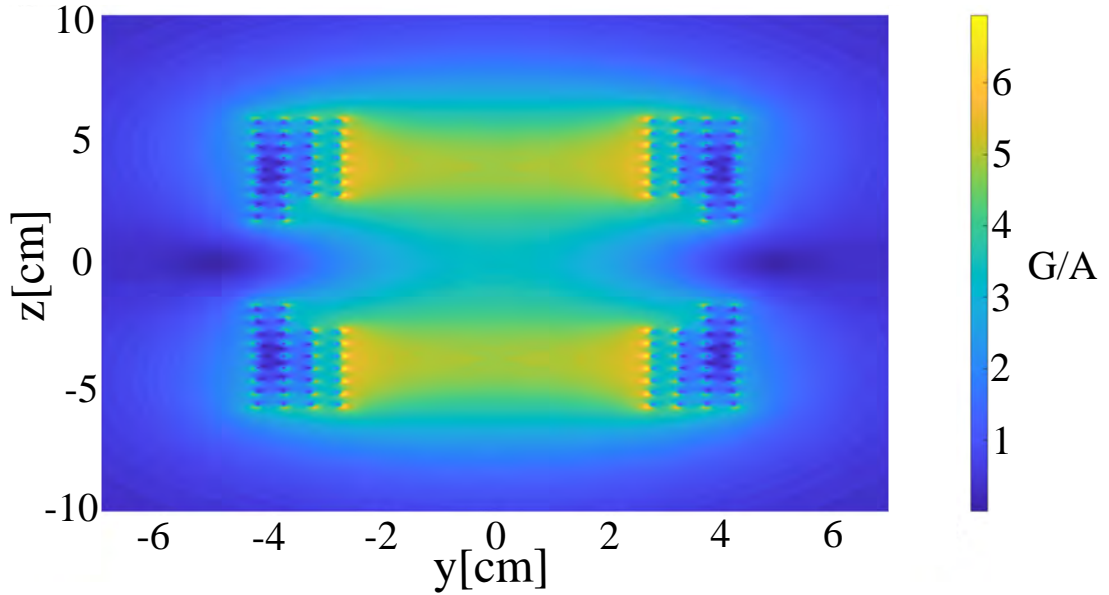


Figure 5.20: Simulation of the magnetic field generated by the Feshbach coils, the coils are set in a Helmholtz configuration in order to create a flat magnetic field in the center of the chamber.

However, the magnetic field produced is not perfectly homogeneous. The residual curvature of the field results in a magnetic potential. The potential is **trapping in the radial direction** Fig. 5.22 and **anti-trapping in the vertical direction** Fig. 5.21 for the atoms in the  $m_F = +1/2$  ground state. When the power of the dipole trap is sufficiently high, the influence of the magnetic trapping/anti-trapping field can be neglected, but when the atoms are in the last stage of evaporation cooling, the magnetic field needs to be taken in account for the correct calculation of the trapping frequencies.

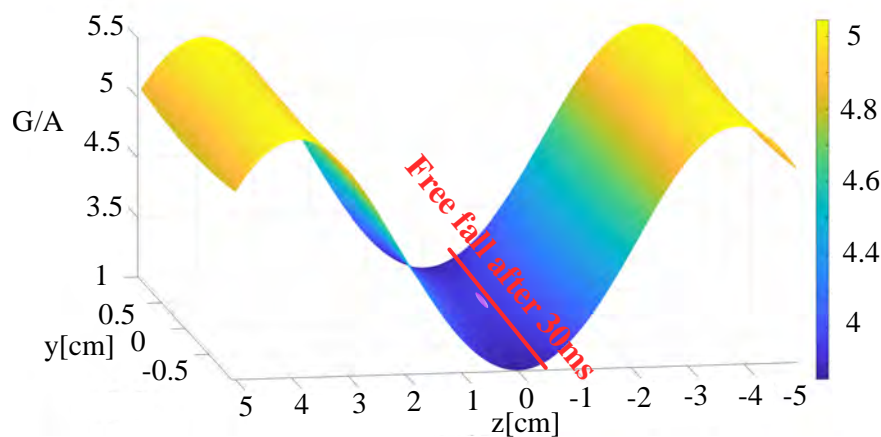


Figure 5.21: Simulation of the magnetic field generated along the vertical axis. This will add an additional trapping/anti-trapping force depending on the internal state of the atoms  $m_F = -1/2$  or  $m_F = +1/2$ .

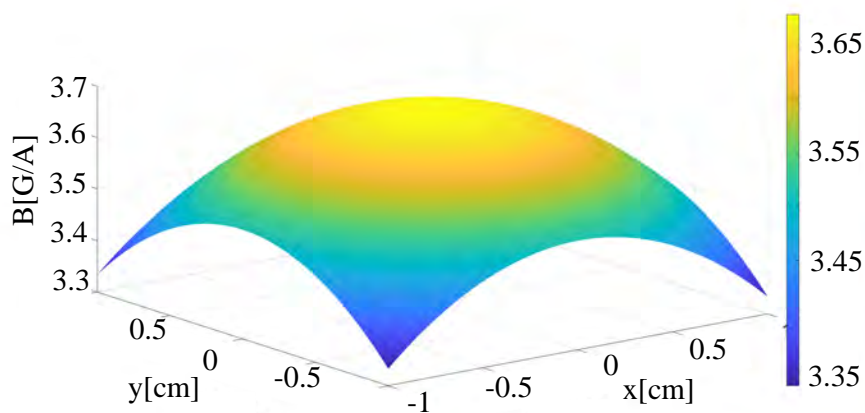


Figure 5.22: Simulation of the magnetic field generated in the horizontal plan. This will add an additional trapping/anti-trapping force depending on the internal state of the atoms  $m_F = -1/2$  or  $m_F = +1/2$ .

The current through these coils can be turned off in  $\approx 1\text{ms}$  using FET-based switch. However, the change of magnetic field create eddy currents in the steel chamber, that can last for 10ms (Fig. 5.23).

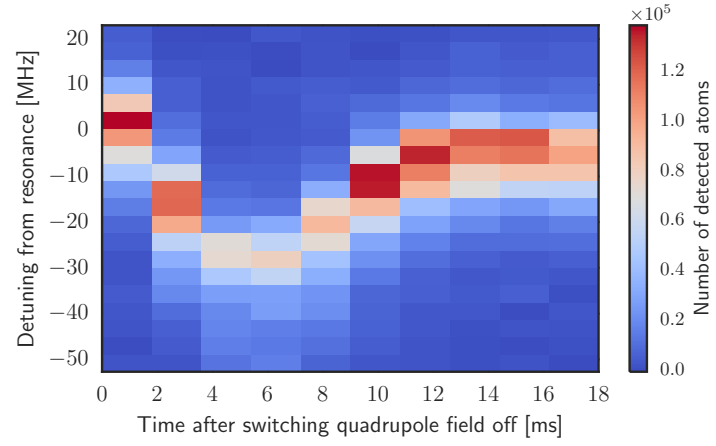


Figure 5.23: Shift of the resonant imaging frequency due to eddy currents after switching off the magnetic coils, from [63].

#### 5.4.4 Stabilization of the dipole trap

In order to reduce heating in the dipole trap due to power fluctuation, the intensity of the light is dynamically controlled by a feedback loop. The stabilization system is described in Fig. 5.24.

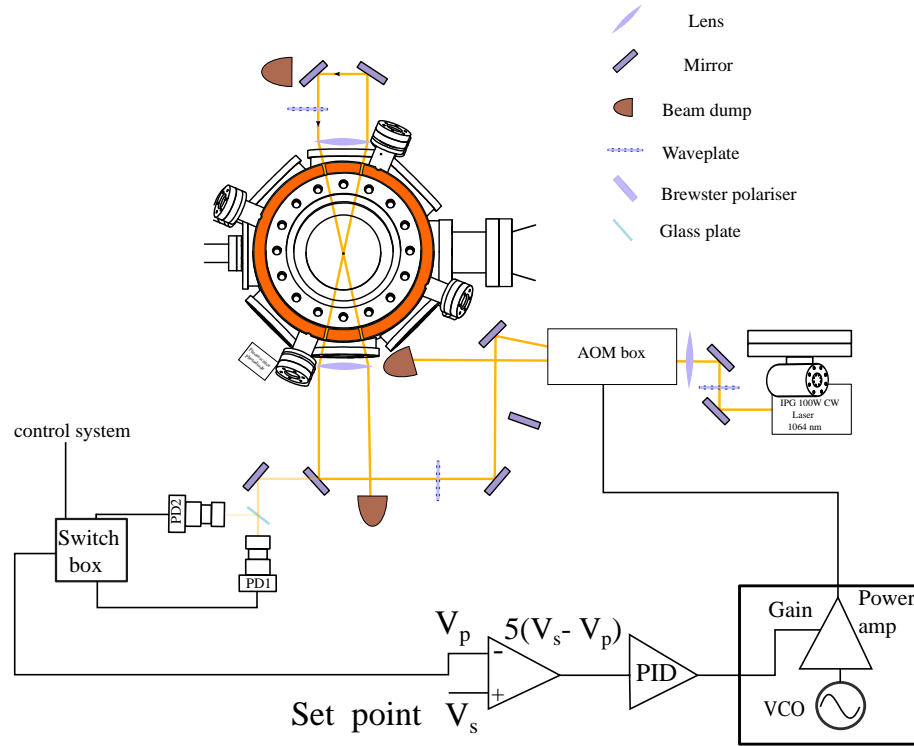


Figure 5.24: Power stabilization scheme for the regulation of the optical dipole trap.

The output light of the IPG laser passes through an AOM, through the first diffraction order. The amount of light going in the first order is controlled by a RF signal. Then, a small amount of light is diverted toward two photodiodes to feed the feedback loop. The intensity of light going into the photodiode is set to be just under the saturation level of the photodiode to get the best signal to noise ratio (SNR), then the voltage of the photodiode  $V_p$  is compared to a set point  $V_s$  using a differential amplifier to give  $5(V_s - V_p)$ . The reason we use two photodiodes is that the range of power for the evaporative cooling goes from 100W to 50mW. When we reach 50mW, if we use only one photodiode, the intensity of light going to the

photodiode is very small and the feedback loop does not work optimally because of a bad SNR. The first one is therefore, used for the high power evaporation part, and the other one for the low evaporation power. We use a switch box controlled by 5V signal from the control system to change from one photodiode to the other one during the evaporation. The  $5(V_s - V_p)$  signal is used as an error signal for the PID controller. The output of the PID controller is then sent back to the AOM driver and the RF signal is to control the intensity of light going into the first order of diffraction of the AOM. The second AOM driver is used for the low power control and the calibration is shown in Fig. 5.25.

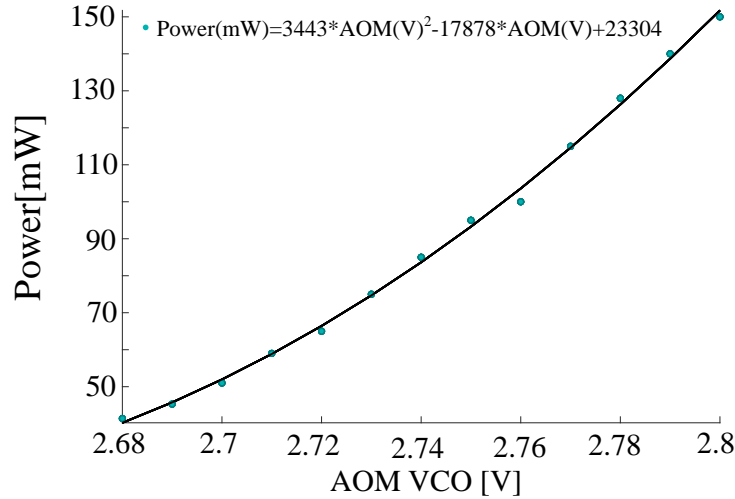


Figure 5.25: Output power of the dipole trap against the control voltage sent the second AOM controller.

In Fig. 5.26, we make sure that the dipole trap is functioning correctly by measurement the number of atoms over a large time range here 32s. Then, we can fit with an exponential to extract the lifetime of the dipole trap (see Fig. 5.26). In the case of  $P = 1.9W$  where the phase space density  $D \approx 1$  (close to the BEC transition), the lifetime is  $\approx 16s$ , which is good because it is bigger than the time of the evaporation sequence  $\approx 5s$ .

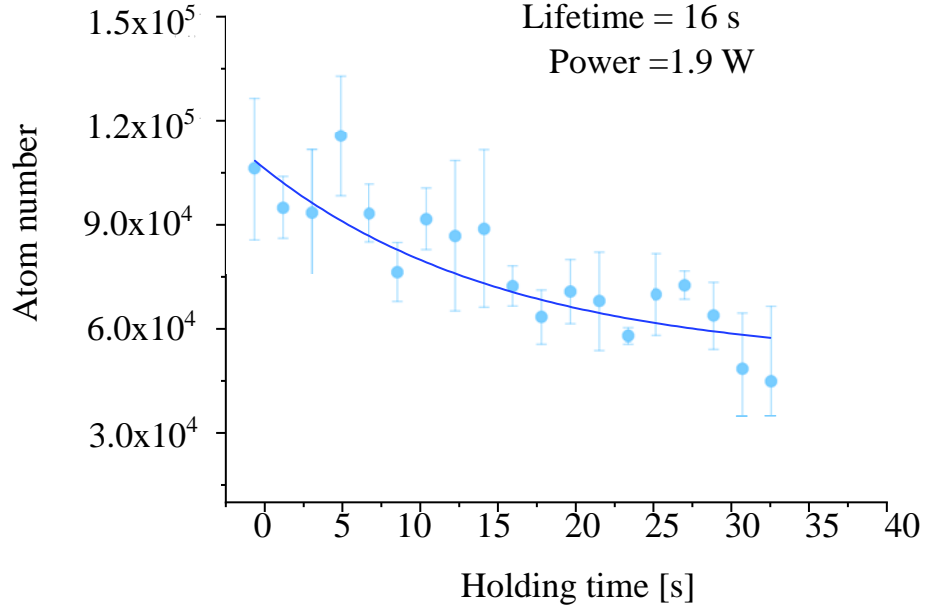


Figure 5.26: We measure the number atoms over time to get access to the lifetime of the dipole trap, in this case at  $P=1.9\text{W}$ .

### 5.4.5 Trapping frequencies

In this section, we describe the method use for the measurement of the trapping frequencies, which are fundamental parameters for the calculation of quantities such as **temperature, chemical potential, condensate fractions**. We first discuss the experimental methods. Using these results, the simulation of the dipole trap potential (see section 5.4.2) and the magnetic fields potential of the Feshbah coils (see section 5.4.3), we obtain a continuous function of the trapping frequencies (radial and longitudinal) depending on the power of the dipole trap. The experimental and theoretical plots are represented in Fig. 5.30 and we find a good agreement between them.



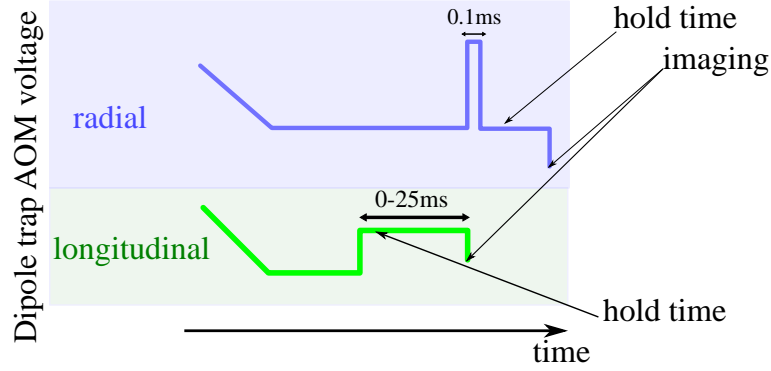


Figure 5.27: Representation of the two methods to measure the radial and the longitudinal frequencies.

Trapping frequencies have been measured in two different ways (see Fig. 5.27), for the radial trapping frequencies the most convenient method was to measure the frequency of the breathing mode. For this method the power of the dipole trap is decreased to the desired value for the trapping frequency measurement then, suddenly increased to a level 20x higher than the initial power, then the size of the cloud oscillate at twice the frequency of the trap. Experimentally, we take pictures at different times after the intensity peak. The other method, consist in measuring the centre of mass oscillations, and gives good results for the longitudinal trapping frequencies. Here the power of the dipole trap is decreased to a value below the power we want to measure the frequency, then the power is risen again to value we want to measure the frequency, and we scan the time that the power is risen and pictures are taken at these different times.

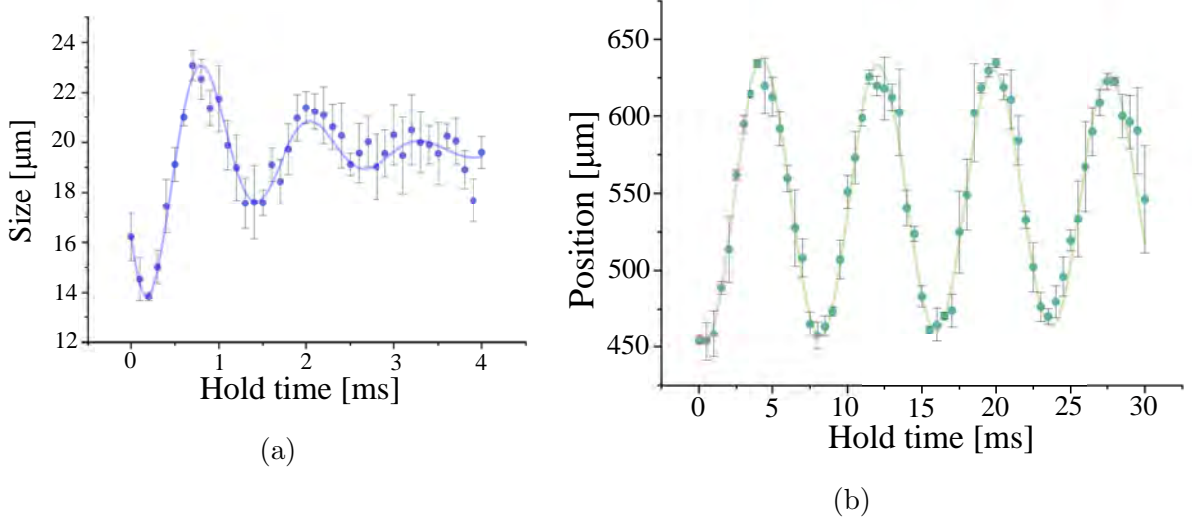


Figure 5.28: Experimental results of the trapping frequency measurement, left hand side is the radial frequency fitted with a damped sine function, the size of the cloud is oscillating, so-called breathing mode. On the left hand side, the longitudinal trapping frequency, here the position of the cloud is oscillating, also fitted with a damped sinus function.

Now, using the simulations of the Feshbach coil shown in section 5.4.3 and section 5.4.2, we obtain the total trapping potential map in the main chamber (see Fig. 5.29). Therefore, assuming the trap to be harmonic  $V(r, z) = 1/2m\omega_r^2r^2 + 1/2m\omega_x^2x^2$ , the simulated potential is fitted with a parabola  $f(x) = a.x^2$  in the respective direction, then the theoretical trapping frequency is given by:

$$\omega_i = \sqrt{2a_i/m}. \quad (5.28)$$

The knowledge of the magnetic potential has a fundamental importance for the trapping frequencies used for the in situ fitting method developed in chapter 6. The In situ pictures are taken in the presence of the optical trap potential and Feshbach magnetic coil and therefore need to be characterized accurately.

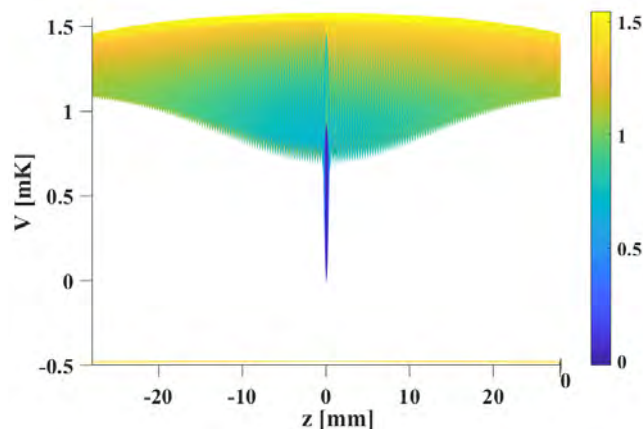


Figure 5.29: Dipole trap potential and Feshbach coil potential combined in order to calculate more accurate theoretical trapping frequencies. We see that the curvature of the magnetic field created by the Feshbach coil is not perfectly flat, therefore the trapping frequencies are modified.

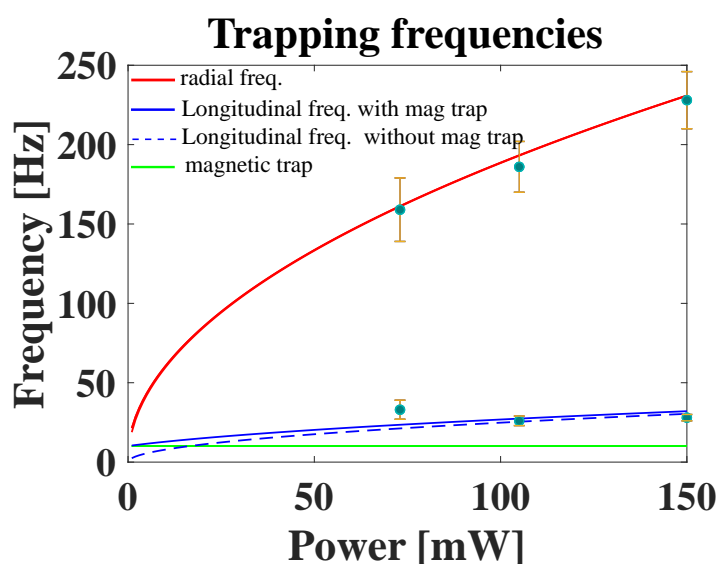


Figure 5.30: Plot of the trapping frequencies (radial, longitudinal) against the dipole trap power and the trap created by the Feshbach coils. Here we plot from 0 to 150mW, the region that we are interested in to achieve condensation. The experimental points are taken using the technique explained above and averaged over 3 measurements.

## 5.5 Imaging

The imaging system is an essential tool to explore the properties of the atomic cloud. In this section, we first discuss the absorption imaging, which is the principal technique used to recover images by shining a resonant light beam on the cloud, then the shade is recorded on a CCD camera and then analysed, allowing us to access the spatial density distribution of the atoms. Next, we describe a method to measure the temperature, the Time of Flight (TOF) method, and discuss its limitations, and why using in situ imaging for low temperature is more appropriate in our experiment. Finally, we use the frequency of the resonant imaging beam to obtain the value of the magnetic field and via the Feshbach resonance the value of the inter-atomic interaction of the atoms.

### 5.5.1 Absorption imaging

A resonant beam with an intensity of  $\approx 1\text{mW}$  is sent on the atom cloud (see Fig. 5.32), and the transmitted signal (depending on the absorption coefficient) is recovered on a CCD camera [9]. Using the definition of the polarizability eq.(4.41), we know the refractive index  $n_{\text{ref}} = \sqrt{1 + n\alpha/2\epsilon_0}$ , where  $n$  the density of atoms, and  $\epsilon_0$  the vacuum permittivity. The absorption coefficient  $a$  can be calculated using [62]:

$$a = 2k_0 \text{Im}\{1 + n\alpha/\epsilon_0\} = \frac{n\hbar\omega_0\Gamma}{2I_{\text{sat}}} \frac{1}{1 + (2\Delta/\Gamma)^2 + I/I_{\text{sat}}} = n\sigma_{\text{scat}} \quad (5.29)$$

with  $\sigma_{\text{scat}}$  the photon-atom cross section given by:

$$\sigma_{\text{scat}} = \frac{\sigma_0}{1 + (2\Delta/\Gamma)^2 + I/I_{\text{sat}}}, \quad (5.30)$$

and  $\sigma_0$  the cross section at  $\Delta = 0$  and  $I \ll I_{\text{sat}}$  is given

$$\sigma_0 = \frac{\hbar\omega_0\Gamma}{2I_{\text{sat}}}. \quad (5.31)$$

From the absorption imaging, we need to extract **spatial density** profile. We use the Lambert-Beer law describing the evolution of the **intensity** of the probe beam

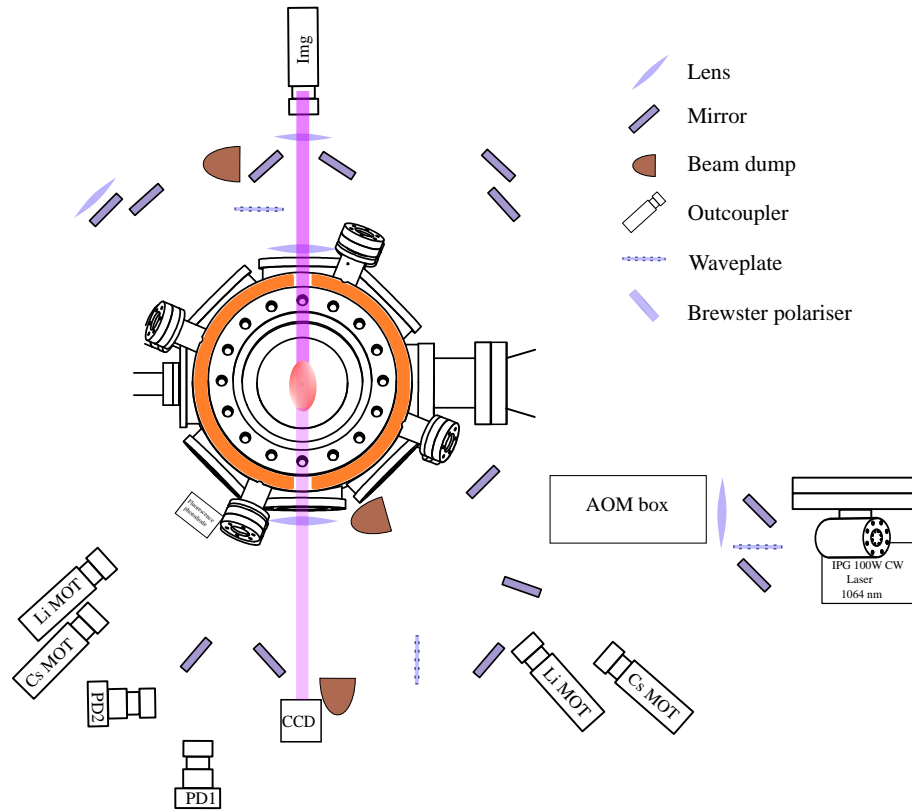


Figure 5.31: Top view of the horizontal imaging system. Light from the imaging outcoupler goes in the chamber, the atom cloud absorbs a part of the light, then a CCD camera recovers the remaining light.

intensity through the medium (the atom cloud) with an absorption  $a$ :

$$\frac{dI}{dz} = -aI, \quad (5.32)$$

then, eq.(5.32) is integrated along the imaging axis. The integration gives us:

$$I_{\text{after the cloud}}(x, y) = I_{\text{before the cloud}}(x, y)e^{-n_z(x, y) \cdot \sigma_{\text{sc}}}, \quad (5.33)$$

with  $n_z(x, y) = \int_{\text{size of the cloud}} n(x, y, z) dz$ , here  $n_z$  is the atomic density in  $z$ -direction that we can extract from eq.(5.33):

$$n_z = -\frac{1}{\sigma_{\text{sc}}} \ln \frac{I_{\text{out}}}{I_{\text{in}}}, \quad (5.34)$$

we also define the optical density:

$$D = n\sigma_0 \frac{1}{1 + \Delta}. \quad (5.35)$$

For the density profiles treated in this thesis  $D \ll 1$ . In contrast, dispersive methods could be also used such as phase contrast imaging [76, 77], however hard to implement in our experiment.

**Experimental realisation and sequence.** In our experiment we have the option to take images along the horizontal and vertical axis (see Fig. 5.32). On the horizontal axis we use an Allied Vision Guppy Pro camera and on the vertical axis an Allied Vision Manta, both setup use imaging telescopes. We summarize in the following figure the experimental set up for the imaging system:

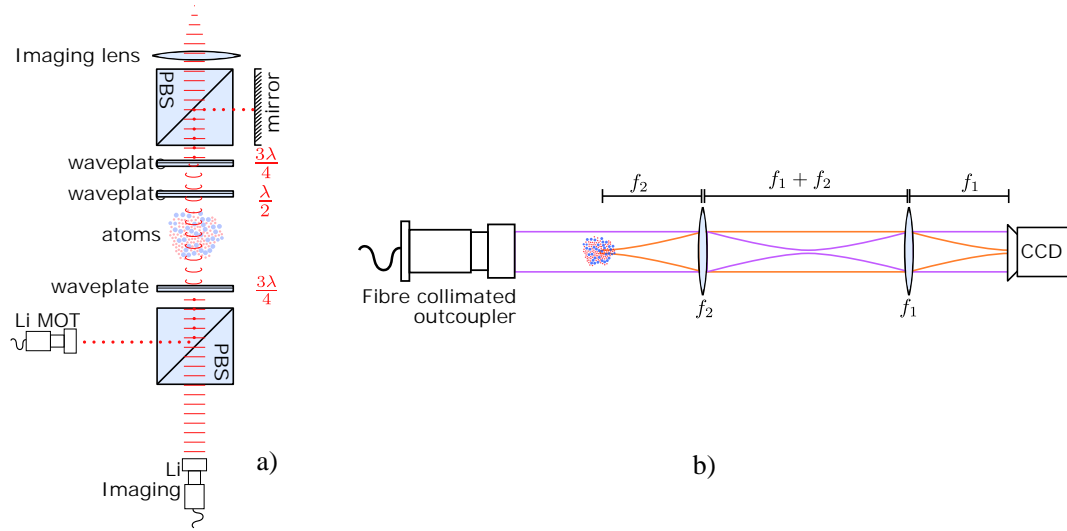


Figure 5.32: a) On the vertical imaging axis the MOT light and the imaging light are overlapped using a polarising beam splitter. b) Telescope scheme used in the case of the vertical and horizontal imaging. For vertical imaging  $f_1 = 250\text{mm}$   $f_2 = 75\text{mm}$ , with a resolution of  $2.5\mu\text{m}$ , for horizontal imaging  $f_1 = 60\text{mm}$   $f_2 = 125\text{mm}$  with a resolution of  $2.0\mu\text{m}$ .

The experimental sequence of the absorption imaging is depicted in Fig. 5.33 where three pictures are taken (see Fig. 5.34) and then reconstructed Fig. 5.35.

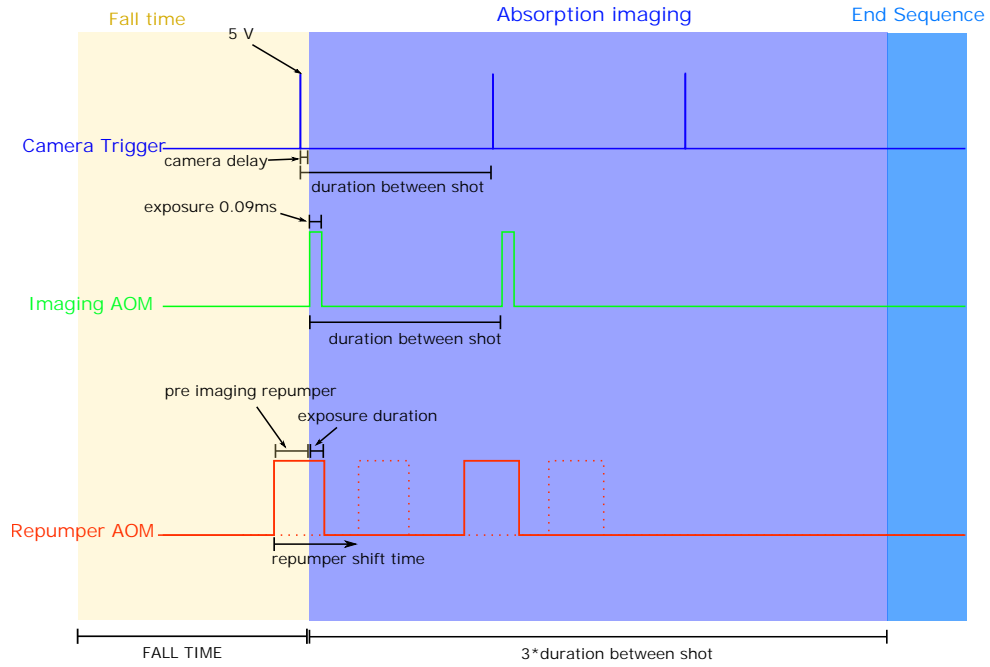


Figure 5.33: Sequence of time of flight imaging. The imaging starts after the fall time. The repumper can be shifted, depending if it is needed during the imaging.

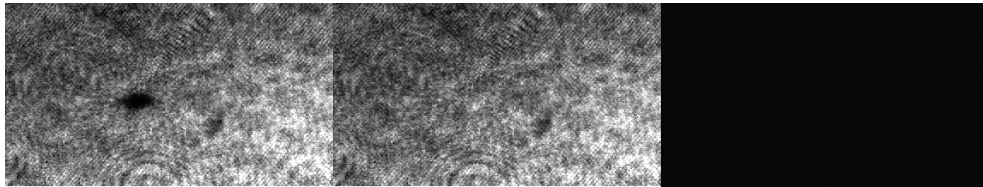


Figure 5.34: During the absorption picture sequence, 3 pictures are taken, the first with light and atoms, the second without atoms and the third one without light.

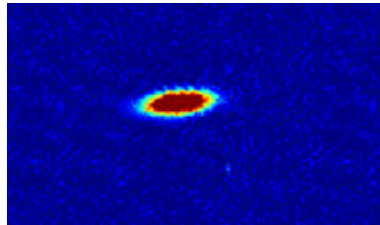


Figure 5.35: Reconstructed images from the raw data Fig. 5.34.



### 5.5.2 TOF

The Time of Flight imaging technique is used to determine the temperature of an atom cloud. It consist in releasing the atoms from the trap by turning off the dipole trap light. Then, the atoms expands freely, we then take several pictures at different time after the release [9, 24]. The absorption imaging is a destructive process, therefore, to take several pictures at different releasing times, the experiment is repeated.

Once the atoms are released, we take picture at different release times (see Fig. 5.36).

**Above  $T_c$ .** The density of the cloud can be treated classically by a Boltzmann distribution:

$$f(\mathbf{r}, \mathbf{p}) \propto e^{-E(\mathbf{r}, \mathbf{p})/k_B T}. \quad (5.36)$$

Where  $f(\mathbf{r}, \mathbf{p})$  is the probability of finding a particle at the position and momentum  $(\mathbf{r}, \mathbf{p})$ . Using the harmonic trap frequency, the energy becomes:

$$E(\mathbf{r}, \mathbf{p}) = \frac{p^2}{2m} + \frac{1}{2}m\omega^2 r^2, \quad (5.37)$$

the normalization of eq.(5.36) using eq.(5.37) gives us :

$$f(\mathbf{r}, \mathbf{p}) = \frac{1}{(2\pi\sigma_r^2)^{3/2}} e^{\frac{-r^2}{2\sigma_r^2}} \frac{1}{(2\pi\sigma_p^2)^{3/2}} e^{\frac{-p^2}{2\sigma_p^2}} \quad (5.38)$$

where  $\sigma_r = k_B T / m\omega^2$  and  $\sigma_p = mk_B T$ . Now, we want to know explore the dynamics of the cloud after a **fall time** of a few milliseconds, we define  $\mathbf{r}' = \mathbf{r} + \frac{\mathbf{p}}{m}t$  that we insert in eq.(5.38), then we integrate over the momentum and we have :

$$f(\mathbf{r}') = \frac{1}{(2\pi\sigma_t^2)^{3/2}} e^{\frac{-r'^2}{2\sigma_t^2}} \quad (5.39)$$

with  $\sigma_t^2 = t^2\sigma_p^2/m + \sigma_r^2$ . We integrate the density profiles of Fig. 5.36 along the longitudinal and radial axis, then the fit of eq.(5.39) gives us  $\sigma_t$ , therefore the temperature can be calculated (see Fig. 5.37).

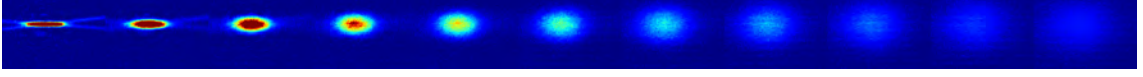


Figure 5.36: Atomic density of the cloud at different fall times. The fall time varies from 0 ms to 0.5 ms.

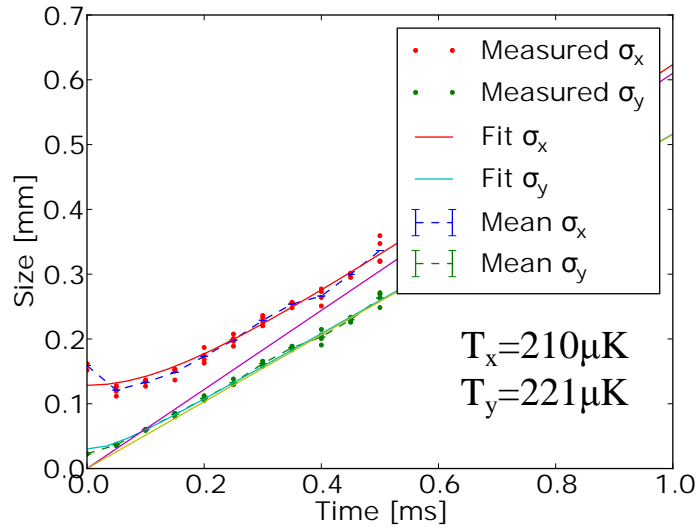


Figure 5.37: Sequence of time of flight imaging. The imaging starts after the fall time.

**Below  $T_c$ .** The density is fit using a bimodal distribution described in details in section 6.2.2 by the ideal gas model. Where the total density is the sum of the condensate density  $n_0$  and the thermal density  $n_{Th}$  integrated to give one dimension densities function and given by:

$$n_0(x) = \max \left[ \frac{15N_0}{R_x} \left( 1 - \frac{x^2}{R_x^2} \right)^2 \right], \quad (5.40)$$

and a Gaussian distribution for the thermal atoms:

$$n_{Th}(x) = \frac{N_{Th}}{\sqrt{2\pi}\sigma_x}, \quad (5.41)$$

where  $N_0$  is the number of condensate atom,  $N_{Th}$  the number of thermal atoms,  $R_x$  the radius of the condensate and  $\sigma_x$  the width of the distribution.

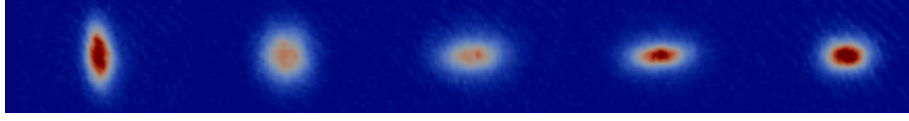


Figure 5.38: The atoms are released at  $T < T_c$ , we observe of inversion the aspect ratio.

This method is suitable to measure classic clouds where  $T > T_c$ , because when the cloud becomes very cold, the expansion of the cloud is also very small and we need to increase the fall time, typically 15 – 25ms. In section 5.4.3, we describe the effect of parasite eddy current that can change the transition frequency. Moreover the influence of the residual Feshbach magnetic field which is difficult to quantify, and in [63], it has been shown that for very low temperature the gas does not undergo a free fall. Finally, during that time the cloud can interact with the background gas and loses informations. Therefore, a most reliable method to obtain the atom cloud density profile is to take in situ image, described in the next section, i.e. the absorption imaging is performed immediately after the switch-off of the dipole trap and the Feshbach coils. However, we are imaging molecules, so the scattering must be chosen so that the binding energy  $E_b = \hbar/2ma^2$  is not too high so they can be dissociate by the imaging light, and we only image one of the two hyperfine state. Therefore, the magnetic field is set between 700G and 800G for just before the imaging process.

### 5.5.3 In situ imaging

In this section, we describe the sequence used for In-situ imaging. In general, this is similar to the TOF method, the difference is the absence of fall time. Moreover, the trigger for the camera and the AOM of the imaging laser is shifted from a small amount due to the delay of the camera and the control system. Even if it is quite small it is important that the cloud does not expand so we have the image of the spatial density in the trapping potential. To get the value of the shift we scan the

shifting time until the cloud is deformed by the imaging light.

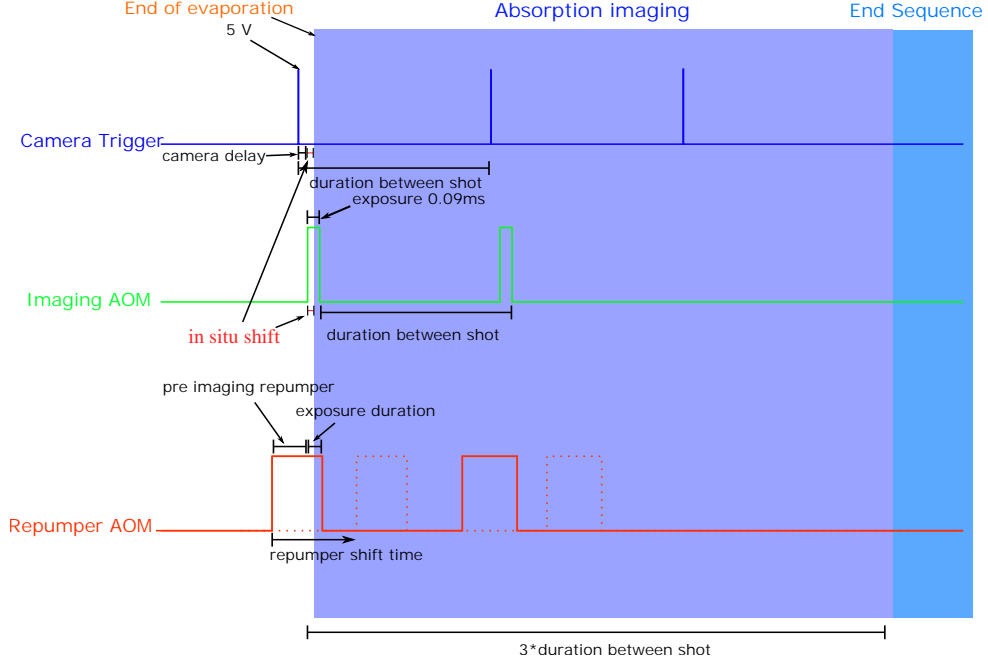


Figure 5.39: Sequence of In situ imaging. Here the imaging starts directly after the evaporation and a period of thermalisation of 100ms, moreover a small delay of  $< 1\text{ms}$  is added to allow for switching time of the dipole trap.

#### 5.5.4 High field imaging and scattering length determination

When atoms are loaded into the dipole trap, they are pumped into a mixture of  $|F = 1/2, m_F = -1/2\rangle$  and  $|F = 1/2, m_F = +1/2\rangle$  hyperfine states, (see section 5.3.2). By tuning the frequency of the imaging laser, it is possible to observe the population of these states Fig. 5.40, and adjust the resonance frequency to maximise the number of atoms. The desired frequency is obtained using an offset lock [78], described in appendix E. It can be tuned over a wide range of frequencies, therefore imaging at different magnetic fields/inter-atomic interactions [450G-900G] is possible. However, to image the MOT we use another locking point, because when the Feshbach coils are off we do not need to scan the imaging over a wide range, so-called **low field**

imaging.

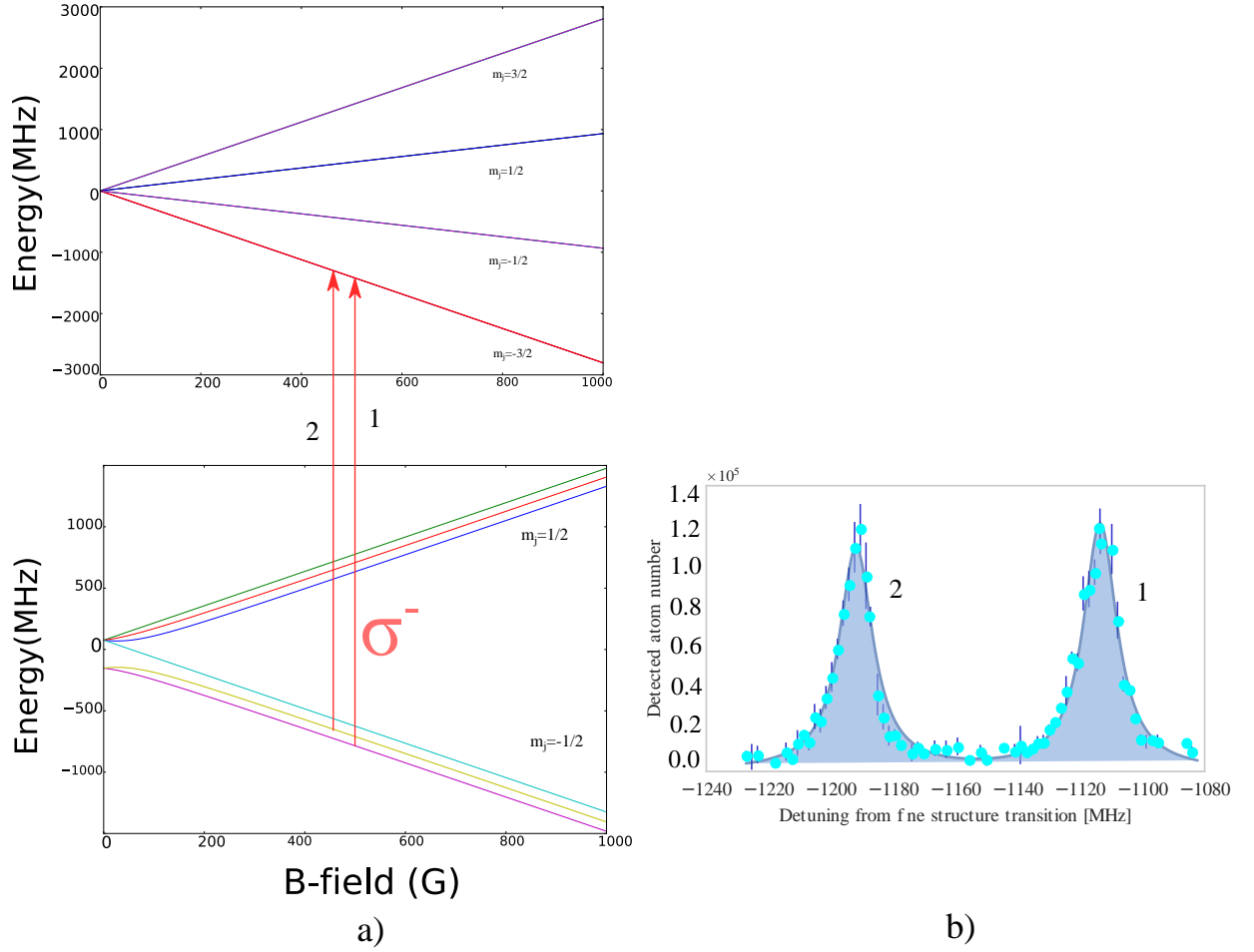


Figure 5.40: a) Transitions used to image atoms in the High field regime. b) Atom number against the imaging frequency showing the two peaks corresponding to the two transition in fig a).

In the **high field imaging** case, once we find the optimal imaging frequency by scanning the imaging frequency and choose the frequency that maximise the atom number, we can directly read off the difference between the reference and imaging laser using a frequency counter placed in the offset lock scheme. We then use this value to find the corresponding magnetic field using Fig. 5.41. The peaks in Fig. 5.40

b) are clearly resolved and the FWHM of each peak is  $\Gamma/2 = 12\text{MHz}$ . Then using Fig. 2.4, we can determine the scattering length of the atoms.

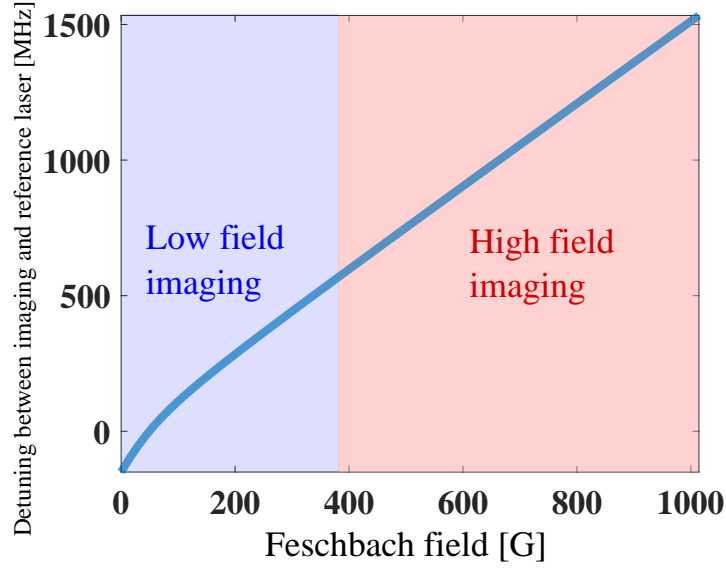


Figure 5.41: The frequency difference between the ground state  $F=1/2$  and the excited state  $m_j = -3/2$  (see Fig. 5.40) against the Feshbach magnetic field.

# Chapter 6

## Study of an interacting ${}^6\text{Li}$ mBEC

In this chapter, we investigate the finite temperature properties of a strongly interacting  ${}^6\text{Li}$  molecular BEC (mBEC) cloud in a harmonic trap to show that the interactions due to the thermal atomic cloud lower the transition temperature by depleting the condensate part, the interactions strength are tuned to investigate this effect for different values of  $a$  (see Fig. 6.1).

By fitting the one dimension spatial density obtained by in situ absorption imaging (see section 5.5.3), we get access to the **temperature** and the **chemical potential** of the atomic cloud. The quality of the fit is given by  $\chi^2$  method [79, 80]. The spatial density is fitted using three different models (see Fig. 6.1), **Ideal Gas(IG)** model [24], **Semi-Ideal(SI)** model [81, 82] and **Hartree-Fock(HF)** model [83–85]. The IG model is the simplest and only takes in account the condensate-condensate atoms interactions. The SI model, takes in account the condensate-condensate atoms interactions, and also the interaction of the condensate cloud on the thermal atoms. Finally, the HF models takes in account the interactions present in the SI, and adds the effect of the repulsion of the thermal cloud on the condensate cloud. Moreover, a new numerical method developed by Nathan Welch [80] is used to solve the HF equations. Then, we discuss the validity of the different models in different regimes, varying the proportion of the thermal/condensate atoms density by changing the temperature, and also changing the interaction strength through the

Feshbach resonance. We observe that when the density of thermal atoms density becomes important  $> 50\%$ , the three model gives different results, and the  $\chi^2$  method shows that the HF model should be used in that regime.

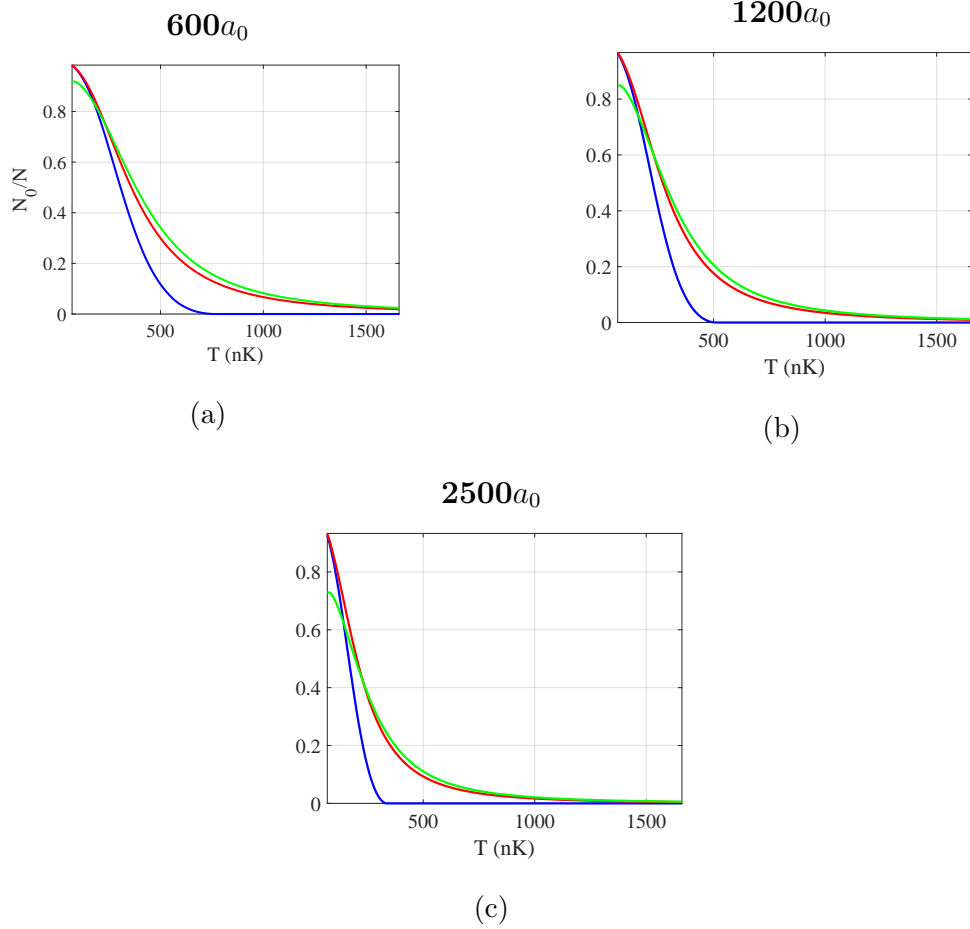


Figure 6.1: Condensed fractions against temperature for the different models (HF, SI, IG).

In Fig. 6.1 The fitting program takes as input the trapping frequencies and the spatial density, and gives the temperature and chemical potential as output. Here we scan the temperatures and set a constant chemical potential using the different fitting model [80] (HF, SI, IG) to give us the condensate fraction against temperature in a)b)c). We observe that the critical temperature of transition is lowered as we increase the interactions strength, this effect is more important in the case of the HF



model due to thermal atoms interactions important at the transition temperature.

## 6.1 The Gross Pitaevskii equation

In the section 3.1.3, we described the Bose-Einstein condensation for a gas without interaction. However, for a gas with an infinite compressibility, we can understand that interaction will have a considerable effect. Consequently, in this first part we describe the formalism used to characterize an interacting BEC in an harmonic trap. Elements of this discussion can be found in [24, 86].

In the formalism of the second quantification, the many body Hamiltonian describing  $N$  interacting bosons trapped by an external potential  $V_{\text{ext}}$  is given by:

$$\begin{aligned} \hat{H} = & \int d\mathbf{r} \hat{\Psi}^\dagger(\mathbf{r}) \left[ -\frac{\hbar}{2m} \nabla^2 + V_{\text{ext}}(\mathbf{r}) \right] \hat{\Psi}(\mathbf{r}) \\ & + \frac{1}{2} \int d\mathbf{r} d\mathbf{r}' \hat{\Psi}^\dagger(\mathbf{r}) \hat{\Psi}^\dagger(\mathbf{r}') V(\mathbf{r} - \mathbf{r}') \hat{\Psi}(\mathbf{r}') \hat{\Psi}(\mathbf{r}), \end{aligned} \quad (6.1)$$

where  $\hat{\Psi}(\mathbf{r})$  and  $\hat{\Psi}^\dagger(\mathbf{r})$  are the boson field operator, they can create or annihilate a particle at the position  $\mathbf{r}$ , and  $V(\mathbf{r} - \mathbf{r}')$  is the two-body inter-atomic potential.

For a large number  $N$  of bosons, the eq.(6.1) is hard to solve and require a lot of computational power, calculations using a Monte Carlo method for  $N = 10^4$  have been made in [87] to extract thermodynamics properties.

To simplify the problem, we use the Bogoliubov (1947) method [86]. We first separate the condensate contribution to the bosonic field operator. Then, the sum over all the states is separated between the particle in the ground state and the excited state:

$$\hat{\Psi}(\mathbf{r}) = \psi_0(\mathbf{r}) \hat{a}_0 + \sum_{i \neq 0} \psi_i(\mathbf{r}) \hat{a}_i, \quad (6.2)$$

where  $\hat{a}_i$  ( $\hat{a}_i^\dagger$ ) are the annihilation (creation) operators of a particles in the state  $\psi_i$ , and  $i = 0$  represents the condensate part. With the corresponding commutation

relations:

$$[\hat{a}_i, \hat{a}_j^\dagger] = \delta_{ij}, \quad [\hat{a}_i, \hat{a}_j] = 0. \quad (6.3)$$

In a BEC, the ground state is macroscopically occupied, i.e. that  $N_0$  is of the order of  $N$ . As a consequence, for temperatures low enough  $T < T_c$ , the commutation relations eq.(6.3) can be neglected, the field operator is then be replaced by  $a = a^\dagger = \sqrt{N_0}$ , and  $N_0 = \hat{a}_0 \hat{a}_0^\dagger$ . The normalisation condition allows us to write  $\Psi_0 = 1/\sqrt{V}$ , where  $V$  is the volume. We rewrite the eq.(6.2) as:

$$\hat{\Psi}(\mathbf{r}) = \sqrt{N_0/V} + \delta\hat{\psi}(\mathbf{r}), \quad (6.4)$$

where the first term describes the condensate and  $\delta\hat{\psi}(\mathbf{r})$  is treated as a perturbation. The generalisation of the mean field approximation of Bogoliubov for time dependant problem can be written in the following form:

$$\hat{\Psi}(\mathbf{r}, t) = \Phi(\mathbf{r}, t) + \delta\hat{\psi}(\mathbf{r}, t) \quad (6.5)$$

where  $\Phi(\mathbf{r}, t) = \langle \Psi(\mathbf{r}, t) \rangle$  is the mean value of the field operator, having the meaning of an order parameter. For an ensemble of  $N$  bosons of mass  $m$  trapped in a harmonic potential  $V_{\text{ext}}(r)$ , the wave function  $\Phi(\mathbf{r}, t)$  is a solution of the Gross Pitaevskii equation (GPE) [24]:

$$i\hbar \frac{\partial \Phi(\mathbf{r}, t)}{\partial t} = \left( -\frac{\hbar^2}{2m} \nabla^2 + V_{\text{ext}}(\mathbf{r}) + g|\Phi(\mathbf{r}, t)|^2 \right) \Phi(\mathbf{r}, t). \quad (6.6)$$

where  $g = \frac{4\pi\hbar^2 a}{m}$ , the interaction term (see section 6.1). We can obtain the ground state of eq.(6.6) by defining  $\Phi(\mathbf{r}, t) = \phi(\mathbf{r}) \exp(-i\mu t/\hbar)$ , where  $\mu$  is the chemical potential and  $\phi(\mathbf{r})$  a real function that satisfies the normalization condition  $\int d\mathbf{r} \phi^2 = N_0 = N$ . Therefore eq.(6.6) becomes:

$$\left[ \frac{-\hbar^2}{2m} \nabla^2 + V_{\text{ext}}(r) + g\phi^2(\mathbf{r}) \right] \phi(\mathbf{r}) = \mu\phi(\mathbf{r}). \quad (6.7)$$

This model was successful to describe results in experiments using density profile for  $a > 0$  [88], and its instability for  $a < 0$  [89, 90]. The mean field approximation is valid at low temperature and in the dilute limit where  $na^3 \ll 1$ .

**Effective interacting potential.** When the atomic density becomes important, the collisions lead to an interaction energy that becomes bigger than other energy of the system such as the thermal energy [74]. This interaction is approximated by a contact interaction, even if the inter-atomic separation is larger than the range of the potential. In this case we can calculate approximate the potential experienced by an atom in a gas with a density  $n$  by:

$$V_{\text{at}} = \lim_{V \rightarrow 0} \frac{1}{V} \sum_{i=1}^N \int g \delta(r - r_i) dr = gn = \frac{4\pi\hbar^2}{m} an. \quad (6.8)$$

A characteristic length scale is introduced, the healing length  $\xi$ , which is the distance over which the kinetic energy  $\approx \hbar^2/2m\xi$  is equal to the interaction energy  $\approx \frac{4\pi\hbar^2}{m} an$ , i.e. when the healing length is  $\xi = (8\pi na)^{-1/2}$ .

### 6.1.1 Thomas-Fermi approximation

In our experiment, the scattering length  $a > 0$ , corresponding to repulsive interaction. Moreover, the condition  $Na/a_{\text{ho}} \gg 1$  is fulfilled, in that regime the wave function  $\Phi(\mathbf{r}, t) = \sqrt{n(\mathbf{r})}$  is flattered, and the term  $\nabla^2 \sqrt{n(\mathbf{r}, t)}$  becomes small compared to the interaction term  $gn^2(\mathbf{r}, t)$ , consequently we can write:

$$n(\mathbf{r}) = \Phi^2(\mathbf{r}) = \frac{\mu - V_{\text{ext}}(\mathbf{r})}{g} \quad (6.9)$$

Using the normalization of the density, we integrate over space and obtain:

$$\mu_{TF} = \frac{\hbar\omega_{\text{ho}}}{2} \left( \frac{15N_0 a}{a_{\text{ho}}} \right)^{2/5}, \quad (6.10)$$

where  $a_{\text{ho}} = \sqrt{\hbar/(m\omega_{\text{ho}})}$ , is the oscillator length associated to the geometrical average  $\omega_{\text{ho}} = (\omega_x \omega_y \omega_z)^{1/3}$ . From eq.(6.10) we can obtain the radius of the condensate  $R_i$  where  $i = x, y, z$ , using the fact that:

$$n_{TF}(R_i) = 0, \quad (6.11)$$

and we obtain:

$$R_i = a_{\text{ho}} \left( \frac{15N_0 a}{a_{\text{ho}}} \right)^{1/5} \frac{\omega_{\text{ho}}}{\omega_i} \quad (6.12)$$

This would predict a chemical potential  $\mu = 0$  at the transition temperature. However, the interaction of the thermal clouds that are not taken in account here will have an influence on depleting the condensate part, and therefore increase the initial chemical potential necessary to add an atom into the condensate part (see section 6.4).

### 6.1.2 Hartree-Fock equations

We write the GPE equations for the condensed part and the thermal parts separately using eq.(6.6), adding the interactions terms describes in Fig. 6.2, we define the Hartree-Fock equations:

$$\left[ \frac{-\hbar^2}{2m} \nabla^2 + V_{ext}(r) + gn_0 + 2gn_{th} \right] \Psi_0 = \mu \Psi_0, \quad (6.13)$$

and

$$\left[ \frac{-\hbar^2}{2m} \nabla^2 + V_{ext}(r) + 2gn_0 + 2gn_{th} \right] \Psi_i = \epsilon_i \Psi_i, \quad (6.14)$$

where  $V_{ext}(r)$  is the trapping potential (see further details in section 5.4.5), and  $\epsilon$  the energy of the  $i^{th}$  excited level. The factors of 2 appear in the interaction terms as there are two asymmetric interactions between condensate and thermal-thermal atoms. These interactions are shown in the following figure:

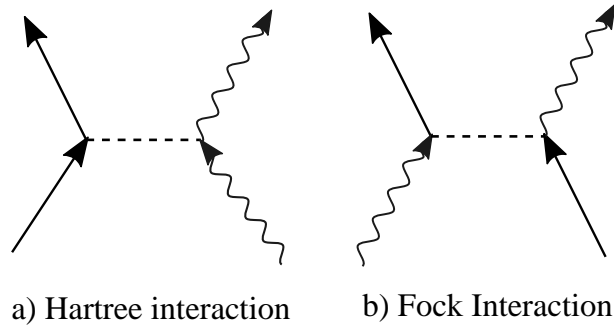


Figure 6.2: Feynman Diagrams of a) the Hartree interaction, between a ground state (solid line) and an excited state atom (wavy line), b) Fock interaction, exchanging an atom from the condensate with an atom from the thermal cloud. The interaction is carried out via a s-wave scattering (dashed line).

## 6.2 The fitting models

In this section, we describe the different models used to fit the density profiles obtained by performing in situ measurements. As described in section 5.5, pictures used for the spatial density profiles are taken from the top of the main chamber (see Figs. 6.3,6.4), we then have access to the density of the longitudinal axis. In the calculations, the density profiles are then integrated over the radial axis  $\mathbf{r}$  and fitted along the longitudinal axis  $\mathbf{z}$ . We describe three different models, the main difference among them is the types of interaction that are taken in account, from the least accurate one, the Ideal Gas model, to the most accurate one, the Hartre-Fock model. We will also discuss under which conditions these models are valid. These models are originally described in [74, 80].

### 6.2.1 Ideal gas

The IG or "bi-modal" model neglects all interactive contributions to the effective potential excepts condensate-condensate atoms interactions, which leads to write eq.(6.13) in the TF approximation:

$$[V_{\text{ext}}(r) + gn_0] \Psi_0 = \mu \Psi_0, \quad (6.15)$$

where the external potential is the optical trap described in section 5.4.2 and defined by:

$$V_{\text{ext}} = \frac{1}{2}m(\omega_r^2 r^2 + \omega_z^2 z^2), \quad (6.16)$$

with  $\omega_r = \sqrt{\omega_y \omega_z}$  the radial frequency and  $\omega_x$  the longitudinal frequency. Therefore, by multiplying eq.(6.15) by  $\Psi_0^*$ , we obtain the density for the condensate part:

$$n_0 = \frac{1}{g}(\mu - V_{\text{ext}})\delta(V_{\text{ext}} < \mu). \quad (6.17)$$

Now, by doing a radial integration in eq.(6.17), we obtain the axial density profile for the condensate atoms:

$$n(z) = \begin{cases} \frac{\pi}{gm\omega_r^2}(\mu - \frac{1}{2}m\omega_z^2 z^2)^2, & |z| < \sqrt{\frac{2\mu}{m\omega_z^2}} \\ 0, & \text{else.} \end{cases} \quad (6.18)$$

In this model the thermal cloud is described by a Maxwell-Boltzmann approximation, neglecting the Bose-enhancement. The Maxwell-distribution used to describe the thermal atoms is given by:

$$f(\epsilon_i) = \frac{1}{e^{\frac{\epsilon_i - \mu}{k_B T}} - 1} \approx e^{\frac{-\epsilon_i + \mu}{k_B T}}, \quad (6.19)$$

with  $\epsilon_i = \frac{\hbar^2 k^2}{2m} + V_{\text{ext}}$ . Then to find the spatial density distribution we integrate over all the momenta  $k$  [81]:

$$n_{\text{th}}(z, r) = \left( \frac{mk_B T}{2\pi\hbar^2} \right)^{3/2} \exp\left( \frac{\mu - V_{\text{ext}}}{k_B T} \right). \quad (6.20)$$

Moreover, eq.(6.20) is radially integrated to find the line density along  $z$  to give:

$$n_{\text{th}}(z) = \sqrt{\frac{m}{2\pi}} \frac{(k_B T)^{5/2}}{\hbar^3 \omega_r^2} \exp\left( \frac{\mu - V_{\text{ext}}}{k_B T} \right). \quad (6.21)$$

This model does not take into account the interactions of the thermal atoms and should be used only for low temperatures, when the thermal part is negligible. A fit of this model to the experimental data is shown in Fig. 6.5.

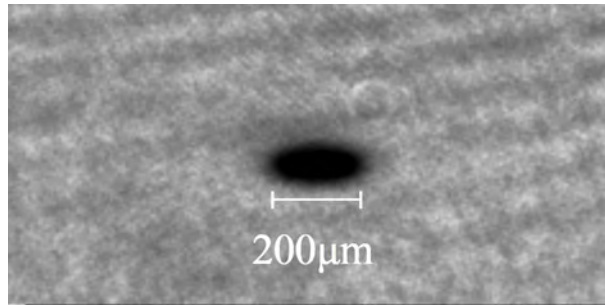


Figure 6.3: Raw image of the BEC. From the vertical imaging.

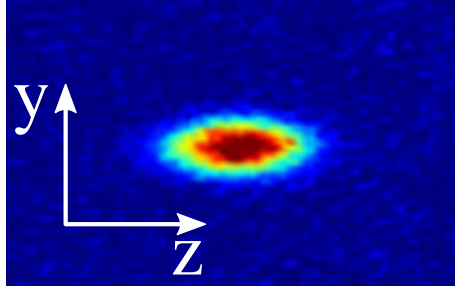


Figure 6.4: Density profile of the BEC.

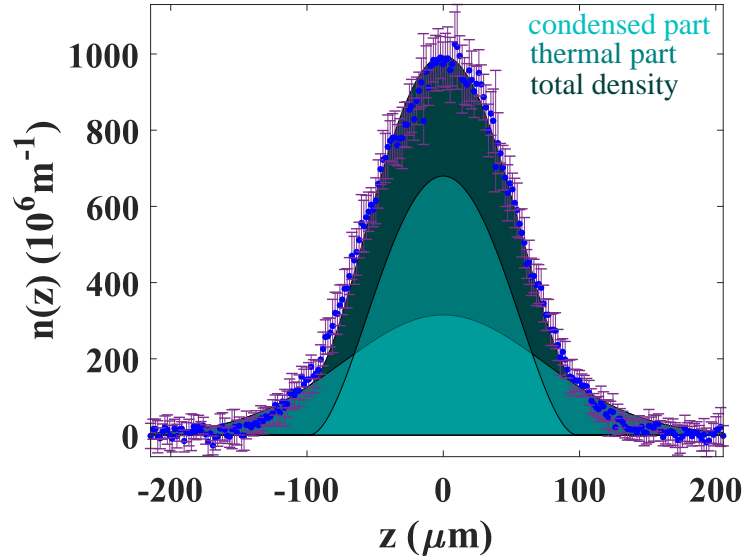


Figure 6.5: Fitting of the atomic density using the (IG) model. The experimental data points (blue squares) are the average over 10 density profiles (see section 6.3).

### 6.2.2 Semi-ideal

Here we present a more accurate model taking more terms of the Hartree Fock eqs.(6.13,6.14) into account, so-called the semi-ideal model. Assuming that the thermal part density is negligible, eqs.(6.13,6.14) can be written as:

$$\left[ \frac{-\hbar^2}{2m} \nabla^2 + V_{ext}(r) + gn_0 + 2gn_{th} \right] \Psi_0 = \mu \Psi_0, \quad (6.22)$$

and

$$\left[ \frac{-\hbar^2}{2m} \nabla^2 + V_{ext}(r) + 2gn_0 + \cancel{2gn_{th}} \right] \Psi_i = \epsilon_i \Psi_i, \quad (6.23)$$

In the eq.(6.22) and eq.(6.23), the thermal interaction term is neglected, because we suppose that the temperature is low enough to have a high condensate fraction.

However, the thermal cloud is described by the Bose-Einstein distribution:

$$n_{th} = \frac{\rho(E)dE}{e^{\frac{E-\mu}{k_B T}} - 1}, \quad (6.24)$$

where we assume that enough thermal states are occupied, therefore  $E$  is continuous and  $\rho(E)$  is the density of state. We use the same trapping frequency as in the Ideal gas model, i.e. we use  $\omega_r$  and  $\omega_z$ . We define the energy of the system as:

$$E(k, x, r) = \frac{\hbar^2 k^2}{2m} + \frac{m}{2}(\omega_r^2 r^2 + \omega_z^2 z^2) + 2gn_0(z, r), \quad (6.25)$$

and  $\rho(k, z, r) = 2\pi k^2 dk 2\pi r dr dx$ . The effective potential  $U_{\text{eff}}$  for the thermal is given by:

$$U_{\text{eff}}(z, r) = \frac{m}{2}(\omega_r^2 r^2 + \omega_z^2 z^2) + 2gn_0(z, r). \quad (6.26)$$

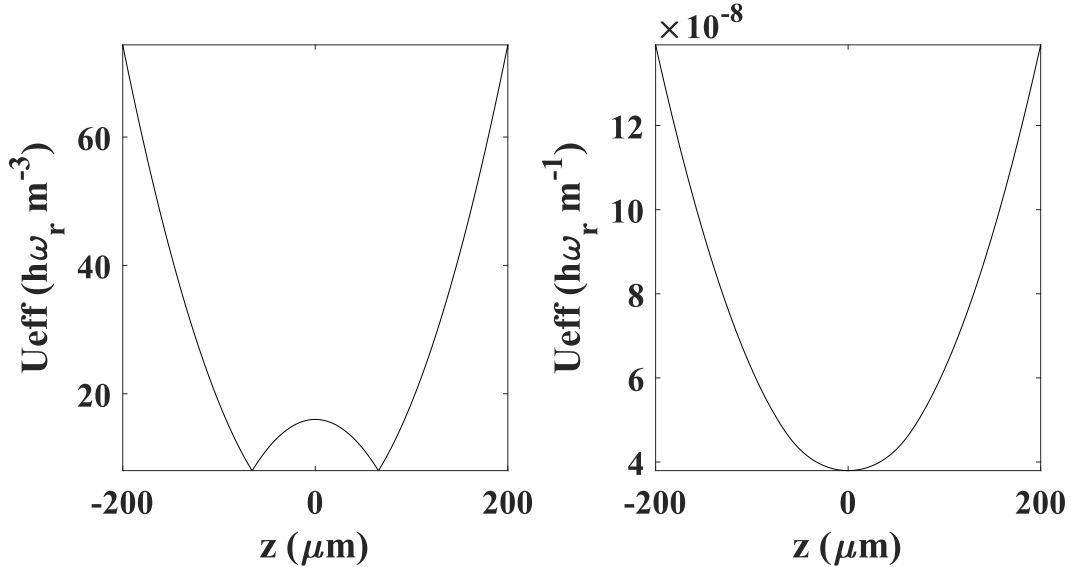


Figure 6.6: The plot of  $U_{\text{eff}}$  on the left hand side is along  $(x, r = 0)$ . The plot of  $U_{\text{eff}}$  on the right hand side is after integration over  $r$ . The parameters for this plot are:  $\omega_r = 200\text{Hz}$ ,  $\omega_z = 25\text{Hz}$ ,  $T = 80\text{nK}$ ,  $\mu = 5\hbar\omega_r$ ,  $a = 1600a_0$ .



We remove the  $k$ -dependence by integrating over all the momentum states. The method described in appendix B gives us:

$$\begin{aligned}
 n_{th}(x, r) &= \frac{4\pi}{(2\pi)^3} \int_0^\infty \frac{k^2 dk}{e^{\frac{E-\mu}{k_B T}} - 1} \\
 &= \frac{2}{\sqrt{\pi}} A_k \int_0^\infty \frac{X^{1/2} dX}{e^X/Z - 1} \\
 &= A_k \sum_{l=1}^\infty \frac{Z^l}{l^{3/2}}
 \end{aligned} \tag{6.27}$$

with the associate variables:

$$A_k = \left( \frac{mk_B T}{2\pi\hbar^2} \right)^{3/2} \tag{6.28}$$

$$X = \frac{\hbar^2 k^2}{2mk_B T} \tag{6.29}$$

$$Z = \exp \left[ - \left( \frac{m}{2} (\omega_r^2 r^2 + \omega_x^2 x^2) + 2gn_0(z, r) - \mu \right) / k_B T \right] \tag{6.30}$$

Then, in Fig. 6.7, we plot the densities  $n(z, r)$  and  $n_{th}$  before integration along  $(z, r = 0)$  and after integration. The particular shape of the thermal cloud density in Fig. 6.7 of the left hand side is given by the effective potential  $U_{\text{eff}}$  given by the left hand side plot in in Fig. 6.6. After integration over  $r$  the shape of the effective potential and the atomic density is changed (see Fig. 6.7 and Fig. 6.6), this has been observed in [74, 91].

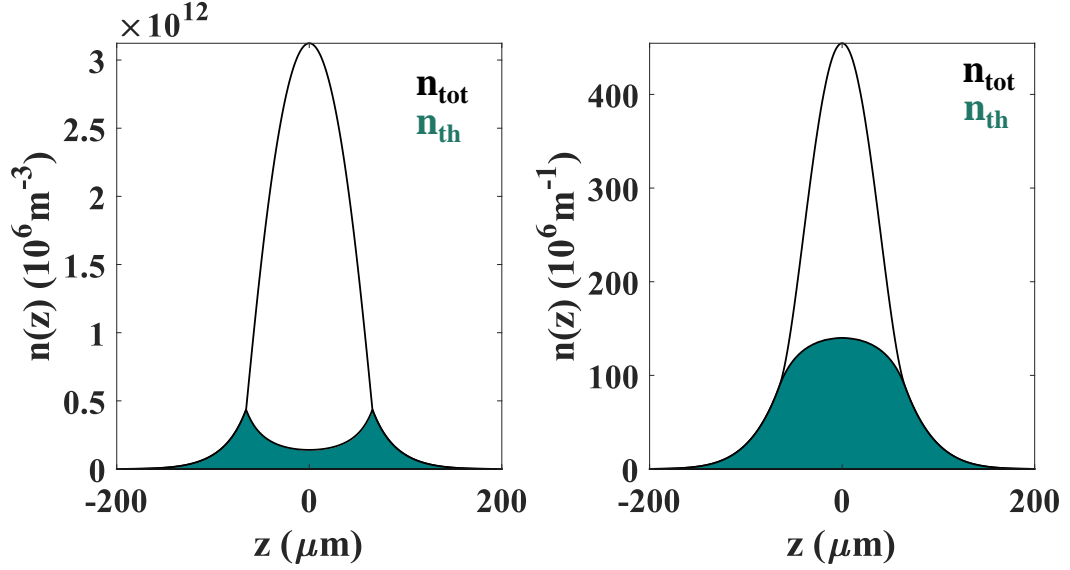


Figure 6.7: Plot the densities  $n(z, r)$  and  $n_{\text{th}}$  before integration along  $(z, r = 0)$  (left hand side) and after integration (right hand side). The parameters for this plot are:  $\omega_r = 200\text{Hz}$ ,  $\omega_z = 25\text{Hz}$ ,  $T = 80\text{nK}$ ,  $\mu = 5\hbar\omega_r$ ,  $a = 1600a_0$ .

**Analytical solution.** In general, this problem can only be solved numerically [82]. However, in [24] the interactions are treated as a perturbation, and an analytical solution can be found, using eq.(6.10), we define the following scaling parameter:

$$\eta = \frac{\mu(T=0)}{k_B T_c^0} = \frac{1}{2} \zeta(3)^{1/3} \left( 15 N^{1/6} \frac{a}{a_{ho}} \right)^{2/5} \approx 1.57 \left( N^{1/6} \frac{a}{a_{ho}} \right)^{2/5}, \quad (6.31)$$

which is the ratio between the chemical potential defined in eq.(6.10) and the thermal energy at  $T = 0$  in the non interacting case (see eq.(3.11)). The order parameter  $\eta$  mainly depends on the ratio  $a/a_{ho}$ , which is usually  $< 1$  for weakly interaction BEC, however in our case, considering that we can tune the inter-atomic interactions, the ratio can reach a value of 1. Using the approximation that  $\eta$  is small [24, 81] found the following relation:

$$\frac{N_0}{N} = 1 - t^3 - \eta \frac{\zeta(2)}{\zeta(3)} t^2 [1 - t^3]^{2/5}, \quad (6.32)$$

where  $t = N_0/N$ , in eq.(6.32) the first term is eq.(3.14) and the second term represents the first correction of the semi-ideal model with  $\eta$  small. Using the same

approximation [83] shows that we can write the shift in critical temperature such as:

$$\frac{\Delta T_c}{T_c^0} \approx -1.33 \frac{a}{a_{ho}} N^{1/6} = -0.43 \eta^{2/5}, \quad (6.33)$$

where  $\Delta T_c = T_c - T_0^c$ . Moreover in [92], experimental measurements demonstrate that a second order correction depending on the scattering length  $a$  is needed to describe the shift in critical temperature for strongly interacting gas.

### 6.2.3 Hartree-Fock

The semi-classical model is suitable for low temperatures due to the low density of thermal atoms, however when temperatures are close to  $T_c$ , this model leads to inaccuracies. Therefore, to improve the model, the repulsion caused by the thermal cloud density is included into the GPE equations :

$$\left[ \frac{-\hbar^2}{2m} \nabla^2 + V_{ext}(r) + gn_0 + 2gn_{th} \right] \Psi_0 = \mu \Psi_0, \quad (6.34)$$

and

$$\left[ \frac{-\hbar^2}{2m} \nabla^2 + V_{ext}(r) + 2gn_0 + 2gn_{th} \right] \Psi_i = \epsilon_i \Psi_i, \quad (6.35)$$

to give the condensate density part:

$$n_0(z, r) = \max \left\{ \frac{1}{g} \left[ \mu - \frac{m}{2} (\omega_r^2 r^2 + \omega_z^2 z^2) - 2gn_{th} \right], 0 \right\}, \quad (6.36)$$

and the thermal density part:

$$n_{th}(z, r) = \left( \frac{mk_B T}{2\pi \hbar^2} \right)^{3/2} \sum_{l=1}^{\infty} \frac{Z_{full}^l}{l^{3/2}}, \quad (6.37)$$

where

$$Z_{full} = \exp \left[ - \left( \frac{m}{2} (\omega_r^2 r^2 + \omega_z^2 z^2) + 2gn_0(z, r) + 2gn_{th}(z, r) - \mu \right) / k_B T \right]. \quad (6.38)$$

We define the effective potential as (see Fig. 6.8):

$$U_{\text{eff}} = \frac{m}{2}(\omega_r^2 r^2 + \omega_z^2 z^2) + 2gn_0(z, r) + 2gn_{\text{th}}(z, r) \quad (6.39)$$

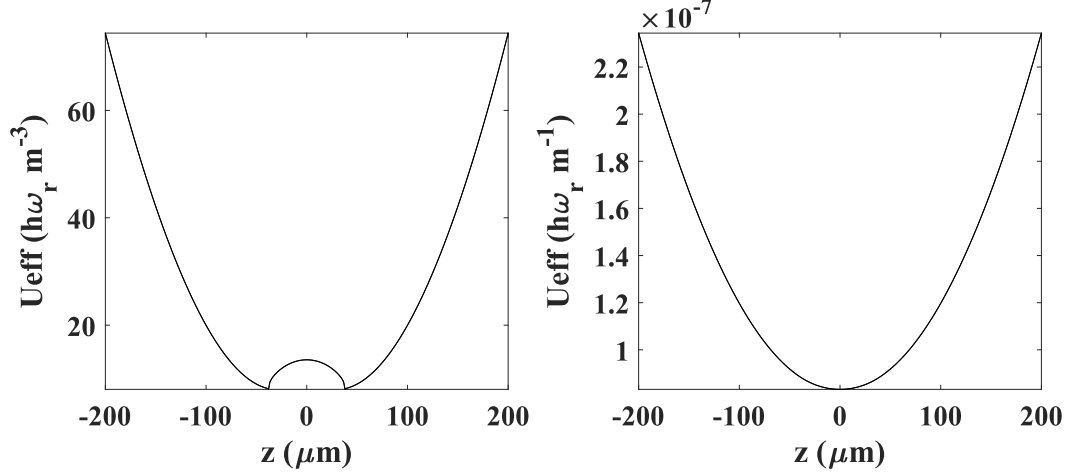


Figure 6.8: The plot of  $U_{\text{eff}}$  on the left hand side is along  $(x, r = 0)$ . The plot of  $U_{\text{eff}}$  on the right hand side is after integration over  $r$ . The parameters for this plot are:  $\omega_r = 200\text{Hz}$ ,  $\omega_z = 25\text{Hz}$ ,  $T = 80\text{nK}$ ,  $\mu = 5\hbar\omega_r$ ,  $a = 1600a_0$ .

and the corresponding atomic density profiles:

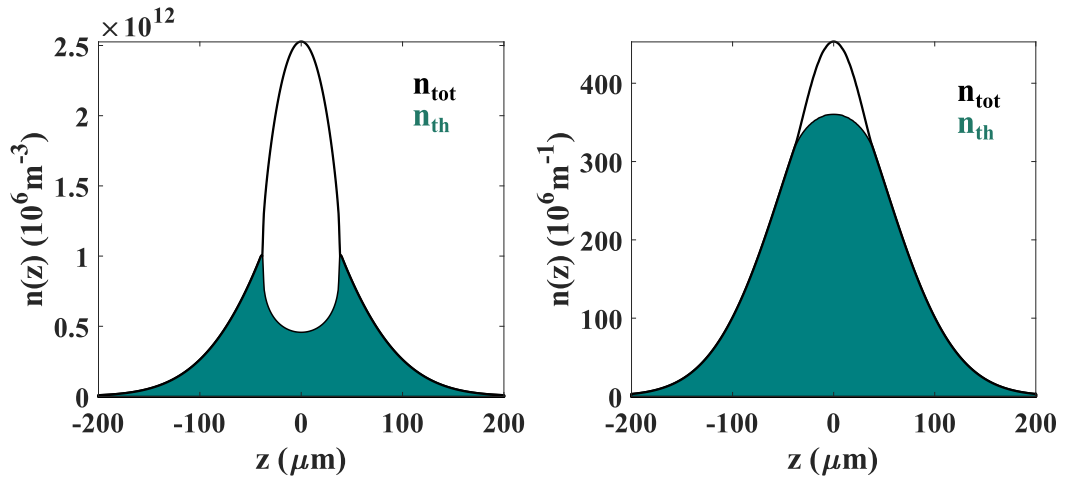


Figure 6.9: Plot the densities  $n(z, r)$  and  $n_{\text{th}}$  before integration along  $(z, r = 0)$  (left hand side) and after integration (right hand side). The parameters for this plot are:  $\omega_r = 200\text{Hz}$ ,  $\omega_z = 25\text{Hz}$ ,  $T = 80\text{nK}$ ,  $\mu = 5\hbar\omega_r$ ,  $a = 1600a_0$ .

An iterative scheme can be used to solve eq.(6.36) and eq.(6.37), but it requires considerably larger computational resources than the two models (IG and SI) given above.

In order to be able to fit this more complex model to the experimental data, we use a method, where the summation and iterations required are solved just once and then interpolated (see Fig.6.10) to give the fully interactive densities, this method was developed by Nathan Welch [80]. The eq.(6.36) is injected in eq.(6.37) to eliminate the condensate part density. Then, both sides of eq.(6.37) contain  $n_{th}$ , therefore we can write the following transcendental equation:

$$X = a \sum_{l=1}^{\infty} \frac{e^{-l|b+X|}}{l^{3/2}}, \quad (6.40)$$

with

$$a = \frac{2a_s}{\hbar} \sqrt{\frac{2k_B T m}{\pi}} \quad (6.41)$$

and

$$b = \frac{\frac{m}{2}(\omega_r^2 r^2 + \omega_z^2 z^2) - \mu}{k_B T} \quad (6.42)$$

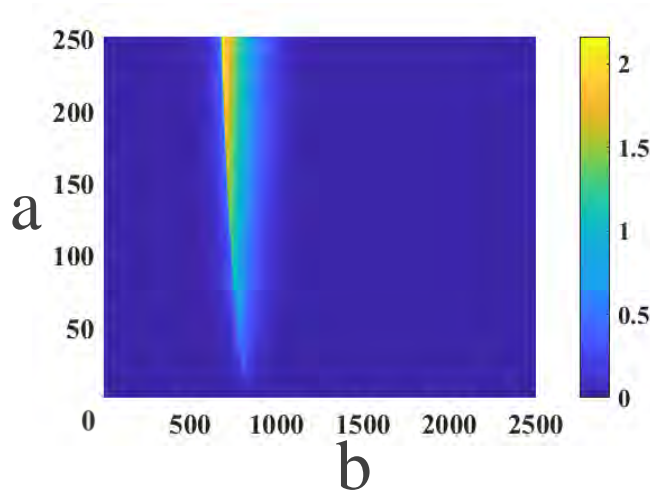


Figure 6.10: Interpolation of the transcendental equation eq.(6.40).[80].

The absolute exponent in eq.(6.40) allows the density distribution of the thermal cloud to be calculated in both the (mainly) condensate and (mainly) non-condensate regions. The self-interacting cloud can then be found using:

$$n_{\text{th}}(z, r) = \frac{k_B T}{2g} X(a[T], b[r, z, \mu, T]). \quad (6.43)$$

### 6.2.4 Comparison between the SI and the HF model

In Fig. 6.11, we compare the two most relevant models, the SI and HF models. On the left hand side the temperature is very low  $T = 60\text{nK}$ , on the right hand side  $T = 150\text{nK}$ . We see that the models give similar results at low temperature when the density of thermal atoms  $n_{\text{th}}$  is low, and diverge when the temperature approach the critical temperature  $T_c$ , due to the influence of the density of the thermal atoms.

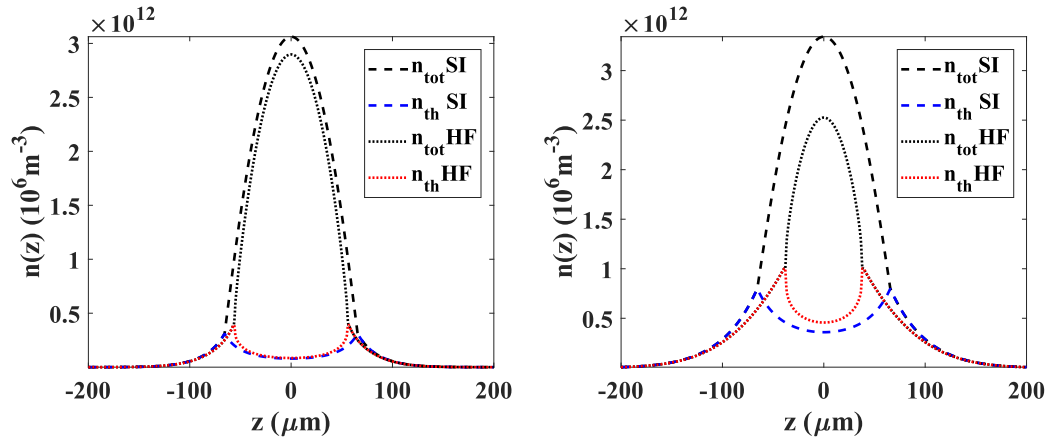


Figure 6.11: The parameters for this plot are:  $\omega_r = 200\text{Hz}$ ,  $\omega_z = 25\text{Hz}$ ,  $\mu = 5\hbar\omega_r$ ,  $a = 1600a_0$ ,  $T = 60\text{nK}$  for the left hand side figure and  $T = 150\text{nK}$  for the right hand side figure.

## 6.3 Fitting program

In this section, we describe the way the spatial atomic density measurements are processed and analysed by the fitting program. We first process the data in four individual steps, the three first step are depicted in Fig. 6.12.

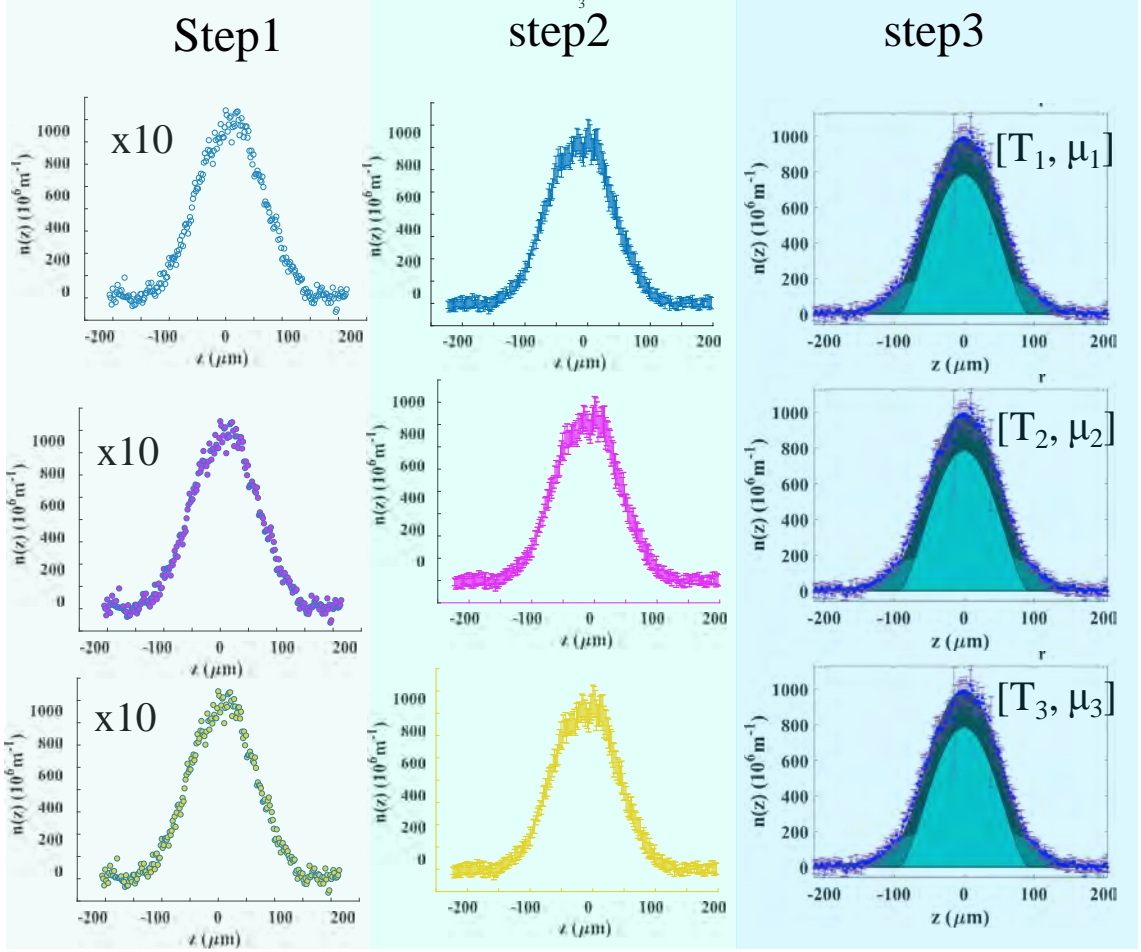


Figure 6.12: In order to compensate the spatial fluctuation of the lithium atoms, we take 30 absorptions images for each value of the trapping frequencies. Then we separate the data into 3 packs of 10 images, these 10 images are then average to give 3 different distributions with a standard error. Then the 3 different distributions are fitted with the different models (IG, SI, HF) to give 3 values of temperature and chemical potential, which leads to an estimation of the standard error for  $T$  and  $\mu$ .

1. **Step 1:** We take 30 In-situ absorption images for a particular set of trapping frequencies and interactions strength  $[\omega_r, \omega_z, a]$ .
2. **Step 2:** The 30 images are divided in three equal parts, each part is summed-up and averaged. Note that for the average, the different density distributions need to be centred, to do so a SI fitting is performed. For this fit all inputs

are free parameters in order to find the center of the distribution  $z_0$ .

3. **Step 3:** From the previous step, we obtain three density distribution with a standard error, which are then fitted with the IG, SI and HF models.
4. **Step 4:** From the fits of step 3, we obtain a set of three sets  $[T + \Delta T, \mu + \Delta\mu]$  for each model.

**Chi-squared method.** We define the quantity  $\chi^2$  that is used to define the goodness of a fit:

$$\chi^2 = \sum_i \frac{(y_i - y(x_i))^2}{\alpha_i}, \quad (6.44)$$

With  $\alpha_i$  the error bar,  $y_i$  the experimental value and  $y(x_i)$  the value of the fit. The  $\chi^2$  is summed over all the data points and should be minimised to obtain the best fit. A complete study of the least square fitting is described in [79]. The original program proposed by N.Welch used a Matlab function **fminsearch** to find the best  $[T, \mu]$  couple of parameters in order to minimise the  $\chi^2$ . However for the HF model, the program had difficulties to find a solution due the higher complexity of the HF model. We therefore replace the original function by **fminsearchbnd** a modified Matlab function where boundaries can be fixed  $[T_0 \pm \Delta T, \mu_0 \pm \Delta\mu]$  so the program is looking for values of  $[T, \mu]$  in a reasonable range. This helps the algorithm finding the solution faster in the HF model case, also a starting point is set for the algorithm  $[T_0, \mu_0]$ . These initial values are the final values found by the SI model.

## 6.4 Results

In this section, we discuss the results of the fitting using the Ideal Gas model, the Semi Ideal model and the Hartree-Fock model to our actual data. The main objective is to determine temperature and chemical potential using the trapping frequencies, total atom numbers and one-dimension density profiles as input. From



these outputs, we can also obtain the condensate and thermal fraction of the atoms. In Fig. 6.13, we represent the condensate fraction against the temperature obtained by the fitting of the three different models (see section 6.3) with the interaction strength set at  $a = 1600a_0$ , we also plot analytical solution of the IG [24] and SI model [81] as reference. Atom clouds are prepared by setting the power of the dipole trap to different final values to reach different temperatures, therefore the trapping potential  $\omega_{ho}$  varies, consequently we plot the condensate fraction against the temperature and the trapping frequency. The total atom number in the cloud ranges from  $1,5 \cdot 10^5$  to  $2,5 \cdot 10^5$ .

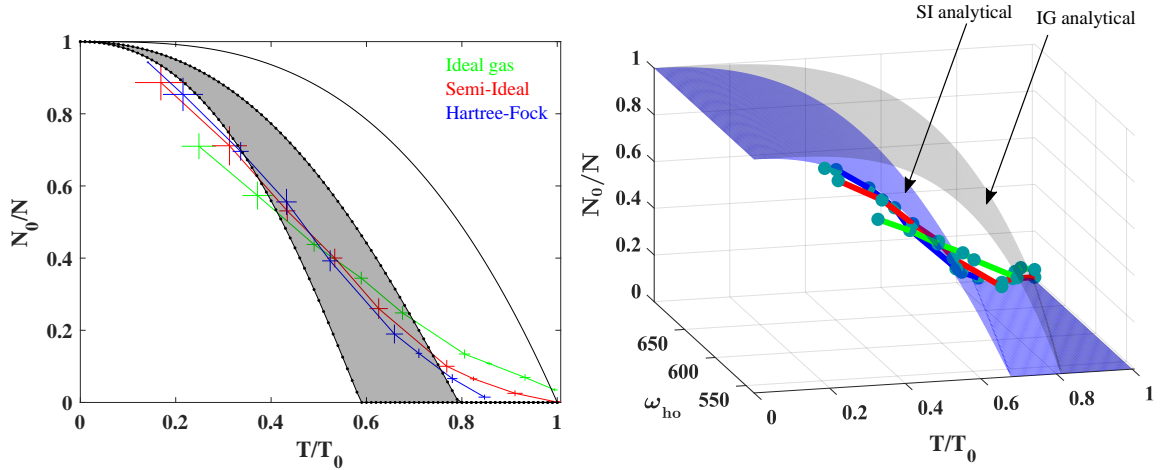


Figure 6.13: Plot of the condensate fraction against the temperature. On the left hand side, the shaded area is bounded by the analytical solution [81] for SI model where  $\eta = 0.72$  (see eq.(6.32)) for two different values of trapping frequencies  $\omega_{ho}$ , these two values are the trapping frequencies at the beginning and the end of the evaporation. The solid line represents the ideal gas eq.(3.3). On the right hand side we plot the the same functions and data adding a third dimension, the trapping frequency that varies during the measurements when we change the depth of the dipole trap to change the temperature.  $T_0$  is the transition temperature from the ideal case defined in eq.(3.11).

For temperatures  $T < 0.5T_c$ , the three models give approximately the same condensate fraction, because for these temperatures the condensate fraction is high enough so that the effect of the thermal atoms becomes less important, therefore the three models converge to the same condensate fraction value, and the SI and HF data points agree well with the SI analytical model. For temperatures  $T > 0.5T_c$ , we see that the three models diverge, because of the more important fraction of thermal atoms, and therefore the thermal atoms interaction term in the HF equations is bigger, the thermal atoms deplete the condensate cloud. The SI model overestimates the condensate fraction compared to the Hartree-Fock model when thermal interactions are significant, the SI fitting points diverge from the SI analytical solution, and the HF fitting points are closer to the SI analytical solution. Moreover, The Hartree-Fock model gives a lower temperature of transition than the SI model, because of the importance of the thermal cloud atoms at this stage of the condensation, the HF model is a more realistic model to determine the transition temperature. This difference between the SI model and the HF model has been measured with  ${}^{87}\text{Rb}$  at lower interaction strength  $a \approx 100a_0$  [88].

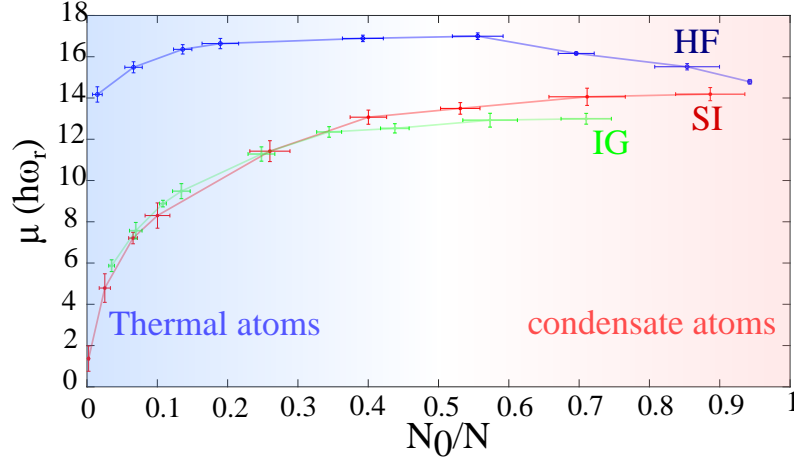


Figure 6.14: Plot of the chemical potential for the three different models against the condensate fraction. At low condensate fraction, i.e. high thermal fraction the SI and GI models tend to zero, on the other hand the HF model tends to a finite value due the interaction energy of the thermal cloud.

In Fig. 6.14, we plot the chemical potential found through the fitting program, the difference between the SI and IG model is small. The chemical potential starts from a value around zero, and goes asymptotically to a finite value when the condensate fraction increases. Due to the thermal atoms density interactions taken in account in the HF model, the initial value of the chemical potential, when almost all the atoms are in the thermal part is  $\mu_c \approx 2gn_{th,0} = 14\hbar\omega_r$  with  $n_{th,0}$  the thermal cloud density:

$$n_{th,0} \approx \left( \frac{mk_B T}{2\pi\hbar} \right)^{3/2} \gamma(3/2). \quad (6.45)$$

For lower temperature, the chemical potential is given by  $\mu_{HF} \approx 16\hbar\omega_r$ . In the case of the SI model, when almost all the atoms are in the thermal part, the chemical potential is  $\mu_c \approx 0$ . When the condensate atoms dominates the chemical potential converges to the chemical potential of the HF model  $\mu_{SI} \approx 14\hbar\omega_r$ . This means that the chemical potential is mostly determined by the interaction energy of the system. At low temperature the interaction energy of the condensate atoms dominate, and at high temperature the interaction energy stems mainly from the thermal atoms.

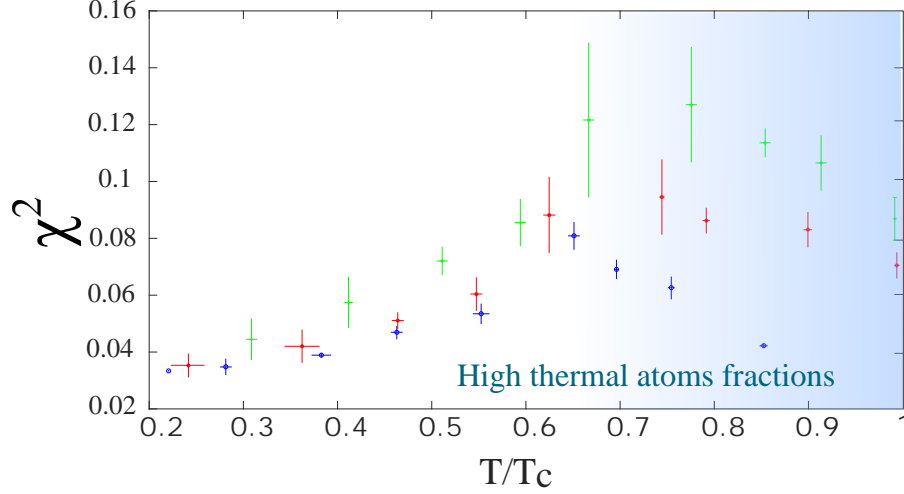


Figure 6.15:  $\chi^2$  for fits of the different models (blue - HF model, red - SI model, green - IG model). For the set of data shown in Fig. 6.13.

In order to determine which model fits the experimental data best, we calculate  $\chi^2$  value for each fit for a range of clouds with different temperatures. For this we use the same experimental data set as in Fig. 6.15. The  $\chi^2$  is always lower in the case of the HF model. For high temperature, which is expected, the HF model seems to fit better the experimental data. When the temperature decreases the  $\chi^2$  of the three models converge, even if the relation  $\chi^2[HF] < \chi^2[SI] < \chi^2[IG]$  is still verified at all the temperatures.

## Higher interactions

In this paragraph, we perform the same measurements at different scattering length  $1600a_0$ ,  $3500a_0$ ,  $4500a_0$  and we observe a decrease in the transition temperature when we increase the scattering length (see Fig. 6.17), that agrees with the observation in [92, 93]. Moreover, by increasing the interaction strength, we see that the chemical potential is increased (Fig. 6.16), which makes sense since the chemical potential is related to  $gn$ , with  $g$  depending on the scattering length (see section 2). In Fig. 6.17 a)b), we see that the critical temperature  $T_c$  is lowered as the interactions

are increased. In Fig. 6.17 c)d) the statistical analysis also show that the HF model is more suitable when the thermal atoms part is  $> 50\%$ .

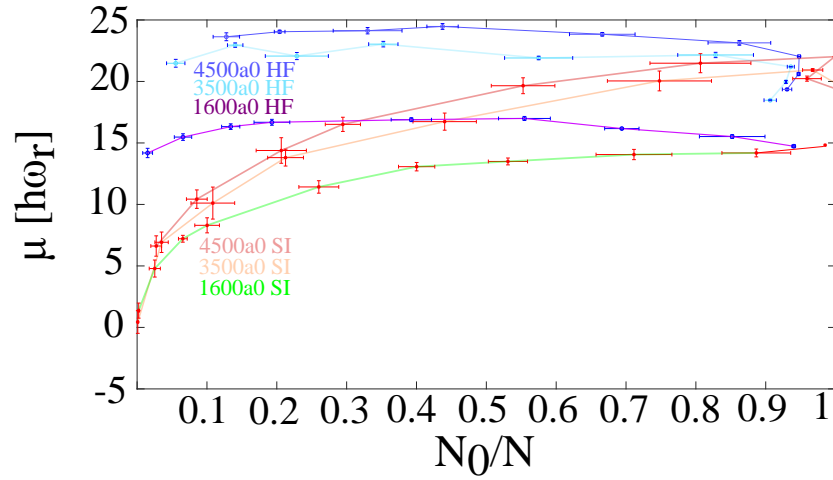


Figure 6.16: Chemical potential against condensate part at different interaction strength for the HF and SI model. (blue - HF model, red - SI model)

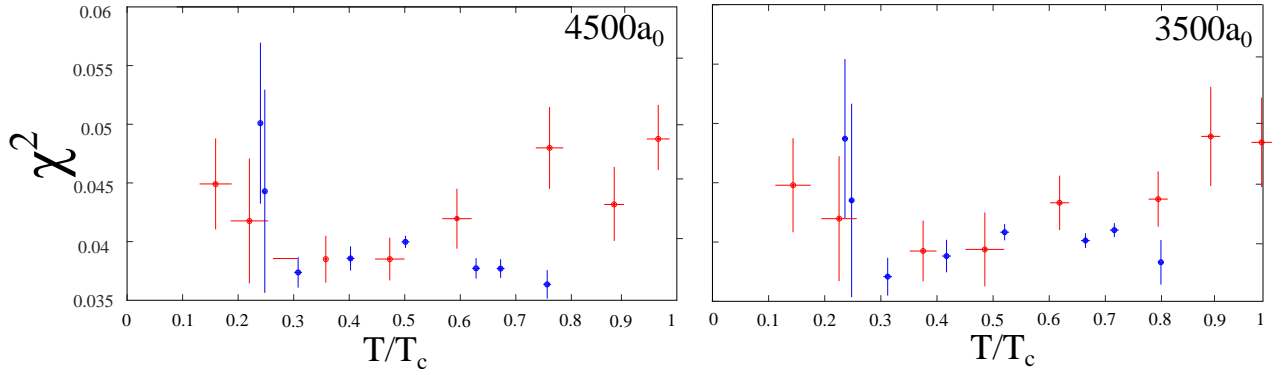


Figure 6.17: The two plots represent the  $\chi^2$  analysis for the measurements at  $a = 3500a_0$  and  $a = 4500a_0$  (see Fig. 6.18).

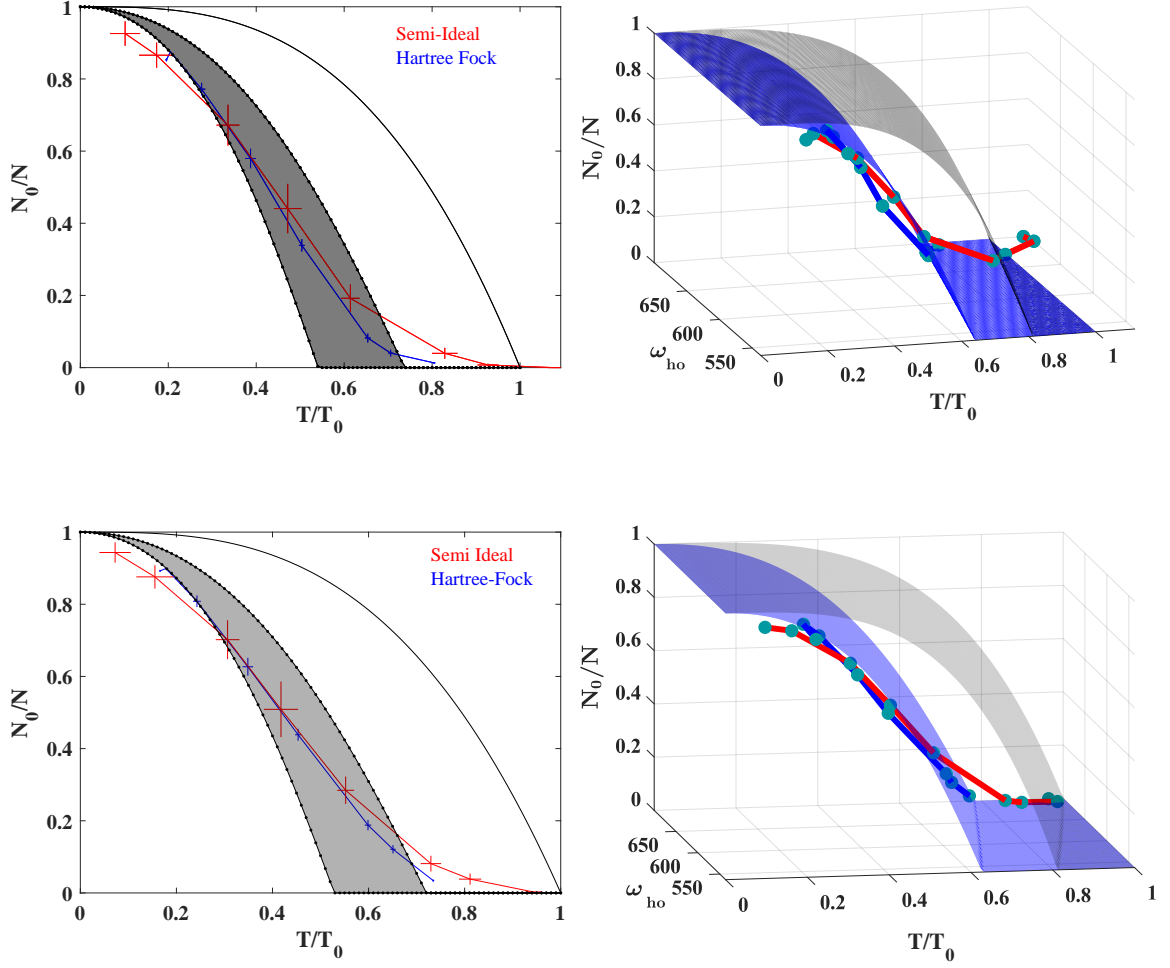


Figure 6.18: Plot of the condensate fraction against the temperature at  $a = 3500a_0$ . On the left hand side, the shaded area is bounded by the analytical solution for SI model where  $\eta = 0.93$  (see eq.(6.32)) for two different values of trapping frequencies  $\omega_{ho}$ , these two values are the trapping frequencies at the beginning and the end of the evaporation. The solid line represents the ideal gas eq.(3.3). On the right hand side we plot the the same functions and data adding a third dimension, the trapping frequency that vary during the measurements.  $T_c$  is the transition temperature from the ideal case defined in eq.(3.11). c) same as a) and d) same as b), with  $a = 4500a_0$  and  $\eta = 1.02$ .

## 6.5 Radius Measurement

In this section, we are going to focus on a different approach, allowing us to find an analytical formula for the HF model between the **radius** of the condensate  $R$  and the condensate fraction. The radius of the condensate in the TF approximation is directly related to the chemical potential, using eq.(6.17) for  $x = \mathbf{R}$  and after radial integration, we obtain [80]:

$$R_z = \sqrt{\frac{2(\mu - gn_{\text{th},0})}{m\omega_z^2}}, \quad (6.46)$$

with ,

$$n_{\text{th},0} \approx \left( \frac{mk_B T}{2\pi\hbar} \right)^{3/2} \gamma(3/2), \quad (6.47)$$

the peak thermal cloud density. In eq.(6.46) the presence of the  $gn_{\text{th},0}$  term is necessary to have the radius of the condensate  $R_x = 0$  at the temperature  $T_c$ , because the chemical potential is different from zero at the transition in the HF model (see Fig. 6.14).

The original idea is originally described in [1], however in this paper the conditions are different, as they use time of flight imaging, and we are using in-situ imaging which is according to [1] more suitable for the theoretical model developed in the paper. Moreover, we are able to tune the scattering length to vary the inter-atomic interactions.

### 6.5.1 Relation between the radius of the condensate and the condensate fraction using ideal gas model

In this section, we describe the theory and the main approximation developed in [1] in order to find the analytical formula between  $R$  the radius of the condensate and  $N_0$  the number of atoms in the condensate part. The density of the condensate part equation is similar to the ideal gas model:

$$n_0(\mathbf{r}) = \frac{\mu - V(\mathbf{r})}{g} \quad (6.48)$$

where  $V(\mathbf{r}) = 1/2m\omega_r^2 r^2$  is the external potential,  $\mu$  the chemical potential and  $g$  the interaction strength. For an isotropic potential, the density profile corresponds to an inverted parabola, with  $R$  the radius of the parabola, determined by the condition,  $\mu = V(R)$ . The normalization of the wavefunction gives us [94]:

$$\int |\Psi(\mathbf{r})|^2 d^3\mathbf{r} = \int |n_0(\mathbf{r})|^2 d^3\mathbf{r} = N_0, \quad (6.49)$$

by integration of eq.(6.48) over the space  $\mathbf{r}$  and using eq.(6.49), we obtain a formula for the chemical potential:

$$\mu = \left[ \left( \frac{15gN_0}{8\pi} \right)^2 \left( \frac{m\omega_{ho}^2}{2} \right)^3 \right]^{1/5}. \quad (6.50)$$

Inserting eq.(6.50) into the condition  $\mu = V(R)$  gives us a relation between chemical potential and atom number in the condensate:

$$\frac{R^5}{N_0} = \frac{15}{4\pi} \frac{g}{m\omega_{ho}^2} = C, \quad (6.51)$$

where  $C$  is a constant depending on the inter-atomic interactions and the trapping frequencies. Applying the same method as in section 6.1.1, we can define eq.(6.51) in an anisotropic trapping potential:

$$\frac{R_i^5}{N_0} = \frac{15}{4\pi} \frac{g}{m\omega_{ho}^2} \left( \frac{\omega_{ho}}{\omega_i} \right)^{5/2} = C_i. \quad (6.52)$$

### 6.5.2 First correction to the ideal model

We have first found the relation eq.(6.51), that gives that the ratio  $\frac{R^5}{N_0}$  equals to a constant  $C$ . Now, we define the following relation using the GPE and the TF approximation:

$$n_0(\mathbf{r}) + n_T(\mathbf{r}) = \frac{\mu - V(\mathbf{r})}{g}, \quad (6.53)$$

where  $n_T$ , the density of thermal atoms, from that we obtain the following relation [1]:

$$\frac{R_i^5}{N_0} = C_i \left( \frac{2}{N_0/N} - 1 \right). \quad (6.54)$$



### 6.5.3 Analytical Hartree Fock model

In this section, we describe a simplified Hartree-Fock model, and we follow closely the developement in [1]. This model is valid [81, 95, 96] when the thermal energy  $k_B T \gg \hbar\omega$ , i.e. when thermal atoms cloud has a larger spatial extent than the oscillator  $a = \sqrt{\hbar/m\bar{\omega}}$ . In this approximation the density distributions are given by:

$$n_0(\mathbf{r}) = \frac{\mu - V(\mathbf{r}) - 2gn_T(\mathbf{r})}{g} \Theta(\mu - V(\mathbf{r}) - 2gn_T(\mathbf{r})) \quad (6.55)$$

$$n_T(\mathbf{r}) = \frac{1}{\lambda_T^3} g_{3/2} \left( e^{-\frac{V(\mathbf{r}) + 2gn_T(\mathbf{r}) + 2gn_0(\mathbf{r}) - \mu}{k_B T}} \right) \quad (6.56)$$

So far, the model is similar to the one exposed in section 6.2.3. We define the thermal DeBroglie wavelength  $\lambda_T = \sqrt{\hbar^2/2\pi m k_B T}$  and:

$$g_{3/2}(x) = \sum_{n=1}^{\infty} \frac{x^n}{n^{3/2}} \quad (6.57)$$

In this model, the interactions between thermal atoms will be neglected due to the supposed low density of the thermal cloud, however their interactions with the condensate are kept. Then, eq.(6.55) remains the same. The main assumption is the existence of a quantitative equivalence between the chemical potential and the repulsive field in eq.(6.56). The peak density in eq.(6.48) is given by  $n_{\text{peak}} = \mu/g$ , corresponding to the minimum of the potential. The interactions of the atoms in the condensate is approximated by a homogeneous distribution, given by half of the peak density of the original distribution,  $n_{\text{uniform}} \approx n_{\text{peak}}/2 = \mu/2$ . The approximation is then,  $n_0(\mathbf{r}) \approx n_{\text{uniform}} = \mu/2$ . This approximation means that the thermal atoms interact independently from their position in the trap. The choice of  $n_{\text{uniform}} \approx n_{\text{peak}}/2$  is based on the mean value of the density of the condensate cloud based on:

$$\begin{aligned} n_{\text{uniform}} &= \langle n_0 \rangle = \int \psi^*(\mathbf{r}) n_0(\mathbf{r}) \psi(\mathbf{r}) \\ &= \int |\psi(\mathbf{r})|^4 d^3r. \end{aligned} \quad (6.58)$$

Applying eq.(6.48) to  $\psi(\mathbf{r})$  with an isotropic potential and a harmonic trapping potential, we have:

$$n_{\text{uniform}} = \frac{65\pi\sqrt{2}}{105(m\omega_{ho}^2)^{3/2}} \frac{\mu^{7/2}}{g^2}, \quad (6.59)$$

substituting eq.(6.50) in this expression gives us:

$$n_{\text{uniform}} = \frac{4}{7} \frac{\mu}{g} = 0.57 \frac{\mu}{g} \approx \frac{1}{2} \frac{\mu}{g}, \quad (6.60)$$

Therefore, the thermal atom density can be simplified as:

$$n_T(\mathbf{r}) = \frac{1}{\lambda_T^3} g_{3/2} \left( e^{-V(\mathbf{r})/k_B T} \right). \quad (6.61)$$

We integrate eq.(6.48) and eq.(6.61), using  $N = N_0 + N_T$ , resulting in an expression for the chemical potential:

$$\mu = \frac{3}{4\pi} \left[ \frac{Ng}{R^3} + \frac{2\pi}{5} m\omega_{ho}^2 R^2 - \frac{g(c_0 f(R/\sigma) + c_1)}{R^3} \left( \frac{k_B T}{\hbar\omega_{ho}} \right)^3 \right], \quad (6.62)$$

with

$$c_0 = \frac{4}{\sqrt{\pi}}, \quad c_1 = \zeta(3), \quad (6.63)$$

where  $\zeta(n)$  the Riemann zeta function,  $R$  is the limit of the Heaviside function of eq.(6.55) and  $\sigma = \sqrt{2k_B T/m\omega^2}$ . The expression eq.(6.62) contains the zero temperature term, the trapping energy term and the HF correction due to finite temperature. And finally the function  $f(R/\sigma)$ :

$$f(R/\sigma) = \left( \frac{R}{\sigma} \right) \sum_{n=1}^{\infty} \frac{e^{-n(\frac{R}{\sigma})^2}}{n^{5/2}} - \frac{\sqrt{\pi}}{2} \sum_{n=1}^{\infty} \frac{\text{erf} \left( n^{1/2} \frac{R}{\sigma} \right)}{n^3} \quad (6.64)$$

To determine  $R$ , we use the boundary condition:

$$n_0(R) = 0 \Rightarrow \mu - V(R) - 2gn_T(R) = 0, \quad (6.65)$$

leading to:

$$R^5 = \frac{15}{4\pi} \frac{g}{m\omega_{ho}^2} \left[ N - (c_0 f(R/\sigma) + c_1 + c_2 g(R/\sigma)) \left( \frac{k_B T}{\hbar\omega_{ho}} \right)^3 \right], \quad (6.66)$$

where  $c_2 = \frac{8}{3\sqrt{\pi}}$ . At  $T = 0$ , eq.(6.66) corresponds to eq.(6.51). We finally obtain [1] :

$$\frac{R^5}{N_0} \approx \frac{15}{4\pi} \frac{U_0}{m\omega_{ho}^2} \frac{1}{r} [1 - 0.83F(R/\sigma)(1 - r)], \quad (6.67)$$

where  $r = N_0/N$ . Where  $F(R/\sigma) = c_0f(R/\sigma) + c_1 + c_2g(R/\sigma)$  shown in Fig. 6.19, an approximated value of  $F(R/\sigma) \approx 0.55$  is taken from this curve using the fact that the ratio  $R/\sigma$ , which is the ratio between the radius of the condensate and the extension of the thermal cloud is in the range  $[0.8, 1.2]$  [1].

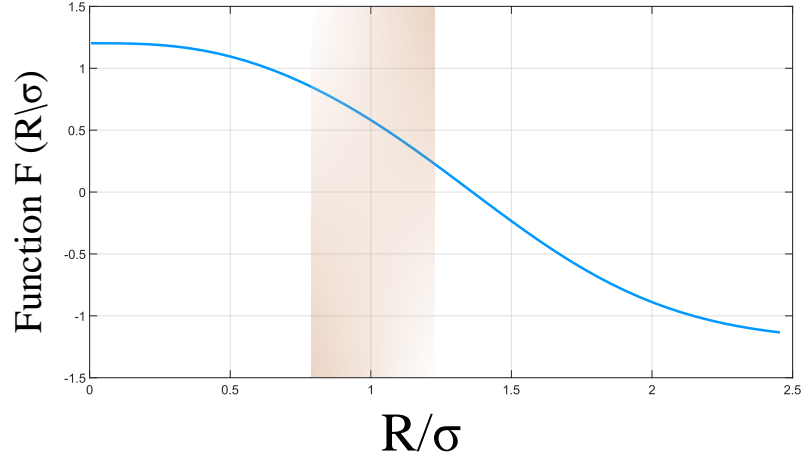


Figure 6.19: Function  $F(R/\sigma)$ . From [1]

In our case, we are interested in the value of  $R_z$ , therefore we use the eq.(6.52) into eq.(6.67) to obtain:

$$\frac{R_z^5}{N_0} \approx \frac{15}{4\pi} \frac{U_0}{m\omega_{ho}^2} \left( \frac{\omega_{ho}}{\omega_z} \right)^{5/2} \frac{1}{r} [1 - 0.83F(R_z/\sigma_z)(1 - r)]. \quad (6.68)$$

However, during the evaporation process that allows us to change the ratio  $N_0/N$ , we vary the trapping frequency  $\omega_{ho}$ , but the ratio  $\omega_{ho}/\omega_z$  is almost constant over the range that we use during the evaporation and can be averaged. Therefore the eq.(6.67) is plot in 3D (see Fig.6.20) to take in account the fact that  $\omega_{ho}$  changes.

#### 6.5.4 Comparaison of the 3 models

Here we present the different relations between the radius of the condensate and the condensate fraction in an anisotropic trap, using an ideal gas model eq.(6.52), a first

correction eq.(6.54) and an analytical HF model eq.(6.68). In our experiment we need to vary the trapping frequency to vary the temperature, therefore a 3D plot is necessary, and we compare these three methods in the following figure:

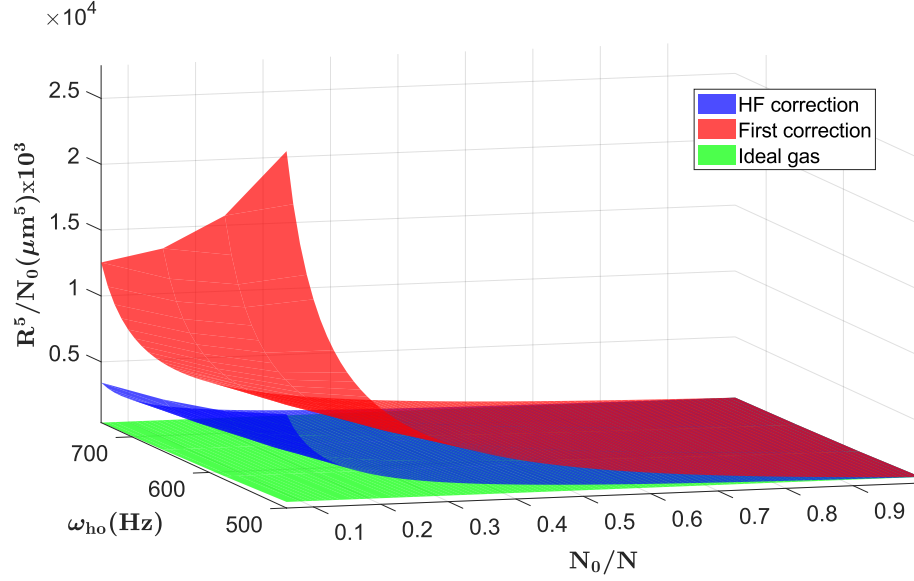


Figure 6.20: 3D plot of the three different model, the ideal gas model is simply a constant, the first correction gives larger radius of the condensate than the HF model when we approach the transition, i.e.  $N_0/N \rightarrow 0$ . For these plot we have chosen the scattering length  $a = 1600a_0$  and a ration  $\omega_z/\omega_r = 1/7$ .

## 6.6 Results

We use the results of the chemical potential from the HF model found in the previous section (see Fig. 6.16) in order to work out the radius of the condensate using eq.(6.46). The theoretical curve is obtained using eq.(6.68), however in our experiment in order to vary the condensate fraction  $N_0/N$ . Consequently, we need to vary the trapping frequencies, therefore the eq.(6.67) depends on two parameters, the condensate fraction  $N_0/N$  and the trapping frequency  $\omega_{ho}$ . The plot on Fig. 6.21 at  $1600a_0$  and  $3500a_0$  show a good agreement between the theoretical plot (the blue transparent curve) defined by eq.(6.67) and the experimental data (the cyan markers linked by the dark blue line). However at very high interaction  $4500a_0$  on Fig. 6.22 the model breaks down and does not correspond to the experimental data points.

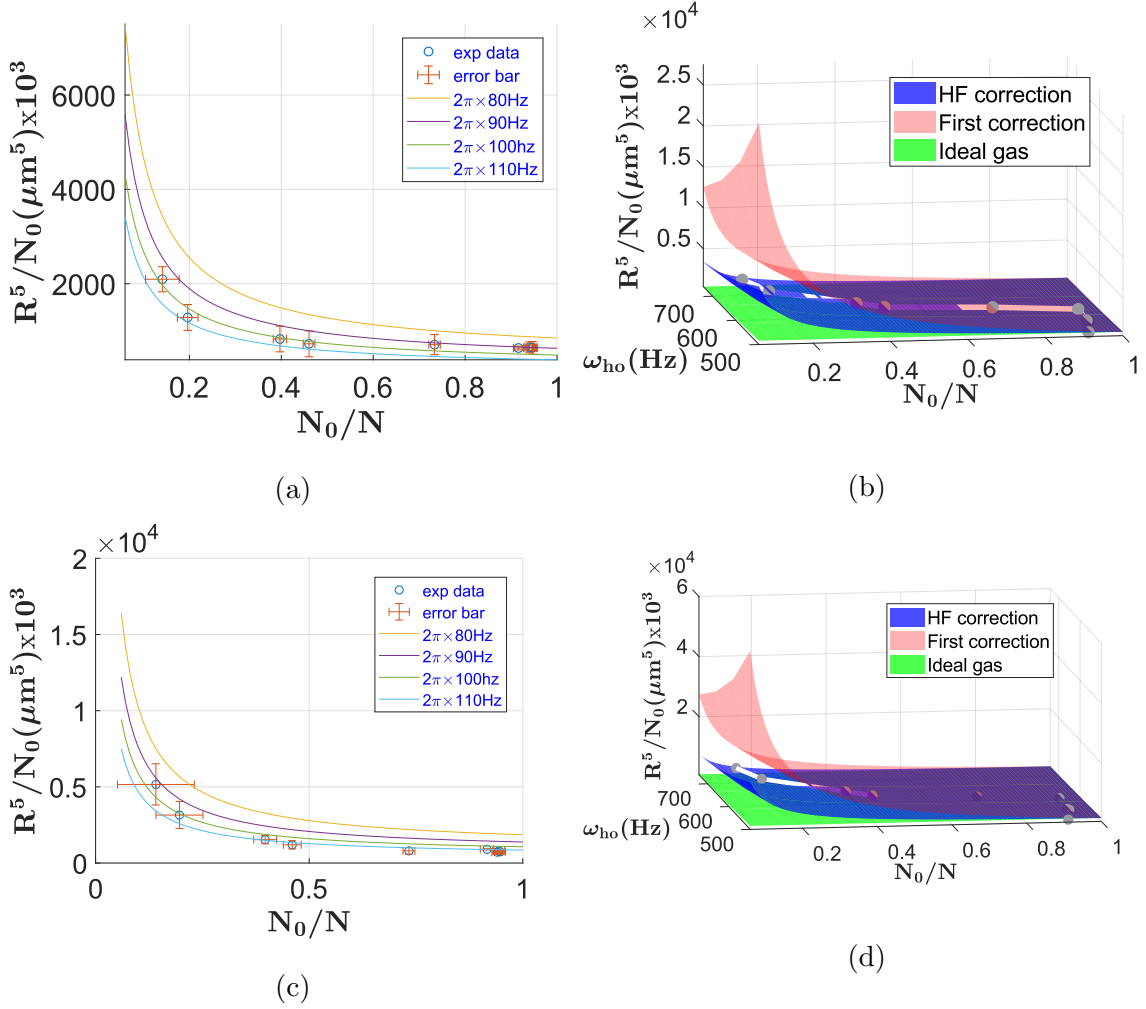


Figure 6.21: a) Radius measurement against condensate fraction with a scattering length  $a_s = 1600a_0$  using the HF model, the different lines represent different trapping frequencies. a) Radius measurement against condensate fraction with a scattering length  $a_s = 1600a_0$  in 3D using the three different models. a) Radius measurement against condensate fraction with a scattering length  $a_s = 3500a_0$  using the HF model, the different lines represent different trapping frequencies. a) Radius measurement against condensate fraction with a scattering length  $a_s = 3500a_0$  in 3D using the three different models.

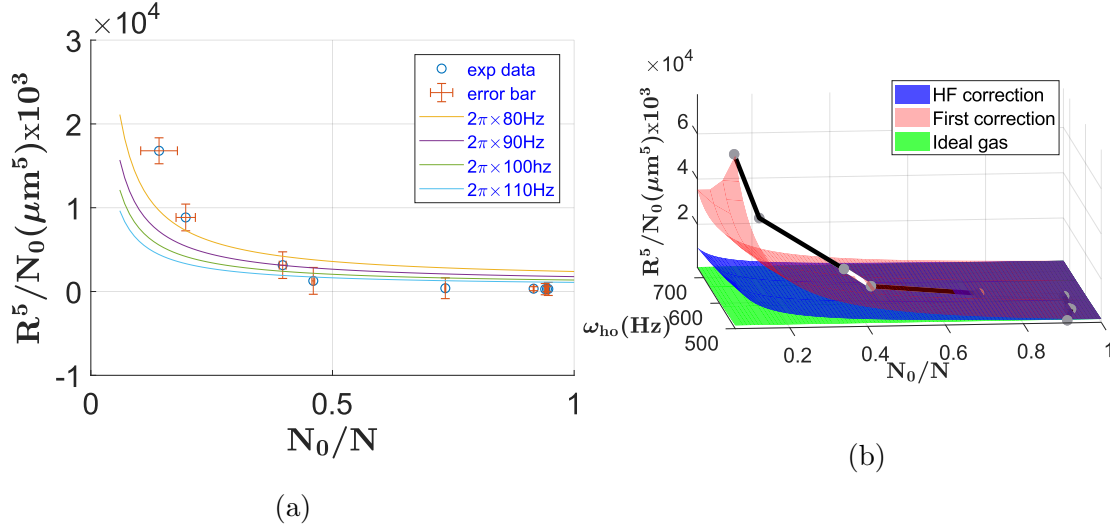


Figure 6.22: a) Radius measurement against condensate fraction with a scattering length  $a_s = 4500a_0$  using the HF model, the different lines represent different trapping frequencies. a) Radius measurement against condensate fraction with a scattering length  $a_s = 4500a_0$  in 3D using the three different models.

The good agreement between the radius of the condensate (strongly related to the chemical potential) with the theoretical 3D plots ( $1600a_0$  and  $3500a_0$ ) give us a supplementary argument in favour of the HF model and about the solidity of the analytical solution proposed in [1] even at higher interactions strength. These results also tend to confirm the coherence of the chemical potential behaviour found by the fitting program Fig. 6.16.

## 6.7 Prospects: Using an Energy conservation Method to Compare in-situ atom models

In this section, we develop a model to demonstrate with another method which models is the most accurate to describe the atomic cloud, using energy conservation arguments. The theoretical model has been elaborated with the help of N. Welch, and we describe an experimental application of that model. The previous section

explained how to find the temperature, chemical potential and condensate fraction by fitting an in-situ atomic distribution using three different models. We found that the three models give differing results, especially at high atomic interaction strengths when a cold dense cloud can be mistaken for a Bose-Einstein condensate.

In order to test the accuracy of the three-models, we first calculate the total energy predicted by fitting the in situ atomic density in the crossed beam dipole trap using the three different models to obtain three different total energy. Then, we want to let the atomic cloud expand in one beam dipole (see Fig. 6.23) measure again its energy by fitting a Boltzmann function, by knowing the temperature we calculate the energy  $E = k_B T$ . Finally, we compare the total energy predicted by the three models with the energy of the cloud in the one beam dipole trap in order to confirm that the HF model is the most suitable.

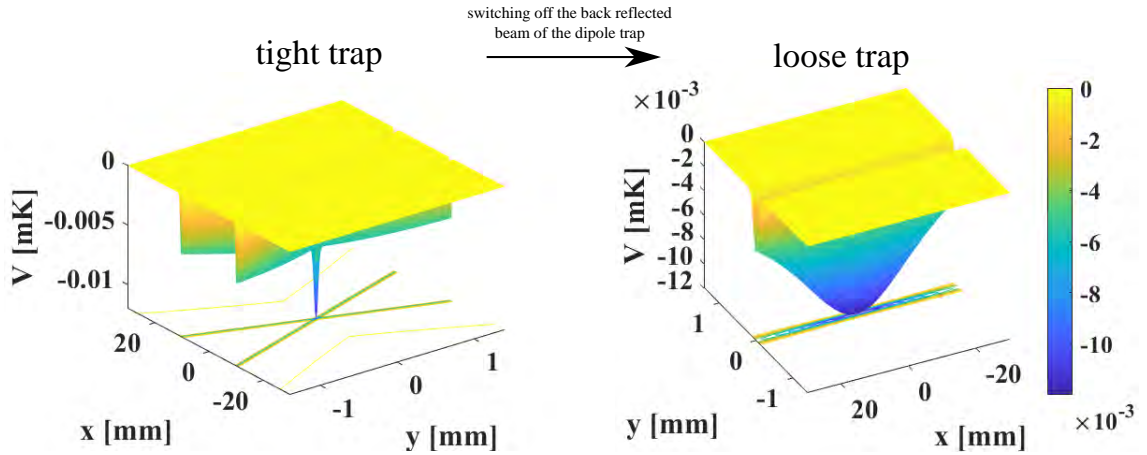


Figure 6.23: The atoms are transferred from a tight trap made of the two crossed beam, then we switch off one of the beam the create a shallower trap and let the atoms expand.

### 6.7.1 Total energy calculation

For the three-different models we need to calculate the total energy predicted from the fitted densities. Therefore, if we assume we have suitably close fits to the experimentally found in-situ thermal density  $n_{th}$  and condensate density  $n_c$ , then we



can calculate the atomic phase-space distribution according to each model and then calculate the total energy  $E_{tot}$ :

$$E_{tot} = E_k + E_{\text{int}} + E_{\text{trap,loose}}, \quad (6.69)$$

where  $E_k$  is the kinetic energy and  $E_{\text{int}}$  is the interaction energy, and  $E_{\text{trap,loose}}$  is trapping energy in the loose trap, given by:

$$E_{\text{trap,loose}}(z, r) = \frac{1}{2}\omega_{z,\text{loose}}^2 z^2 + \frac{1}{2}\omega_{r,\text{loose}}^2 r^2. \quad (6.70)$$

We calculate the energy distribution in phase-space of the atoms in the tight trap, using the spherical symmetry in k-space and cylindrical symmetry in real space:

$$\epsilon_1(k, r, z) = \frac{\hbar^2 k^2}{2m} + U_{\text{trap,tight}}(r, z) + U_{\text{int}}(r, z), \quad (6.71)$$

where the tight trapping potential corresponds to:

$$E_{\text{trap,tight}}(z, r) = \frac{1}{2}\omega_{z,\text{tight}}^2 z^2 + \frac{1}{2}\omega_{r,\text{tight}}^2 r^2. \quad (6.72)$$

Note that it is the third term,  $U_{\text{int}}$ , which differs between the different models. For the ideal-gas model it simply equal to zero. For the semi-ideal model it is equal to  $2gn_c(r, z)$  and for the Hartree-Fock model it is equal to  $2g(n_c(r, z) + n_{th}(r, z))$ . We can then find the energy by integrating the atomic distribution over the energy distribution of the new trapping potential, this is almost identical to eq.(6.71) except we now use the loose trapping potential:

$$\epsilon_2(k, r, z) = \frac{\hbar^2 k^2}{2m} + U_{\text{trap,loose}}(r, z) + U_{\text{int}}(r, z) \quad (6.73)$$

Therefore the energy of the thermal cloud is given by:

$$E_{\text{th}} = \int_0^{k_{\text{max}}} \int_0^{r_{\text{max}}} \int_0^{z_{\text{max}}} f(\epsilon_1) \epsilon_2 dv_{\text{ps}}, \quad (6.74)$$

where  $f(\epsilon)$  is the Bose-Einstein distribution:

$$f_\epsilon = \frac{1}{1 - e^{\frac{\epsilon - \mu}{k_B T}}}, \quad (6.75)$$

and the volume element in phase-space is given by:

$$dv_{\text{ps}} = \frac{1}{8\pi^3} 4\pi k^2 dk 2\pi r dr dz, \quad (6.76)$$

where we have not carried out any cancellation of the factors to explicitly show that each element  $(dkdx)^2$  has a volume of  $\frac{1}{(2\pi)^3}$  in phase space. We also show that in order to save computationally, we are using spherical symmetry in  $k$  and cylindrical symmetry in  $r$  and  $z$  as mentioned and also mirror symmetry in  $z$ . In addition this energy we will also need the trap and interaction energy of the condensate itself. We assume that we are in Thomas-Fermi approximation. The integral to find the energy of the condensate cloud is then given by:

$$E_c = \int_0^{r_{\text{max}}} \int_0^{z_{\text{max}}} n_c(r, z) \epsilon_3 dv, \quad (6.77)$$

where the energetic distribution is only spatial and given by:

$$\epsilon_3(r, z) = U_{\text{trap, loose}}(r, z) + U_{\text{int}}(r, z). \quad (6.78)$$

This time the interaction potential is the same for the ideal model but for the semi-ideal it is  $gn_c(r, z)$  and for the Hartree-Fock model it is equal to  $g(n_c(r, z) + 2n_{\text{th}}(r, z))$ . The spatial integration volume element is now given by:

$$dv = 2\pi r dr 2z dz. \quad (6.79)$$

### 6.7.2 Predictive capabilities

Using eq.(6.74) and eq.(6.77), we can then find the total energy  $E_{\text{tot}} = E_c + E_{\text{th}}$ . For the same atom cloud the three different models will produce three different values of  $E_{\text{tot}}$ . If we then assume that once the cloud has equilibrated entirely and the transfer was adiabatic in the loose trap, this energy will have been conserved. Additionally, if the cloud is suitably low density due to the low trapping frequencies, we should then be able to model the cloud as an ideal Maxwell-Boltzmann gas. Therefore, if the equilibration takes place entirely adiabatically, the three different total energies

can be translated to three different temperatures,  $T_{\text{loose}} = E_{\text{tot}}/(3k_B N)$ . By fitting the low density gas to a simple Gaussian distribution, we should quickly be able to find the actual new temperature and see which model is closest with its prediction.

### 6.7.3 Numerical integration

The integration maxima can be found by approximating the very end of the atomic distribution as a Maxwell-Boltzmann type curve and so using the limits of double bit-precision a maximum energy can be found:

$$E_{\text{max}} = 16k_B T \log(10) \quad (6.80)$$

From this we can find the approximate spatial and k-space limits:

$$r, z_{\text{max}} = \sqrt{2E_{\text{max}}/m}/\omega_{r,z}, \quad (6.81)$$

.

Note that this approximation is only used to aid in numerical stability. We can then carry out the integrations numerically using an equally spaced grid and improving the accuracy by using composite Newton-Cotes coefficients [97].

### 6.7.4 Experimental application

For this method to work as described in the introduction, the atomic cloud has to reach the ideal gas situation. Therefore, we have to let the cloud expand for a sufficient expansion time  $> 15\text{ms}$ , so that the effects of interaction have vanished. The idea is to transfer the atomic cloud from the dipole trap with two beams (tight trap) to a shallower dipole trap (loose trap) with one beam and let the atoms reach their classical behaviour, then perform a simple IG model fitting. To do so, a shutter is placed on the way back of the dipole trap beam Fig. 6.24. A picture is then taken after a sufficient time  $t \approx 20\text{ms}$ .

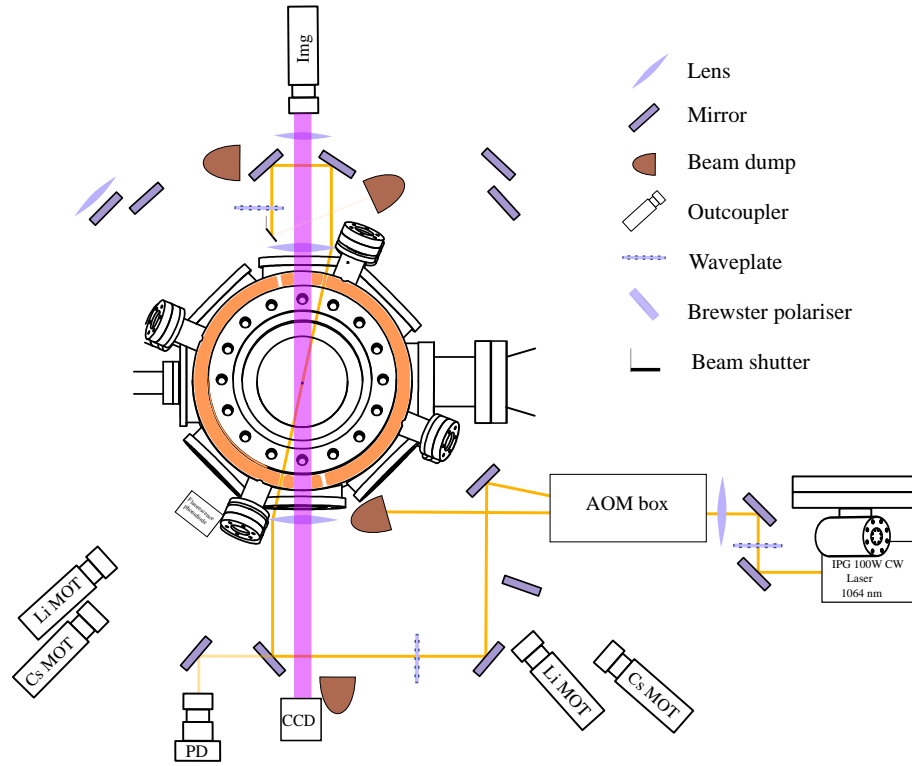


Figure 6.24: Top view of the main chamber. The yellow path represents the path of the optical dipole trap, a beam shutter is set in order to block the beam before it enters again in the main chamber.

An absorption imaging picture is taken in Fig. 6.25. So far the stability at this level of power did not let us image properly the cloud properly, too many atoms were lost during the transfer. Therefore, a next step will be to improve the stability and optimise the transfer between the tight trap and the loose trap.

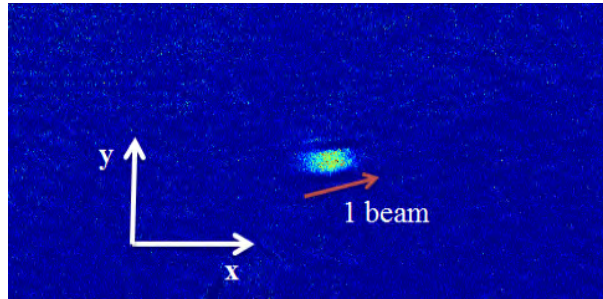


Figure 6.25: Absorption imaging picture of the atoms cloud transferred in the one beam dipole trap. The direction of the trap is rotated from the horizontal  $x$ -axis direction.

# Chapter 7

## Initial work: Double well with $^6\text{Li}$ molecules

### 7.1 Introduction

In this chapter we describe the state of the art and the implementation of a double well potential shaped dipole trap to reproduce a Josephson junction (JJ) [98] with cold atoms. Firstly, in order to observe the associated effects, such as Josephson AC/DC current [99], Josephson oscillations and self trapping [100–102]. Finally, a future step would be to use the second species  $^{133}\text{Cs}$  (see appendix G) as an impurity to realise the Dicke model [103]. Another experiment will be to perform large Josephson oscillations at the BEC-BCS crossover in order to observe solitons[102]. My contribution of this part was to design and set up the optics and electronics to create a double well shaped trapping potential.

### 7.2 A Josephson junction in the cold atoms paradigm

Cold atoms can be used for the simulation of condensed matter system. Here we describe the ultracold atoms equivalent of a JJ. First let's describe the original JJ [98] (see Fig. 7.1).

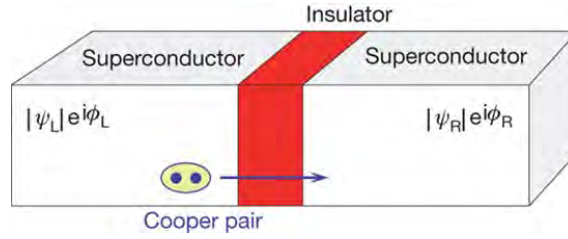


Figure 7.1: The classic JJ, consist of two superconductors separated by an insulator. From [19].

The left and right sides are described independently by two macroscopic wave functions with  $\psi_{L/R}$  the amplitude of probability and  $\phi_{L/R}$  the phase, and the relative phase  $\phi = \phi_L - \phi_R$ .

In a condensed matter system, two electrons at the Fermi sea surface in a superconductor pair up to create the so-called Cooper pair. In our cold atoms experiments, the cooper pairs are formed by attractively interacting lithium atoms, that exist in different states (BEC, BEC-BCS crossover, BCS) (see Fig. 1.2), note that a JJ has been realised and observed among those states [104]. The equivalent of the insulator is an optical barrier obtained by using a blue detuned light beam depicted in Fig. 7.2 (see section 4.3).

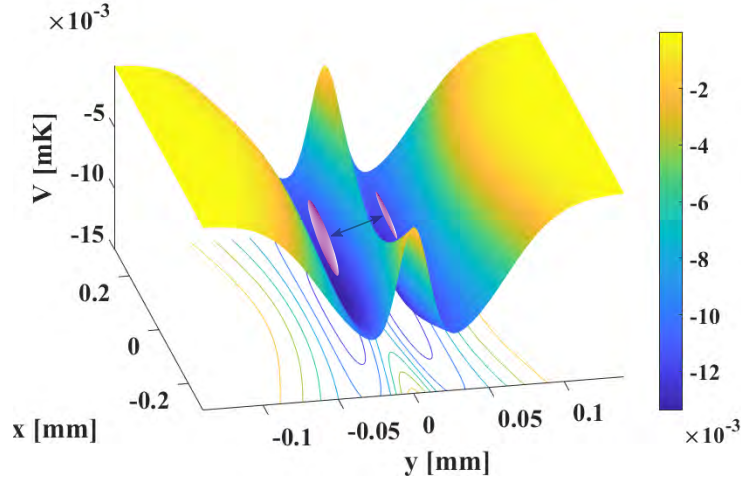


Figure 7.2: Double well trap created by the superposition of the optical dipole trap described in section 5.4.2 and a blue detuned beam, in this figure the power of the dipole trap beam is  $P_1 = 1W$  and the blue laser beam is  $P_2 = 100mW$ . The atoms are on both side of the barrier.

Once the atoms are condensed into a BEC, the optical barrier is ramped-up adiabatically, the position of the barrier allows us to adjust the population imbalance  $z$  between the two sides:

$$z = \frac{N_L - N_R}{N_L + N_R}. \quad (7.1)$$

The population imbalance can also be adjusted via a magnetic coil gradient to move the atoms Fig. 7.7 [105]. The conduction  $G$  can be adjusted by the proportion of thermal atoms in the BEC and the height of the optical barrier.



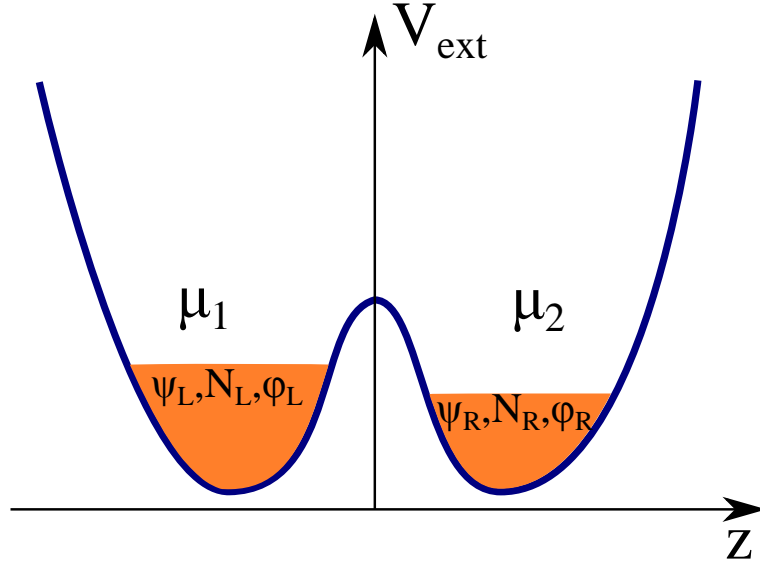


Figure 7.3: Schematic geometry of the double well with a split BEC. Where  $\mu_i$ ,  $N_i$  and  $\phi_i$  are respectively the chemical potential, atom number and phase. The value  $i$  defines the side in which the BEC is situated,  $R$  for right side and  $L$  for left side.

Different effects have been observed so far: **Plasma oscillations/Self-trapping.** In the case of the plasma oscillations, the difference between the population of the right side and left side of the double well must be under a certain critical value,  $z_C = 0.5$  for rubidium 87 atoms described in [100]. This leads to oscillations in  $z$  and  $\phi$ , corresponding to a harmonically oscillating pendulum. In the case of  $z > z_c$ , the on-site interaction energy becomes larger than the tunnelling energy [106]. The phase increases rapidly in time, and leads to a fast tunnelling current, the population imbalance stays around the initial value, and the phase grows monotonically, so called self-trapping. For a system described in Fig. 7.3, the Josephson's oscillations are mathematically defined by a couple dynamic equations for the variation of the phase and the population imbalance [99, 100]:

$$\dot{\phi} = \frac{\Delta\mu}{\hbar} - \omega_J \frac{z}{\sqrt{1-z^2}} \cos \phi, \quad (7.2)$$

and

$$\dot{z} = \omega_J \sqrt{1-z^2} \sin \phi - G\Delta\mu, \quad (7.3)$$

where  $G$  is the conductance,  $\omega_J$  the tunneling frequency, the chemical potential  $\mu = \mu_1 - \mu_2$ , and the phase  $\phi = \phi_L - \phi_R$ . The second term on the right side of eq.(7.3) is a damping term due to the finite temperature of the BEC. In Fig. 7.4, we show simulation from GPE's LAB [107], allowing to solve dynamical GPEs and observe oscillations in the low interaction case.

The **a.c Josephson effect** seems at first similar to the plasma oscillations, however the difference between the plasma oscillations and the a.c Josephson effect is that the amplitude of  $\phi$  is different. For the plasma oscillations it is limited to  $\pi < \phi < \pi$  and can be defined for small amplitude, therefore the variation of the population can be approximated in that case to  $\dot{z} \propto \phi$ . In the case of the a.c Josephson effect, a constant  $\Delta\mu$  is applied, and for  $G = 0$ , we can write  $\dot{z} = -\omega_J \sin(\frac{\Delta\mu}{\hbar}t)$ . In the a.c Josephson effect, the phase  $\phi$  always increases and reveals the sinusoidal nature of eq.(7.3).

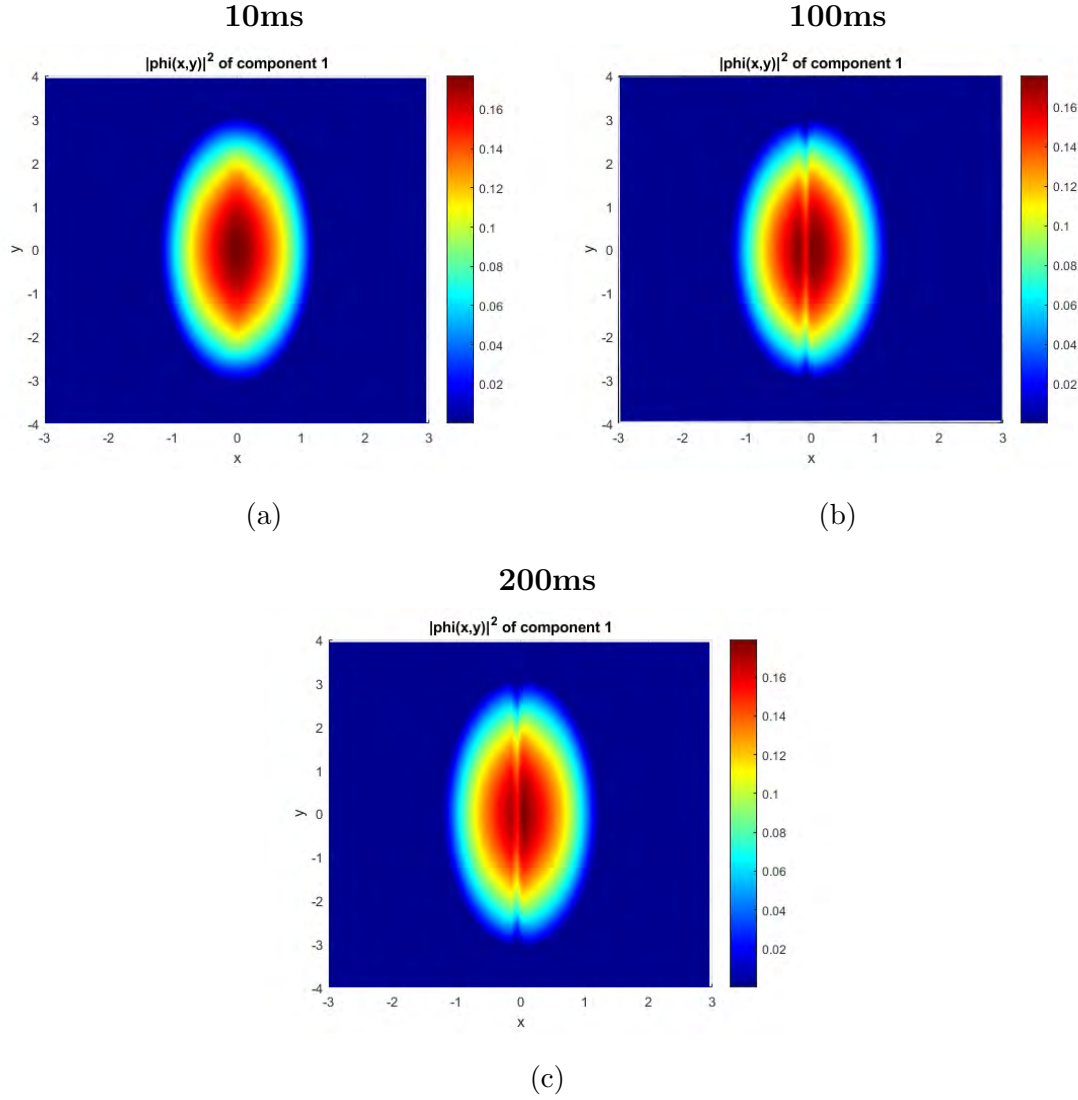


Figure 7.4: Simulation using GPElab [107]. Dynamical simulation of GPEs equations, using optical trapping frequencies  $\omega_r = 200\text{Hz}$  and  $\omega_z = 30\text{Hz}$ , and number of atoms  $N = 1000$ .

### 7.3 Experimental apparatus

In this section, we describe the experimental implementation of the double well. To do so, we have set a second laser beam (green beam on Fig. 7.5) blue detuned from the atomic transition. We choose a laser beam with a wavelength  $\lambda = 532\text{nm}$

(Dragon laser 1W, ref:532FN1W). This laser beam acts as a repulsive potential in the middle of the optical dipole trap, corresponding to the insulating barrier (see figure Fig. 7.2).

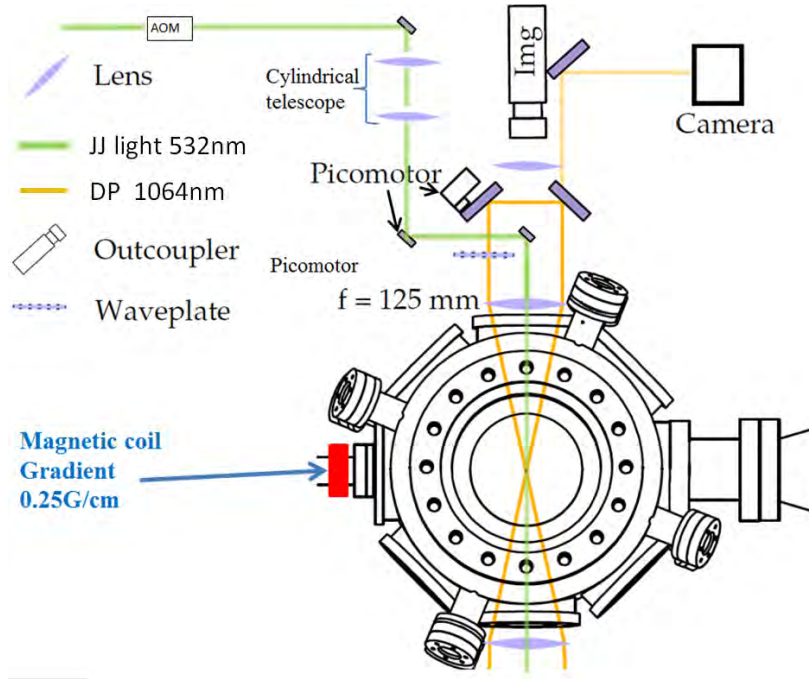


Figure 7.5: Figure of the experimental setup with the main chamber. The green line represent the repulsive barrier laser and the yellow line the harmonic dipole trap.

The blue detuned beam is initially an isotropic gaussian mode TEM00 with a diameter of 2mm and a wavelength of 532nm. The maximal laser output power is 1000 mW. An acousto-optical modulator allows fast switching off, and allows us to control the height of the repulsive barrier. In order to shape the beam to cut the optical dipole trap, we use a telescope of cylindrical lenses, to finally reach beam waist of  $2.3(1)\mu\text{m}$  at the position of the atoms (see Fig. 7.6). Also, a picomotor (see Fig. 7.5) is set to align the green beam in the centre of the trap, and create a population imbalance by creating an asymmetrical double well. The horizontal imaging light (see section 5.5) used for the  ${}^6\text{Li}_2$  also need to pass through the mirror after the picomotor, therefore we use a dichroic mirror (DMLP650) allowing the imaging light to pass and to reflect the green beam into the main chamber.

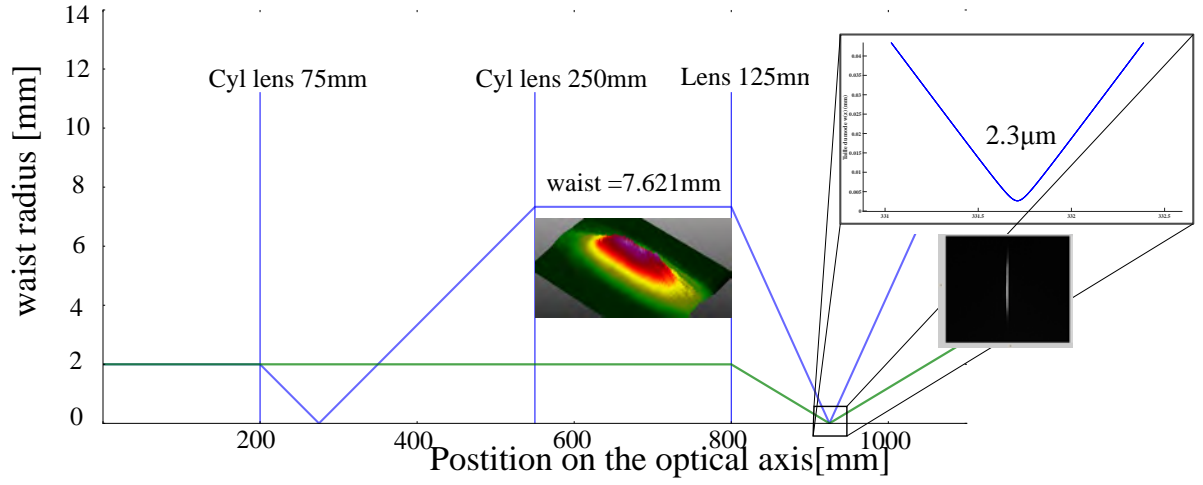


Figure 7.6: Evolution of the barrier laser vertical waist (blue line) and horizontal waist (green line) along the optical path shown in the previous figure.

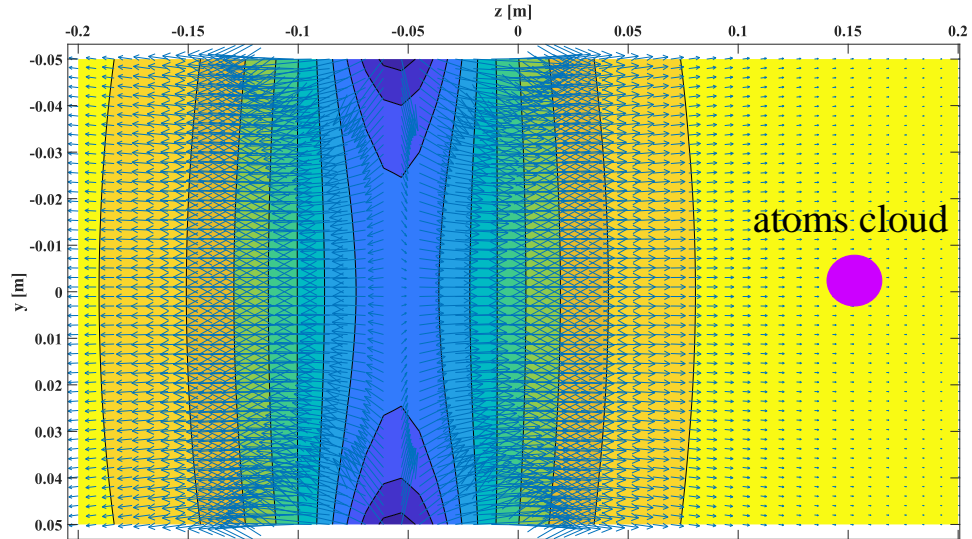


Figure 7.7: The last coil of the Zeeman slower (see section 5.2) is used in order to create a constant magnetic field on the atoms cloud in the double well.

## 7.4 Prospects

A first step in the future experiment will be to reproduce Josephson oscillations in the double well. Moreover, our experiment is designed to produce a second BEC of  $^{133}\text{Cs}$ , this second specie could be used as an impurity among the  $^6\text{Li}$  atoms to realise the Dicke model [103]. Another experiment will be perform large Josephson oscillations at the BEC-BCS crossover in order to observe the creation of solitons [102].

# Chapter 8

## Conclusions and outlook

The production of the molecular Bose-Einstein condensate is a challenging endeavour. The chapter 2 gives us the fundamental tools in order to understand the realisation of a mBEC. The chapter 3 gives us a detailed description of the important steps involved in the process, from the atomic beam production to the imaging of the atoms cloud. Every step is characterized in order to optimize the temperature and the density of the atoms all along the process. The full description of our future dual species oven is described in appendix G. Currently, a grey molasses [71] is being implemented, to do so a laser providing cooling and repumping light is under construction. This will allow us to reach lower temperature at the MOT stage. We have been able to load  $\approx 2 \cdot 10^6$  atoms in the optical dipole trap. The forced evaporation has also been enhanced by improving the AOM driver of the optical dipole trap, allowing us to reach lower temperatures. Additionally, a second photodiode has been added in the feedback loop of the PDI system to improve the stability of the optical dipole trap all along the evaporative process, and reach mBEC at very low temperatures. A better understanding of the Feshbach magnetic coils and the optical trapping potential has led to more accurate simulations to determine the trapping frequencies (see section 5.4.5) and obtain a better agreement with the measurements, where also new methods have been proposed. A method to determine the scattering length from the imaging laser frequency (see section 5.5.4)

have been tested, with a more accurate and faster reading of the scattering length value. For the first time in this experiment, an In-Situ imaging sequence has been implemented and used to perform measurements. The chapter 4 characterized the mBEC itself by fitting different models (Ideal gas, Semi-Ideal gas, Hartree Fock) to the one dimensional atomic density distribution measurements obtain by in-situ absorptions imaging. A program to analyse and average the atomic density profiles has been developed. Also, the fitting program initially proposed in [80] to fit the data to the different models has been improved and adapted to our experiment. This program takes the trapping frequencies of the trapping potential (longitudinal and radial), the scattering length  $a_s$  and the one-dimensional averaged density profiles, to give us the temperature, the chemical potential, and the condensate fraction of the mBEC. We test the three models using a statistical analysis method (see section 6.3). The stastitcal analysis of the results showed that the Hatree-Fock model is the most accurate to determine the thermodynamics properties of the mBEC when the temperature approaches  $T_c$  the critical temperature. The HF models takes in account the effects of the thermal cloud atoms interactions that depletes the condensate. Effects that are important due to the high interactions regime  $a_s > 1000a_0$ . Also, despite the relatively high interactions, the fits seem to hold and give sensitive results. The results are summed up in the article proposal appendix H. Moreover, the condensate radii has been calculated from the the chemical potential results, and fitted to an analytical formula giving a relation between the radius of the condensate and the consensate fraction[1]. The good agreement between the chemical potential (or condensate radius) gives us another indication of the consistency of the fitting program. The chapter 5 describes the implementation of a double well shaped optical trap, and proposes options to future experiments. On a different note, the productivity of the laboratory has been improved by the implementation of a second control system following the instructions in [65], allowing us to run both experiments ( $^6\text{Li}$ - $^{133}\text{Cs}$  mixture and Atom-Light integrated interface experiment[108]) present in the laboratory at the same time. The next step will be to perform the measurement



proposed in section 6.7, to confirm with an energy conservation based theory our results about the Hartree-Fock model. Additionally, the dual species oven described in appendix G is currently being implemented and tested. The second specie could be used to add impurities in the double well shaped optical trap implemented in the experiment (see section 7), in order to realise the Dicke model [103]. Another experiment will be to perform large Josephson oscillations at the BEC-BCS crossover in order to observe solitons[102].

# Bibliography

- [1] M. A. Caracanhas, J. Seman, E. Ramos, E. Henn, K. Magalhaes, K. Helmer-son, and V. S. Bagnato, “Finite temperature correction to the thomas–fermi approximation for a Bose–Einstein condensate: comparison between theory and experiment,” *Journal of Physics B: Atomic, Molecular and Optical Physics*, vol. 42, no. 14, p. 145304, 2009.
- [2] W. Pauli, “The connection between spin and statistics,” *Physical Review*, vol. 58, no. 8, p. 716, 1940.
- [3] M. H. Anderson, J. R. Ensher, M. R. Matthews, C. E. Wieman, and E. A. Cornell, “Observation of bose-einstein condensation in a dilute atomic vapor,” *science*, vol. 269, no. 5221, pp. 198–201, 1995.
- [4] C. C. Bradley, C. Sackett, J. Tollett, and R. G. Hulet, “Evidence of bose-einstein condensation in an atomic gas with attractive interactions,” *Physical review letters*, vol. 75, no. 9, p. 1687, 1995.
- [5] K. B. Davis, M.-O. Mewes, M. R. Andrews, N. J. van Druten, D. S. Durfee, D. Kurn, and W. Ketterle, “Bose-einstein condensation in a gas of sodium atoms,” *Physical review letters*, vol. 75, no. 22, p. 3969, 1995.
- [6] S. N. Bose, “Plancks Gesetz und Lichtquantenhypothese,” *Springer*, 1924.
- [7] M. Andrews, C. Townsend, H.-J. Miesner, D. Durfee, D. Kurn, and W. Ket-

- terle, “Observation of interference between two bose condensates,” *Science*, vol. 275, no. 5300, pp. 637–641, 1997.
- [8] M. Greiner, O. Mandel, T. Esslinger, T. W. Hänsch, and I. Bloch, “Quantum phase transition from a superfluid to a mott insulator in a gas of ultracold atoms,” *nature*, vol. 415, no. 6867, p. 39, 2002.
- [9] W. Ketterle, D. S. Durfee, and D. Stamper-Kurn, “Making, probing and understanding Bose-Einstein condensates,” *arXiv preprint cond-mat/9904034*, 1999.
- [10] B. DeMarco and D. S. Jin, “Onset of fermi degeneracy in a trapped atomic gas,” *science*, vol. 285, no. 5434, pp. 1703–1706, 1999.
- [11] G. Roati, F. Riboli, G. Modugno, and M. Inguscio, “Fermi-bose quantum degenerate k 40- r 87 b mixture with attractive interaction,” *Physical Review Letters*, vol. 89, no. 15, p. 150403, 2002.
- [12] Z. Hadzibabic, C. Stan, K. Dieckmann, S. Gupta, M. Zwierlein, A. Görlitz, and W. Ketterle, “Two-species mixture of quantum degenerate bose and fermi gases,” *Physical review letters*, vol. 88, no. 16, p. 160401, 2002.
- [13] A. G. Truscott, K. E. Strecker, W. I. McAlexander, G. B. Partridge, and R. G. Hulet, “Observation of fermi pressure in a gas of trapped atoms,” *Science*, vol. 291, no. 5513, pp. 2570–2572, 2001.
- [14] F. Schreck, L. Khaykovich, K. Corwin, G. Ferrari, T. Bourdel, J. Cubizolles, and C. Salomon, “Quasipure bose-einstein condensate immersed in a fermi sea,” *Physical Review Letters*, vol. 87, no. 8, p. 080403, 2001.
- [15] W. Ketterle and M. W. Zwierlein, “Making, probing and understanding ultra-cold fermi gases,” *arXiv preprint arXiv:0801.2500*, 2008.

- [16] M. W. Zwierlein, C. A. Stan, C. H. Schunck, S. M. Raupach, S. Gupta, Z. Hadzibabic, and W. Ketterle, “Observation of Bose-Einstein condensation of molecules,” *Physical review letters*, vol. 91, no. 25, p. 250401, 2003.
- [17] L. N. Cooper, “Bound electron pairs in a degenerate fermi gas,” *Physical Review*, vol. 104, no. 4, p. 1189, 1956.
- [18] T. Bourdel, L. Khaykovich, J. Cubizolles, J. Zhang, F. Chevy, M. Teichmann, L. Tarruell, S. Kokkelmans, and C. Salomon, “Experimental study of the beccs crossover region in lithium 6,” *Physical review letters*, vol. 93, p. 050401, 08 2004.
- [19] W. Ketterle and M. W. Zwierlein, “Making, probing and understanding ultra-cold Fermi gases,” pp. 20–30, Jan. 2008.
- [20] S. L. Cornish, N. R. Claussen, J. L. Roberts, E. A. Cornell, and C. E. Wieman, “Stable 85 rb Bose-Einstein condensates with widely tunable interactions,” *Physical Review Letters*, vol. 85, no. 9, p. 1795, 2000.
- [21] J. Dalibard, “Notes de cours: Atomes ultra-froids,” *ENS Ulm, Les gaz quantiques*, p. 108.
- [22] B. DeMarco, J. Bohn, J. Burke Jr, M. Holland, and D. S. Jin, “Measurement of p-wave threshold law using evaporatively cooled fermionic atoms,” *Physical review letters*, vol. 82, no. 21, p. 4208, 1999.
- [23] J. J. Sakurai and E. D. Commins, “Modern quantum mechanics, revised edition,” 1995.
- [24] F. Dalfovo, S. Giorgini, L. P. Pitaevskii, and S. Stringari, “Theory of Bose-Einstein condensation in trapped gases,” *Reviews of Modern Physics*, vol. 71, no. 3, p. 463, 1999.

- [25] M. Greiner, C. A. Regal, and D. S. Jin, “Emergence of a molecular Bose-Einstein condensate from a fermi gas,” *Nature*, vol. 426, no. 6966, pp. 537–540, 2003.
- [26] S. Inouye, M. Andrews, J. Stenger, H.-J. Miesner, D. Stamper-Kurn, and W. Ketterle, “Observation of feshbach resonances in a Bose-Einstein condensate,” *Nature*, vol. 392, no. 6672, p. 151, 1998.
- [27] C. Cohen-Tannoudji, B. Diu, and F. Laloë, “Mécanique quantique, tome 2, collection enseignement des sciences,” 1973.
- [28] C. Chin, R. Grimm, P. Julienne, and E. Tiesinga, “Feshbach resonances in ultracold gases,” *Reviews of Modern Physics*, vol. 82, pp. 1225–1286, Apr. 2010.
- [29] M. Bartenstein, A. Altmeyer, S. Riedl, R. Geursen, S. Jochim, C. Chin, J. H. Denschlag, R. Grimm, A. Simoni, E. Tiesinga, *et al.*, “Precise determination of li 6 cold collision parameters by radio-frequency spectroscopy on weakly bound molecules,” *Physical review letters*, vol. 94, no. 10, p. 103201, 2005.
- [30] K. Dieckmann, C. Stan, S. Gupta, Z. Hadzibabic, C. Schunck, and W. Ketterle, “Decay of an ultracold fermionic lithium gas near a feshbach resonance,” *Physical review letters*, vol. 89, no. 20, p. 203201, 2002.
- [31] K. OHara, S. Hemmer, S. Granade, M. Gehm, J. Thomas, V. Venturi, E. Tiesinga, and C. J. Williams, “Measurement of the zero crossing in a feshbach resonance of fermionic 6 li,” *Physical Review A*, vol. 66, no. 4, p. 041401, 2002.
- [32] G. Zürn, T. Lompe, A. N. Wenz, S. Jochim, P. Julienne, and J. Hutson, “Precise characterization of li 6 feshbach resonances using trap-sideband-resolved rf spectroscopy of weakly bound molecules,” *Physical review letters*, vol. 110, no. 13, p. 135301, 2013.

- [33] A. Einstein, “Preussische akademie der wissenschaften, phys-math,” *Klasse, Sitzungsberichte*, vol. 23, no. 3, 1925.
- [34] S. De Groot, G. Hooyman, and C. Ten Seldam, “On the Bose-Einstein condensation,” *Proc. R. Soc. Lond. A*, vol. 203, no. 1073, pp. 266–286, 1950.
- [35] W. Ketterle and N. Van Druten, “Bose-einstein condensation of a finite number of particles trapped in one or three dimensions,” *Physical Review A*, vol. 54, no. 1, p. 656, 1996.
- [36] G. Cook and R. Dickerson, “Understanding the chemical potential,” *American Journal of Physics*, vol. 63, no. 8, pp. 737–742, 1995.
- [37] J. Bardeen, L. N. Cooper, and J. R. Schrieffer, “Theory of superconductivity,” *Physical review*, vol. 108, no. 5, p. 1175, 1957.
- [38] V. L. Ginzburg, “High-temperature superconductivity (history and general review),” *Soviet Physics Uspekhi*, vol. 34, no. 4, p. 283, 1991.
- [39] J. G. Bednorz and K. A. Müller, “Possible high  $c$  superconductivity in the Ba-La-Cu-O system,” *Zeitschrift für Physik B Condensed Matter*, vol. 64, no. 2, pp. 189–193, 1986.
- [40] T.-L. Ho, “Universal thermodynamics of degenerate quantum gases in the unitarity limit,” *Physical review letters*, vol. 92, no. 9, p. 090402, 2004.
- [41] J. M. Hutson and P. Soldan, “Molecule formation in ultracold atomic gases,” *International Reviews in Physical Chemistry*, vol. 25, no. 4, pp. 497–526, 2006.
- [42] K. M. Jones, E. Tiesinga, P. D. Lett, and P. S. Julienne, “Ultracold photoassociation spectroscopy: Long-range molecules and atomic scattering,” *Reviews of Modern Physics*, vol. 78, no. 2, p. 483, 2006.

- [43] S. Jochim, M. Bartenstein, A. Altmeyer, G. Hendl, C. Chin, J. H. Denschlag, and R. Grimm, “Pure gas of optically trapped molecules created from fermionic atoms,” *Physical review letters*, vol. 91, no. 24, p. 240402, 2003.
- [44] J. Li, J. Liu, L. Luo, and B. Gao, “Three-body recombination near a narrow feshbach resonance in li 6,” *Physical Review Letters*, vol. 120, no. 19, p. 193402, 2018.
- [45] C. Chin and R. Grimm, “Thermal equilibrium and efficient evaporation of an ultracold atom-molecule mixture,” *Physical Review A*, vol. 69, no. 3, p. 033612, 2004.
- [46] W. Macke, “LD landau and EM lifshitz, quantum mechanics, non-relativistic theory. volume 3 of a course of theoretical physics,” *ZAMM-Journal of Applied Mathematics and Mechanics/Zeitschrift für Angewandte Mathematik und Mechanik*, vol. 39, no. 5-6, pp. 250–250, 1959.
- [47] Z.-C. Yan, J. F. Babb, A. Dalgarno, and G. Drake, “Variational calculations of dispersion coefficients for interactions among h, he, and li atoms,” *Physical Review A*, vol. 54, no. 4, p. 2824, 1996.
- [48] G. Gribakin and V. Flambaum, “Calculation of the scattering length in atomic collisions using the semiclassical approximation,” *Physical Review A*, vol. 48, no. 1, p. 546, 1993.
- [49] D. Petrov, “Three-body problem in fermi gases with short-range interparticle interaction,” *Physical Review A*, vol. 67, no. 1, p. 010703, 2003.
- [50] D. Petrov, C. Salomon, and G. V. Shlyapnikov, “Weakly bound dimers of fermionic atoms,” *Physical Review Letters*, vol. 93, no. 9, p. 090404, 2004.
- [51] H. J. Metcalf and P. Van der Straten, *Laser cooling and trapping*. Springer Science & Business Media, 2012.

- [52] K. Davis, “Bose-Einstein condensation in a gas of sodium atoms,” *Bulletin of the American Physical Society*, vol. 41, no. CONF-9605105-, 1996.
- [53] N. Newbury and C. E. Wieman, “Resource letter tna-1: Trapping of neutral atoms,” *American Journal of Physics*, vol. 64, no. 1, pp. 18–20, 1996.
- [54] Y. Castin, K. Berg-So, J. Dalibard, K. Mo, *et al.*, “Two-dimensional sisyphus cooling,” *Physical Review A*, vol. 50, no. 6, p. 5092, 1994.
- [55] W. Ketterle and N. Van Druten, “Evaporative cooling of trapped atoms,” in *Advances in atomic, molecular, and optical physics*, vol. 37, pp. 181–236, Elsevier, 1996.
- [56] C. Cohen-Tannoudji, F. Laloe, and B. Diu, *Mécanique quantique*, vol. 3. EDP Sciences, 2017.
- [57] C. J. Foot, *Atomic physics*, vol. 7. Oxford University Press, 2005.
- [58] P. S. Julienne, A. Smith, and K. Burnett, “Theory of collisions between laser cooled atoms,” in *Advances in atomic, molecular, and optical physics*, vol. 30, pp. 141–198, Elsevier, 1992.
- [59] M. E. Gehm, “Properties of 6Li.” <http://www.physics.ncsu.edu/jet/techdocs/pdf/PropertiesOfLi.pdf>.
- [60] D. A. Steck, “Cesium d line data.” <https://steck.us/alkalidata/cesiumnumbers.1.6.pdf>.
- [61] R. Grimm, M. Weidemüller, and Y. B. Ovchinnikov, “Optical dipole traps for neutral atoms,” in *Advances in atomic, molecular, and optical physics*, vol. 42, pp. 95–170, Elsevier, 2000.
- [62] C. Cohen-Tannoudji, J. Dupont-Roc, G. Grynberg, and P. Thickstun, *Atom-photon interactions: basic processes and applications*. Wiley Online Library, 1992.



- [63] A. Paris-Mandoki, *A single Apparatus for the Production of Ultracold Fermionic Lithium and Cold Bosonic Caesium*. PhD thesis, University of Nottingham, 2015.
- [64] S. Warriar, *Towards an Ultracold Bose-Fermi Mixture of Cesium and Lithium Atoms*. PhD thesis, University of Nottingham, 2014.
- [65] M. Jones, *Preparation of Cold Samples of Caesium-133 and Lithium-6 in a Single Apparatus for Bose-Fermi Mixture Experiments*. PhD thesis, University of Nottingham, 2014.
- [66] G. W. Thomson, “The Antoine equation for vapor-pressure data.,” *Chemical reviews*, vol. 38, no. 1, pp. 1–39, 1946.
- [67] R. C. Weast, “Handbook of chemistry and physics: a ready-reference book of chemical and physical data,” 1969.
- [68] W. D. Phillips and H. Metcalf, “Laser deceleration of an atomic beam,” *Physical Review Letters*, vol. 48, no. 9, p. 596, 1982.
- [69] E. Raab, M. Prentiss, A. Cable, S. Chu, and D. E. Pritchard, “Trapping of neutral sodium atoms with radiation pressure,” *Physical Review Letters*, vol. 59, no. 23, p. 2631, 1987.
- [70] F. Fatemi, M. Bashkansky, and Z. Dutton, “Dynamic high-speed spatial manipulation of cold atoms using acousto-optic and spatial light modulation,” *Optics express*, vol. 15, no. 6, pp. 3589–3596, 2007.
- [71] S. Rosi, A. Burchianti, S. Conclave, D. S. Naik, G. Roati, C. Fort, and F. Minardi, “ $\lambda$ -enhanced grey molasses on the D2 transition of rubidium-87 atoms,” *Scientific reports*, vol. 8, no. 1, p. 1301, 2018.
- [72] O. Luiten, M. Reynolds, and J. Walraven, “Kinetic theory of the evaporative cooling of a trapped gas,” *Physical Review A*, vol. 53, no. 1, p. 381, 1996.

- [73] S. Chaudhuri, S. Roy, and C. Unnikrishnan, “Evaporative cooling of atoms to quantum degeneracy in an optical dipole trap,” in *Journal of Physics: Conference Series*, vol. 80, p. 012036, IOP Publishing, 2007.
- [74] B. Yuen, “*Production and Oscillations of a Bose Einstein Condensate on an Atom Chip*”. PhD thesis, 2013.
- [75] D. Snoke and J. Wolfe, “Population dynamics of a Bose gas near saturation,” *Physical Review B*, vol. 39, no. 7, p. 4030, 1989.
- [76] R. Meppelink, R. Rozendaal, S. Koller, J. Vogels, and P. van der Straten, “Phase contrast imaging of Bose condensed clouds,” *arXiv preprint arXiv:0909.4429*, 2009.
- [77] M. Gajdacz, P. L. Pedersen, T. Mørch, A. J. Hilliard, J. Arlt, and J. F. Sherson, “Non-destructive faraday imaging of dynamically controlled ultracold atoms,” *Review of Scientific Instruments*, vol. 84, no. 8, p. 083105, 2013.
- [78] U. Schünemann, H. Engler, R. Grimm, M. Weidemüller, and M. Zielonkowski, “Simple scheme for tunable frequency offset locking of two lasers,” *Review of Scientific Instruments*, vol. 70, no. 1, pp. 242–243, 1999.
- [79] I. Hughes and T. Hase, *Measurements and their uncertainties: a practical guide to modern error analysis*. Oxford University Press, 2010.
- [80] N. Welch, *Non-equilibrium dynamics of Bose-Einstein condensates*. PhD thesis, University of Nottingham, 2015.
- [81] M. Naraschewski and D. M. Stamper-Kurn, “Analytical description of a trapped semi-ideal bose gas at finite temperature,” *Physical Review A*, vol. 58, no. 3, p. 2423, 1998.
- [82] A. Minguzzi, S. Conti, and M. Tosi, “The internal energy and condensate

- fraction of a trapped interacting bose gas,” *Journal of Physics: Condensed Matter*, vol. 9, no. 5, p. L33, 1997.
- [83] S. Giorgini, L. Pitaevskii, and S. Stringari, “Condensate fraction and critical temperature of a trapped interacting Bose gas,” *Physical Review A*, vol. 54, no. 6, p. R4633, 1996.
- [84] D. Hutchinson, E. Zaremba, and A. Griffin, “Finite temperature excitations of a trapped Bose gas,” *Physical review letters*, vol. 78, no. 10, p. 1842, 1997.
- [85] M. Holzmann, W. Krauth, and M. Naraschewski, “Precision monte carlo test of the hartree-fock approximation for a trapped Bose gas,” *Physical Review A*, vol. 59, no. 4, p. 2956, 1999.
- [86] L. Pitaevskii and S. Stringari, *Bose-Einstein condensation and superfluidity*, vol. 164. Oxford University Press, 2016.
- [87] W. Krauth, “Quantum monte carlo calculations for a large number of bosons in a harmonic trap,” *Physical review letters*, vol. 77, no. 18, p. 3695, 1996.
- [88] F. Gerbier, J. H. Thywissen, S. Richard, M. Hugbart, P. Bouyer, and A. Aspect, “Experimental study of the thermodynamics of an interacting trapped Bose-Einstein condensed gas,” *Physical Review A*, vol. 70, no. 1, p. 013607, 2004.
- [89] Y. Kagan, A. Muryshev, and G. Shlyapnikov, “Collapse and Bose-Einstein condensation in a trapped Bose gas with negative scattering length,” *Physical Review Letters*, vol. 81, no. 5, p. 933, 1998.
- [90] A. Gammal, L. Tomio, T. Frederico, *et al.*, “Dynamics of Bose-einstein condensation for negative scattering length,” in *Modern Challenges in Quantum Optics*, pp. 384–388, Springer, 2001.

- [91] S. Jochim, M. Bartenstein, A. Altmeyer, G. Hendl, S. Riedl, C. Chin, J. H. Denschlag, and R. Grimm, “Bose-einstein condensation of molecules,” *Science*, vol. 302, no. 5653, pp. 2101–2103, 2003.
- [92] R. P. Smith, R. L. Campbell, N. Tammuz, and Z. Hadzibabic, “Effects of interactions on the critical temperature of a trapped bose gas,” *Physical review letters*, vol. 106, no. 25, p. 250403, 2011.
- [93] Y. Inada, M. Horikoshi, S. Nakajima, M. Kuwata-Gonokami, M. Ueda, and T. Mukaiyama, “Critical temperature and condensate fraction of a fermion pair condensate,” *Physical review letters*, vol. 101, no. 18, p. 180406, 2008.
- [94] C. J. Pethick and H. Smith, *Bose-Einstein condensation in dilute gases*. Cambridge university press, 2002.
- [95] C. Gies, B. P. van Zyl, S. Morgan, and D. Hutchinson, “Finite-temperature theory of the trapped two-dimensional Bose gas,” *Physical Review A*, vol. 69, no. 2, p. 023616, 2004.
- [96] N. P. Proukakis and B. Jackson, “Finite-temperature models of Bose–Einstein condensation,” *Journal of Physics B: Atomic, Molecular and Optical Physics*, vol. 41, no. 20, p. 203002, 2008.
- [97] C. W. Ueberhuber, *Numerical computation 1: methods, software, and analysis*. Springer Science & Business Media, 2012.
- [98] B. Josephson, “Possible new effects in superconductive tunnelling,” *Physics Letters*, vol. 1, no. 7, 1995.
- [99] S. Levy, E. Lahoud, I. Shomroni, and J. Steinhauer, “The a.c. and d.c. Josephson effects in a Bose-Einstein condensate.,” *Nature*, vol. 449, pp. 579–83, Oct. 2007.

- [100] M. Albiez, R. Gati, J. Fölling, S. Hunsmann, M. Cristiani, and M. K. Oberthaler, “Direct Observation of Tunneling and Nonlinear Self-Trapping in a Single Bosonic Josephson Junction,” *Physical Review Letters*, vol. 95, p. 010402, June 2005.
- [101] S. K. Adhikari, H. Lu, and H. Pu, “Self-trapping of a fermi superfluid in a double-well potential in the Bose-Einstein-condensate–unitarity crossover,” *Physical Review A*, vol. 80, no. 6, p. 063607, 2009.
- [102] P. Zou and F. Dalfovo, “Josephson oscillations and self-trapping of superfluid fermions in a double-well potential,” *Journal of Low Temperature Physics*, vol. 177, no. 5-6, pp. 240–256, 2014.
- [103] J. Mumford, J. Larson, and D. O’Dell, “Impurity in a bosonic Josephson junction: Swallowtail loops, chaos, self-trapping, and dicke model,” *Physical Review A*, vol. 89, no. 2, p. 023620, 2014.
- [104] A. Spuntarelli, P. Pieri, and G. Strinati, “Josephson effect throughout the bcs-bec crossover,” *Physical review letters*, vol. 99, no. 4, p. 040401, 2007.
- [105] D. Stadler, S. Krinner, J. Meineke, J.-P. Brantut, and T. Esslinger, “Observing the drop of resistance in the flow of a superfluid fermi gas,” *Nature*, vol. 491, no. 7426, p. 736, 2012.
- [106] L. Salasnich, “L. salasnich, a. parola, and l. reatto, phys. rev. a 65, 043614 (2002).,” *Phys. Rev. A*, vol. 65, p. 043614, 2002.
- [107] X. Antoine and R. Duboscq, “GPElab, a matlab toolbox to solve gross–pitaevskii equations I: Computation of stationary solutions,” *Computer Physics Communications*, vol. 185, no. 11, pp. 2969–2991, 2014.
- [108] J. Nute, *A quantum integrated light and matter interface*. PhD thesis, PhD thesis, University of Nottingham, 2017.

- [109] N. Levinson, "On the uniqueness of the potential in a schrodinger equation for a given asymptotic phase," *Kgl. Danske Videnskab Selskab. Mat. Fys. Medd.*, vol. 25, 1949.